Synthesis and Characterization of Novel Transition Metal Chalcogenide Phases for Energy Storage, Energy Conversion and Optoelectronics

By

Erica Maxine Chen

A dissertation submitted in partial fulfillment
of the requirements for the degree of
Doctor of Philosophy
(Materials Science & Engineering)
at the University of Michigan
2017

Doctoral Committee:

Associate Professor Pierre Ferdinand Poudeu Poudeu, Chair
Professor Rachel S. Goldman
Associate Professor Pei-Cheng Ku
Professor Joanna M. Millunchick
Professor Jamie D. Phillips

ericamc@umich.edu
ORCID: 0000-0001-8998-8817

Dedication

My friends and family

Acknowledgements

Many people have given this work their support and contribution in some way: my friends, my family, my colleagues, committee members and collaborators. I'd like to take this opportunity to acknowledge everyone in guiding and supporting me through this long intellectual journey.

First and foremost, I'd like to thank my advisor, Professor Pierre Ferdinand Poudeu Poudeu. He welcomed me into his lab and has given me guidance and his patience, when I needed it most. I have utmost respect and eternal gratitude for this man. He gives tough love and doesn't mince his words. It doesn't matter if experiments were going well or not, he had a lot of feedback to give, which I have learned a lot from. When I was especially lost, his guidance gave me what I needed to move forward.

To my committee members Professors Joanna Millunchick, Rachel Goldman, Pei-Cheng Ku, Jamie Phillips and Bart Bartlett (former, from candidacy): thank you for serving on my doctoral committee. Your inputs into my projects have been enlightening and valuable. Thank you, Rachel, for sending out the admission letter January 2nd, 2011. I think I would have been working at a Californian steel processing company for not a whole lot and with potentially little career advancement.

My collaborators Prof. John Heron, Prof. Jay Guo, Prof. Citrad Uher, Prof. Emmanouil Kioupakis, Prof. Jennifer Aitken, Prof. Liang Qi, Mingfei Zhang, Logan Williams, Alex Page, Dr. Stanislav Stoyko and Dr. Cheng Zhang. I extend my deepest gratitude for working with me

on aspects of my projects which were not possible in my own lab. Prof. Heron offered his lab space and equipment for pulsed laser deposition and spent time with me to develop deposition parameters. Prof. Jay Guo and Cheng Zhang contributed their expertise and skill for ellipsometry data. Prof. Citrad Uher and Alex Page for contributing Hall measurement and simultaneous Seebeck and electrical resistivity measurements. Prof. Emmanouil Kioupkais and Logan Williams contributed advice and DFT calculations which had me focused on the Cu_4TiSe_4-related projects in the last couple of years. Prof. Liang Qi and Mingfei Zhang provided mechanical elastic constants and phonon dispersion for Cu_4TiSe_4. Prof. Aitken and Dr. Stoyko made an ultra-fast turnaround on two series of samples for UV-VIS-IR diffuse-reflectance spectroscopic data.

Special thanks to the Materials Science & Engineering department support staff: Debbie Johnson, Kevin Worth, Chris Cristian Shelley Fellers, Renee Hilgendorf, Tim Chambers, Justin Scanlon, Ying Qi, Keith McIntyre, Lisa Moran, Janet Riggs, Bonnie Viets and Georgia Knope. When I needed something ordered, when our fume hoods were down, training on the various Van Vlack Lab equipment, a poster printed, a hard drive salvaged, when the VVL equipment needed service – you were all there for me.

Thank you Prof. Bruce Dunn and Prof. Jenn-Ming Yang, they were my academic adviser and the former department chairs of the Materials Science & Engineering Department at UCLA respectively. Both of them encouraged me to pursue graduate studies and in particular Dr. Dunn encouraged me, “You would never be satisfied with just a B.S. Go to graduate school and get [a] Ph.D.” He was right and I am glad I followed his advice.

My colleagues, Alan Olvera, Juan Lopez, Brandon Buchanan and Ruming Lu have been supportive and a pleasure to work with. There are some great moments where bouncing ideas off

of you guys made a difference in the direction I took for my research. When something broke, we did our best to move things forward so that we could continue our research. I'd also like to acknowledge past members of our group: Dr. Nick Moroz, Dr. Yuanfeng Liu, Dr. Honore Djiuetedjeu, Dr. Pranati Sahoo, Dr. Nathan Takas, Dr. Julien Makongo, and Dr. Sanjaya Ranmohotti. Dr. Takas, Dr. Makongo and Dr. Ranmohotti were former postdocs who got me started and taught me basics of being in our lab and advice during the beginning of my study.

Scott Fenton, one of the CPHOM REU students that have come and gone through our lab, synthesized the $Cu_4TiSe_{4-x}S_x$ series and recorded all the powder X-ray diffraction patterns. I continued what he started by conducting additional characterization beyond powdered X-ray diffraction.

I give a shout out to my friends Mary Wise, Regina Garcia, Rosie Klauscher, Margaret Klauscher and Amy McKinley: Thank you for being there for me when big changes in my life uprooted me and forced me to consider how I want to restructure how I live and relate to others. I have become more grounded as a person through your friendship and through the things we did together which magnified and enriched my worldview. I am extremely grateful for the feedback Mr. Lukas Bell (Ford Motor Company) provided on my technical presentation for company interviews. In combination with the suggestions from my dissertation committee and my group members, I gave solid technical presentations. One of those interviews led to an offer at Lam Research, where I will begin the next step in my career.

Finally, I thank my parents and my brother Dr. Jeffrey Chen for their love, encouragement and support, not only in my PhD undertaking but also throughout my life. As my family, I couldn't ask for any better or any more. You are the best and I love you.

TABLE OF CONTENTS

List of Figures

List of Tables

List of Equations and Reactions

Abstract

Today's energy needs are primarily provided by fossil fuels, which are harvested from the earth. Consuming fossil fuels to provide energy for civilization releases products into the atmosphere that contribute to climate change. Ongoing efforts to combat the existential crisis which climate change presents many of the emerging and commercialized technologies for solar, thermoelectric and battery applications involve transition metal chalcogenides. Some of the materials used for these applications are expensive and rare, such as gallium, vanadium and indium, or have no merits towards environmental stewardship, such as cadmium and lead. Thus, the purpose of this work is to further the ongoing effort to discover and develop new materials which are able to meet or exceed benchmarks for their application.

This work focuses on the development of various metal chalcogenide material systems featuring d-block transition metals selected for their contribution to alter structure and properties. Various thermal, electronic and optical properties can be changed through substitution or doping with additional elements to affect to the base composition or as part of a gradient composition series. After an extensive description of experimental methods which describe the associated materials synthesis, processing and characterization techniques in chapter 2, chapter 3 explores the $Cu_{4-x}Li_xS_2$ phases for their contribution as further evidence in the formation of lithiated copper sulfide phases as part of the intercalation reaction before being converted to the binaries copper and lithium sulfide. Chapter 4 documents the development of Cu_4TiSe_4, a novel material with potential for thin-film photovoltaic technologies with its band gap in the range where the

solar spectrum is the most bountiful ($E_{g,indirect}$ = 1.16 eV, $E_{g,direct}$ = 1.34 eV), an outstanding optical absorbance (> 10^{-4} cm^{-1}) outperforming commercially successful materials in the solar spectrum, and suitable for thin-film fabrication. Chapter 5 describes a brief study in utilizing elemental substitution in Cu_4TiSe_4 to alter the band gap by replacing sulfur into the selenium site. In this study, the amount of selenium which may be substituted without deviating from the parent Cu_4TiSe_4 structure is 16 % at and the direct band gap is alterable from 1.34 eV to 1.64 eV as determined from conducting tauc analysis on the diffuse reflectance spectra. The last experimental work in Chapter 6 covers the development of a chemical substitution series between the end compounds Cu_3NbS_4 and Cu_3NbSe_4. Through powdered x-ray diffraction of the series, it was found that for substituting less than 25% of the sulfur with selenium, the powdered patterns more closely resembled Cu_3NbS_4 and with shift which may see further development and application in optoelectronic devices such as LEDs. Finally, Chapter 7 provides further guidance in the research which this thesis may serve as a springboard for the development of ultra-high efficiency, low-cost, environmentally friendly and thin photovoltaics as well as mention other characterization methods which are necessary to diagnose and elucidate complications.

Chapter 1 Introduction

1.1 Present State of Energy Sources for Energy Production

Currently, the world consumes energy at a rate which is not sustainable by consuming fossil fuels such as coal, oil and natural gas. In the United States alone, the energy consumption is approximately 97.65 quadrillion BTU (herein, quad or quads) and the energetic equivalent of 7.5 billion gallons of gasoline[1]. Various sources of energy are utilized to produce this amount, which total almost 111 quads. The United States exports about 13 quads. Of the remaining 98 quads in required source energy, more than 79 quads are sourced from the aforementioned fossil fuels which are domestically produced and imported from other countries. The remaining amount of energy is sourced through 8 quads of nuclear electric power and almost 10 quads of renewable energy. Notwithstanding the well-researched evidence contribution of burning fossil fuels to climate change[2,3] and lack of environmental stewardship, relying on burning fossil fuels to produce more than 80% of the United State's energy needs would eventually disadvantage the country in terms of national security and market stability. The inescapable fact about fossil fuels is in their inability to regenerate. Therefore, sourcing energy through renewable technologies and developing higher energy efficiency devices are significant avenues for reducing energy dependence on fossil fuels.

In terms of electricity, the United States consumed almost 39 quads of energy to produce 14 quads of electricity which are used in a variety of sectors.[4] About 61% of the energy used to

produce usable electricity is lost through conversion. Fossil fuels account for 24.99 quads or 64% of the total energy used to produce electricity while renewable technologies account for 5.34 quads or a little over 12%.[4] The 5.34 quads of renewable energy are sourced from wind, tidal power, geothermal, biomass and solar.[4] Of these renewable sources, solar has the greatest potential to meet large energy demands considering that land and ocean solar fluxes are on the order of 27,000 and 53,000 quads per year respectively.[5] Given the fact that the United States requires 14 quads per year, it is entirely possible to meet a large majority of the electricity need through collecting 50 quads (~0.14 quads per day) and supplementing with developing grid storage technologies such as flow batteries and sodium-ion batteries to meet electricity demand at night.

The cost of developing solar conversion to meet electrical demand currently costs $1.14 per Watt.[6] It is entirely possible that with economies of scale, this cost may fall below $1.00 per Watt, especially considering that countries such as Chile and Saudia Arabia are offering contracts to produce solar electricity at around $0.03 per Watt.[6] In the southwestern United States, GTM Research predicts that the cost of solar-generated electricity will drop as low as $0.75 cents per watt.[6,7] In contrast, coal costs $2.10 per watt for its construction cost[8] while natural gas-fired power plants are around $1.00 per watt[9]. Consequently, it is imperative to develop more advanced energy storage and conversion materials.

Several technologies have been developed to address energy storage and generating renewable energy. With respect to energy storage, there are a number of target areas established by size and environment. For example, grid energy storage requires larger scale energy density and safety. To that extent, there are redox flow batteries, PowerWall (Tesla) and Na-ion systems which can be utilized to address larger and more isolated needs. On a smaller scale for mobile

devices and high-powered electronics, there are Li-ion batteries which by far, have the largest gravimetric energy and power densities as compared to other the other technologies. With respect to Li-ion batteries, the capacity of cathodic materials have been severely outpaced by their anodic counterparts and present a large opportunity to further research and develop higher capacity cathode materials. This work explores the electrochemical performance of the known copper sulfide system with one significant difference in approach: create lithiated copper sulfide phases rather than the unlithiated phases.

For generating renewable energy, solar is of particularly great interest because of the large amount of solar energy that the earth receives and its importance in powering spacecraft. There are many emerging material systems that have been developed and are either flourishing as part of commercial offerings or are in the midst of commercial development such as CZTS[10,11], CdTe[12], CIGS[13,14], CIS[15], CGS[16], GaAs[17], Si[18] and many others[19,20]. However, they have detractors about them which limit their ability to go above and beyond, simply by their inherent material properties. For instance, Si has a lower absorption coefficient than all the other aforementioned solar cell materials, which is important for absorbing the photon energy for generating excitons.[21] Another material's shortfall is the cost of certain elements and/or their environmental hazard such as Cd in CdTe and indium in CIGS. Cu_4TISe_4 was discovered and developed in this work to especially overcome the limitations from a material's absorption coefficient and elemental abundance.

Another avenue to generate renewable energy is founded upon converting heat to electricity. This process is facilitated with thermoelectric devices. Further development of more efficient thermoelectric materials will allow greater utilization of waste heat conversion into electricity. The best materials for thermoeletrics are transition metal chalogenides which utilize the mass-

fluctuation provided in the elements and the chalcogens provide an electronic framework. In this work, $Cu_3NbS_{4-x}Se_x$ members were evaluated for their potential use in thermoelectric applications.

Lastly, the topic of band gap engineering has its application in energy-related problems, but it can also be applied to optoelectronics. In terms of band gap engineering for energy, the band gap is what allows the intake of photon energy of the band gap's energy to excite electrons from the valance band to the conduction band. Photon energy is across a spectrum, thus it is important to be able to adjust band gaps in material systems to harness larger fractions of the solar spectrum thereby increasing the amount of light energy converted into electricity. Another aspect of band gap engineering is to create green band-gap materials. Green band-gap materials are not that common and the one predominantly used in the market is gallium phosphide.

Thus, this work is segmented into different materials for Li-ion battery cathode materials, solar cell absorbers, thermoelectric and band gap tuning for optoelectronics.

1.2 Li-Ion Battery Cathode Materials

Lithium ion battery technology continues to be the primary method for energy storage for mobile transportation and is now making significant gains in the stationary energy storage market.[22] Still, improvements in positive electrode (cathode) materials are necessary for the production of rechargeable Li-ion batteries providing high energy, high power density and extended life cycle for mass vehicle electrification and to supplement the proliferation of solar technologies.[23] Another goal is to also make conversion of chemical energy into clean and sustainable electrical energy for mobile power. However, for large scale sustainable use of the Li-ion battery technology, one must develop positive electrode (cathode) materials sustainable

for the production of rechargeable Li-ion battery combining high energy, high power density and extended cycle life. The criterion for alternative positive electrode (cathode) material consists of (1) low chemical potential relative to lithium, (2) low molecular weight with high molar amount of Li participating in the intercalation, (3) high electronic and ionic conductivity and (4) structural stability for long cycle life. Cost, elemental availability and toxicity are other considerations when developing and testing new cathode materials. It is unlikely that there will be the best material, but only better materials with diversified merits.

The most commonly used cathode material is $LiCoO_2$, which was developed by John B. Goodenough in the 1980's.[24] While serving as the commercialized material for Li-ion battery, its shortfall is inherent in the compositions formulation using cobalt. Cobalt is an expensive heavy metal and areas that lack vigilance and/or compliance in proper disposal can lead to toxic waste accumulation in landfills. In addition to the environmental demerits, the capacity of $LiCoO_2$ is limited by its ability to intercalate only half of the stoichiometrically available lithium in order to maintain electrochemical reversibility. For practical and safety reasons, only half ($x = 0.5$) of the lithium in $LiCoO_2$ are removed and reinserted. Consequently, this limits the amount of useful energy that can be utilized.[25] While $LiCoO_2$ is able to satisfy most requirements, it certainly does not have a large amount of lithium participating in intercalation. Another limitation of $LiCoO_2$ is that the heavy metal cobalt where improper disposal risks environmental contamination. In this respect, $LiCoO_2$ is not sustainable for clean energy storage.

Several alternatives to $LiCoO_2$ have been developed and successfully commercialized, which alleviates concerns regarding environmental stewardship and fundamental limitations. An example material is $LiFePO_4$[26], which has the added bolster of additional capacity alongside its robustness in reversibility and not using cobalt as part of the formulation. Other materials have

been established through research such as lithium nickel cobalt aluminum oxide[27] and lithium nickel manganese cobalt oxide.[28-30]

1.2.1 Li-ion Battery Operation

Li-ion batteries for use in the storage of renewable energy from solar cells or thermoelectric devices secondary batteries, meaning they can be recharged through a reversible lithiation of the cathode and anode materials.

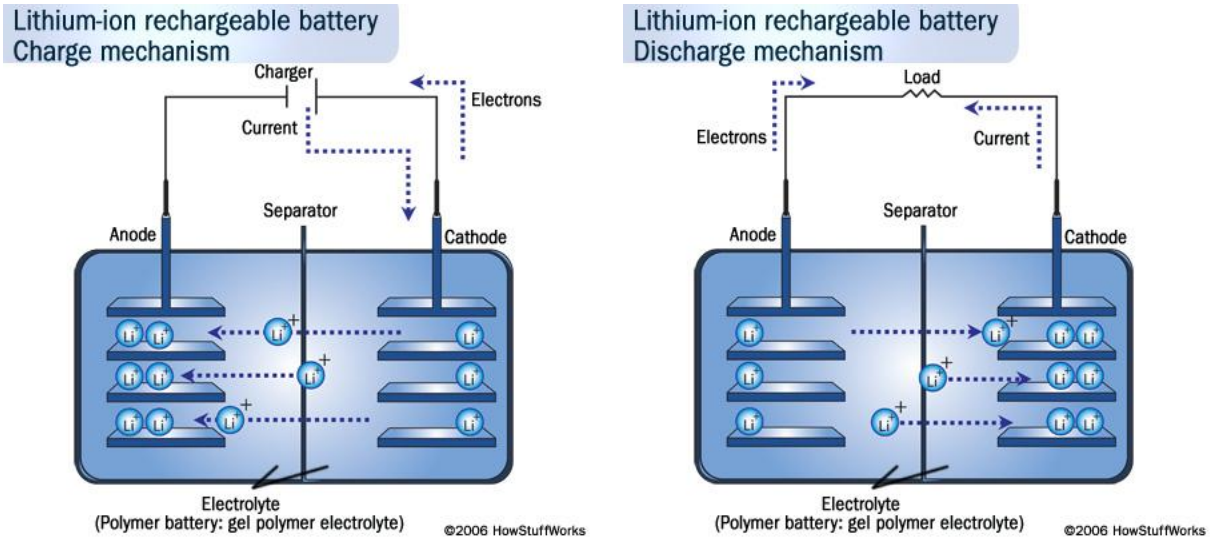

Figure 1-1: Lithium-ion battery a) charging mechanism and b) discharging mechanism.

The first part of this thesis examines lithium-ion cathodes, so the following illustration uses a $LiCoO_2$-Graphite material system as shown in Figure 1-1.[31] The $LiCoO_2$ is the positive electrode and the graphite is the negative electrode. There is a separator between the two electrodes which is electrically insulating but ionically conductive and an electrolyte (typically a lithium salt in a mixture of organic solvents) to facilitate ion transport. Lithium ions ideally flow in between the

two electrodes and electrons go through a charger or through an electrical load. The battery charges upon an application of a positive current and the following reaction occurs:

Equation 1-1 $$LiCoO_2 \rightarrow Li_{(1-x)}CoO_2 + xLi^+ + xe^-$$

The lithium migrates through the electrolyte and separator to be inserted into the anode. The cobalt changes oxidation state from 3^+ to 4^+ and releases the electron (oxidation) to maintain charge neutrality in the compound. The electron goes through the circuit to the other side. At the negative electrode, the following reduction reaction occurs:

Equation 1-2 $$xLi^+ + xe^- + 6C \rightarrow Li_xC_6$$

To discharge, the reactions are reversed. Oxidation occurs at the anode, releasing electrons into the circuit and lithium ions return to the cathode. The cathode material is reduced as it receives electron from the circuit. The process of lithium ions moving back and forth between the cathode and anode is called intercalation because lithium ions are inserted into the electrodes without modifying the material. As known from the second law of thermodynamics, a reversible process has a net entropy change of zero and discovery of material chemistries capable of demonstrating close to that ideal are important.

1.2.2 Lithiated Copper Sulfides

Copper (II) sulfide has good electronic conductivity 1 x 10^{-3} S/cm and its electrochemistry has been previously studied.[32-34] Recently, some lithiated versions of copper (I) sulfide with nominal composition "$Li_2Cu_4S_3$" have also been synthesized by organometallic cleaving and solid state.[35] Even though the compound synthesized by organometallic cleaving featured smaller particle sizes, the compound synthesized by the solid state route had better electrochemical

performance and stability. Unfortunately, this report also did not verify the amount of lithium content in their compounds. Therefore, it is possible that the ratio of lithium to copper can not only affect structure, but also the electrochemical performance. Chapter 3 discusses the synthesis of $Cu_{4-x}Li_xS_2$ phases and provides additional support that lithiated copper sulfide phases form with the addition of lithium and electrons during discharge.

1.3 Photovoltaics

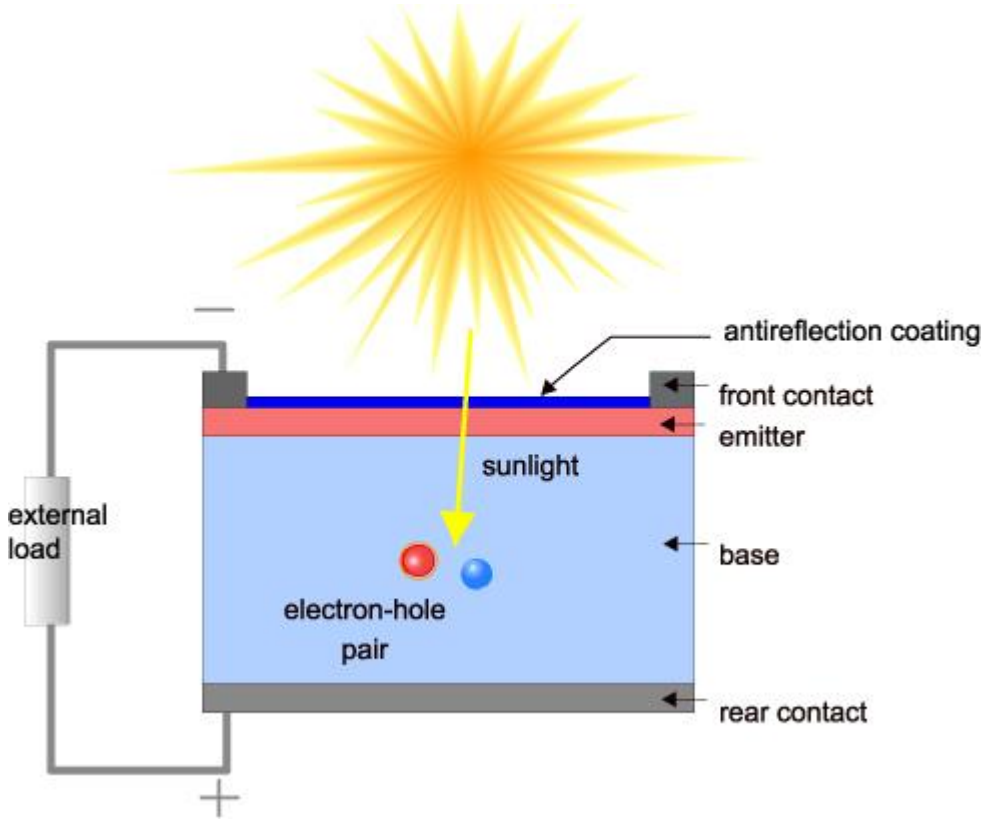

Figure 1-2: Illustration of a solar cell within a solar panel.[36]

Harnessing solar energy from the sun and converting it to useful electricity depends on a simple semiconductor device called a p-n junction. 27% of the global energy production is accounted for by various solar technologies and is predicted to become the largest source of

electricity by 2050.[6] 16% of the global electricity production is produced through just photovoltaic technologies.[6] There still remains a vast market potential which is currently taken up by fossil-based sources which can be slowly replaced through low-cost, non-toxic and higher efficiency materials.

1.3.1 p-n junction

Solar cells are built upon a fundamental structure (in terms of physical and electronic) of two types of semiconducting materials which are labeled according to the majority carrier species (either p for holes or n for electrons) called a p-n junction. Thin film solar cells consist of a thin p and a thin n layer, which are meant to convert specific wavelengths of light into electrical current. Consider a solar cell based on a single p-n junction as shown in Figure 1-2 with an electrode backing on the p-side and a transparent conducting oxide on the n layer, which are then connected to a circuit.[36] Incident photons excite the electrons in the n layer from the valance band to the conduction band and similarly excite holes in the p layer. The excited carriers migrate towards their respective electrode contacts, creating electrical current.

1.3.2 Transition Metal Chalcogenides in Photovoltaics

Presently, many of the thin film inorganic technologies involve transition metal chalcogenides: cadmium telluride (CdTe)[37-41], kesterite (CZTS)[42], copper indium gallium selenide (CIGS), copper indium selenide (CIS), and copper gallium selenide (CGS).[43-47]

CZTS[42] has made enormous gains in research cell efficiency since researchers began investigating, but CZTS has the longstanding problem that the zinc and iron can swap places, creating anti-site defects.[48-51] CdTe is commercially available and successful because cadmium is

an unwanted byproduct of zinc ore metal refinement, making it a cheap precursor material. However, cadmium is considered an environmental hazard which can make clean-up in the event of seismic catastrophe or end-of-life reprocessing a significant challenge and cost. Of the inorganic thin film technologies, CIGS has the largest cell efficiency to date at 20%.[46] As an added benefit, it does not pose anywhere near the environmental concerns that CdTe does, but indium is not considered an abundantly available element[52] which can make large scale deployment for large scale applications such as utility energy plants costly.

Chapter 4 discusses the development of Cu_4TiSe_4, which uses no toxic cadmium or expensive indium in its synthesis and has band gaps ideal for absorbing light in the 1.1-1.5 eV range, which represents the largest bulk of the wavelengths from the solar spectrum. Cu_4TiSe_4 also has an across-the-board enormous absorption coefficient that outperforms GaAs, CdTe, CIGS and CZTS. Both theoretical and experimental efforts have been undertaken to elucidate the extraordinary potential of Cu_4TiSe_4 as a p-type layer in thin film solar technology.

1.4 Band Gap Engineering

Band gap engineering serves as one of prime strategies for altering energy gaps for a variety of purposes: band alignment, photonic emission, and energy conversion. The tailored engineering of the band gap allows for device customization. The primary mode of band gap engineering in this work utilizes chemical substitution for the chalcogenide element for either a heavier or lighter one in the same period. In the case of chapter 5, the work therein describes the alteration of the parent material Cu_4TiSe_4 (from chapter 3) whereby equal amounts of selenium are replaced with equal amounts of sulfur. The purpose of the substitution is to increase the band gap of the parent material without significant altering its structure, so that it may remain

compatible with substrate materials. In chapter 6, another series between two end compounds is examined: Cu_3NbS_4 and Cu_3NbSe_4. Previous work utilizing density functional theory (DFT) has predicted the band gap for Cu_3NbS_4 to be 1.82 eV / 2.31 eV (indirect / direct) and 2.66 eV / 3.21 eV.[53,54] For Cu3NbSe4, its indirect and direct band gaps have been predicted to be respectively 1.45 eV and 1.95 eV .[53,54] Only Cu_3NbSe_4 has had its band gaps experimentally measured and they are reported as 2.14 eV and 2.45 eV respectively for indirect and direct.[55] The crystal structures of these two compounds are extremely similar to each other with similar lattice parameters. Thus, compositional tuning of a series between these end members have potential to be alternative green band gap materials. Another application of materials where the band gap is alterable through the composition is for tandem solar cells.

1.5 Thermoelectrics

Part of this work is also about the development of new and alternative materials for thermoelectric applications. Generating electricity from a heat source has been of keen interest for reclaiming energy from waste heat sources in industrial applications[56] and for radioisotope thermoelectric generators for space applications.[57] The Seebeck and Peltier Effects are what allow for solid-state conversion of heat into electricity and thermal management with applied electrical energy.[58]

1.5.1 Seebeck and Peltier Effect

There are two mechanisms which are exploited for thermoelectric technologies: The Seebeck Effect and the Peltier Effect. The former is the conversion of heat into electricity while the latter is heating or cooling at an electrified junction. The application of these effects in practice use a

large thermal gradient applied to the material to create charge migration in one direction. As the system reaches the steady-state condition, a voltage gradient arises as a consequence.

Mathematically, the Seebeck coefficient is the ratio of the voltage gradient with respect to the temperature gradient across the material as shown in the following equation as prescribed by Equation 1-3:

Equation 1-3

$$S = -\frac{\Delta V}{\Delta T}$$

Similarly, if there is a current I running from two materials with their respective Peltier coefficients, π_a and π_b,the Peltier heat generated at the junction per unit of time can be determined by the following relationship :

Equation 1-4

$$\dot{Q} = \left(\Pi_a - \Pi_b\right) I$$

Caution is advised considering that the Peltier effect does not also consider the effects of Joule heating and thermal gradient effects.

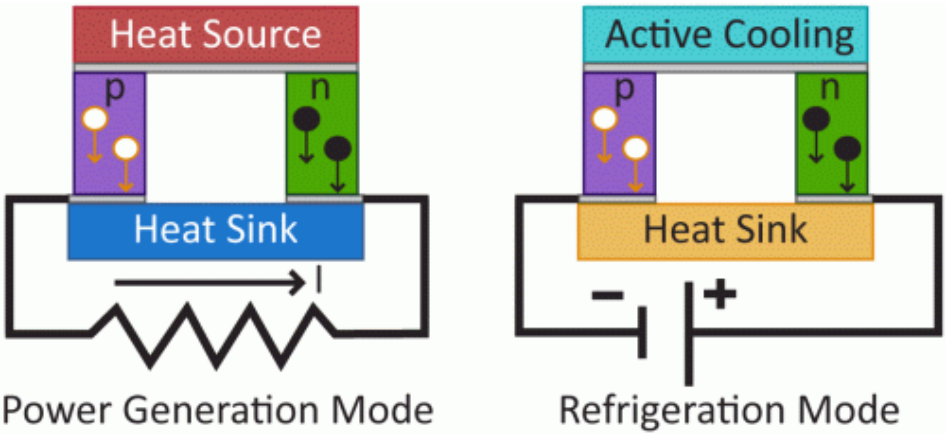

Figure 1-3: Schematic diagrams of thermoelectric modules in power generation mode and refrigeration mode.[59]

A thermoelectric device is built with a number of thermoelectric legs, although one pair of legs are shown in Figure 1-3 for each type of device. Each pair of legs consists of an n-type and p-type material wherein the type indicates the material's type of majority charge carriers. In the case of a thermoelectric device which coverts heat into electrical energy, carriers in both materials flow from the hot side (heat source) to the cold side (heat sink) which then drive a current form the legs with p-type material to the legs with n-type material. In the case of refrigeration mode (also known as thermoelectric cooling), a voltage is applied to the legs whereby the charge carriers then move towards the heat sink and the side opposite to where they move becomes cooler. This is due to the contributions of carriers to conduct phonons.

1.5.2 Thermoelectric Figure of Merit

Thermoelectric performance of a material with respect to temperature is defined using the following material properties: the Seebeck coefficient (S), the electrical conductivity (σ), and the total thermal conductivity (κ). They are related according to the equation (1-3)

Equation 1-5

$$ZT = \frac{S^2\sigma}{\kappa}$$

The material properties in the numerator of the relation, the quantity $S^2\sigma$, is also referred to as the power factor.

1.5.3 Development of Thermoelectric Materials

Ideally, the best materials for thermoelectric are those which facilitate the transport of electrons and inhibit the transport of phonons called electron-crystal-phonon-glass (ECPG). The "electron crystal" characteristic of ECPG materials is the concept that from the perspective of an

electron, the material is like a crystal which allows for the facile conduction of electrons. Contrary to the electron's free flow in the material, the "phonon glass" portion of ECPG describes the characteristic of amorphous materials which have low thermal conductivity because phonons, the vessel of 'heat', do not conduct well. However, materials with these features do not intrinsically exist and there are some fundamental limitations which require different mechanisms and strategies to achieve larger thermopower and ZT.

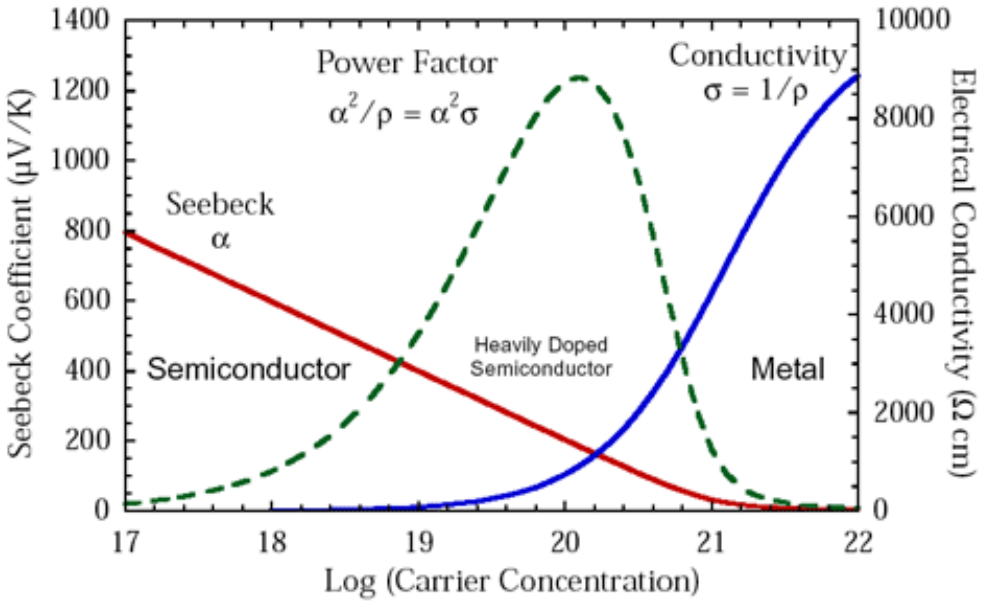

Figure 1-4: The relationship between Seebeck coefficient and conductivity's "inverse" dependence on carrier concentration highlighting a challenge in increasing thermopower.[60]

To understand this limitation, it is important consider the components of power factor. The two quantities are the electrical conductivity and the Seebeck coefficient. The electrical conductivity is related to the carrier concentration, n, and the carrier mobility, μ, as shown in Equation 1-6. The other part of the thermopower, the Seebeck coefficient, can also be defined with respect to k_B (the Boltzmann's constant), h (the Planck constant), m^* (the carrier's effective mass), and n (the carrier concentration) as shown in Equation 1-7.[61]

Equation 1-6

$$\sigma = \frac{1}{\rho} = ne\mu$$

Equation 1-7

$$S = \frac{8\pi^2 k_B^2}{3eh^2} m^* T \left(\frac{\pi}{3n}\right)^{2/3}$$

Through examination of these two equations (Equation 1-6 and Equation 1-7) and inserted into the equation for figure of merit (Equation 1-5), simply increasing the carrier concentration in the semiconductor will not suffice. Because the thermopower is inversely proportional to the carrier concentration, increasing the carrier concentration will eventually decrease the thermopower, as highlighted in Figure 1-4.[60] Thus, other methods for increasing thermopower have been developed such as through doping,[62-65] energy filtering,[60,66-70] electronic band structure engineering,[71-75] and/or increasing the effective mass of carriers.[71] To optimize ZT, the thermal conductivity must also be reduced or minimized. Strategies for reducing thermal conductivity comprise of intentional insertion of point defects,[76-78] nanostructuring,[60,66,79,80] and mesoscale features.[81,82]

Because the best thermoelectric materials have been metal chaclogenide binaries,[83-87] this work also explores the effect of chalcogen substitution in the $Cu_3NbS_{4-x}Se_x$ series to examine the effects of mass fluctuation on electrical transport.

Chapter 2 Experimental Techniques

In this chapter, synthesis and materials characterization techniques utilized in this work are described. The synthesis techniques used are solid-state, which produces bulk polycrystalline powder and pulsed laser deposition (PLD), which uses a bulk target to fabricate thin films. Single crystal growth is also required where there is not a suitable model structure in PDF4+ database or the inorganic crystal structure database (ICSD) to identify and elucidate crystal structure.

2.1 Synthesis

Two synthesis techniques, solid-state and pulsed laser deposition, were used to synthesize powders and films of the novel transition metal chalcogenide systems. Powders synthesized through the solid-state method are densified into targets to use for PLD.

2.1.1 Solid-State Synthesis

Solid state synthesis involves weighing, mixing and grinding stoichiometric amounts of high purity binaries and elements into a homogeneous mixture. The homogenenization achieved by grinding also serves to activate the surface to promote diffusion of the atomic elements.[88,89]

The mixture is then sealed in a quartz tube under ~10^{-3} Torr residual pressure and sheathed within mullite tubes with insulated ends. The mullite serves to protect the furnace from the sealed samples in case they rupture. The samples are left to anneal in the furnace programmed with a prescribed heating profile. After annealing, the evacuated tubes containing the products

are scoured and broken in a glovebox within an argon environment. Samples are reground into a fine powder and stored in the glovebox to prevent oxidation or reaction with moisture. Small amounts of sample are taken out of the box for measurement and processing. If necessary, according to resultant X-ray diffraction patterns and thermal signatures from DSC, the powders may be reground and resealed for further annealing.

For compositions containing alkali metals or other elements which have an affinity towards reacting with the quartz in a way that compromises its sealing integrity (and thus, compromising the desired composition to be synthesized), carbon-coating and/or the addition of aluminum oxide crucibles or carbon/graphite crucibles are employed as a safeguard measure.

2.1.2 Single Crystal Growth

Single crystals are grown through an extended temperature profile, partially determined from the thermal signature exhibited during the differential scanning calorimetry measurement. 100 mg – 250 mg of powdered sample are sealed in a 7 mm x 9 mm quartz tube or smaller and then left in the furnace to anneal with the extended temperature profile. After the samples are brought to room temperature, they are viewed under an optical microscope to verify the presence of single crystals on the tube walls and in the sample bulk. The selection of a specimen for single crystal X-ray diffraction is carried out qualitatively. The qualitative characteristics of single crystals will have a very shiny and faceted appearance. Each potential crystal was mounted on a thin glass fiber attached to a hollow aluminum pin after growth using either two-component epoxy resin and hardener or quick-drying glue.

2.1.3 Pulsed Laser Deposition of Thin Films

Pulsed laser deposition (PLD) is physical vapor deposition process technique where a high-power laser beam is focused upon a target of material. A plasma plume of vaporized material is created where the laser strikes and the ejected material deposits as a thin film on a substrate.

The process requires a vacuum chamber. As shown in Figure 2-1, the chamber contains a substrate stage, a target carousel, one more gate valves, laser window and a chamber access window[90]. A high energy laser, such as an KrF exciplex laser, is arranged some distance away, potentially with other lenses on an optics table, which are specially coated to reflect the laser's wavelength, and arranged in a way that guides the light towards the chamber. There is one last lens which concentrates the light produced by the laser, down to a small spot size, called a condenser lens. The spot is focused on a target of material.

For each laser pulse with sufficient energy density, a small amount of material gets ejected and creates a highly forward-directed plasma plume. This plume is 'aimed' (can be direct to the sample stage or offset, depending on the desired growth conditions) at the substrate and provides the material flux for growing a thin film. Because the contents of the plasma plume can have very high kinetic energy (hundreds of electron volts)[91], a mediating gas is used to slow the ions and/or particles down to prevent them from penetrating the substrate. An important enabling

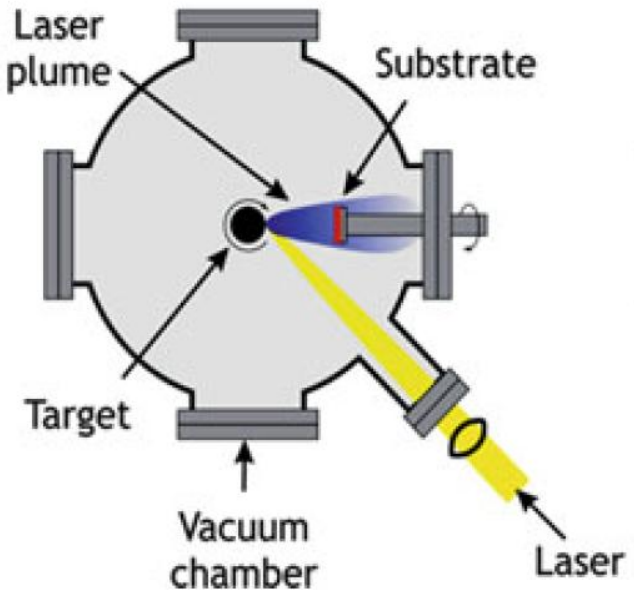

Figure 2-1: Schematic of a chamber for pulsed laser deposition.

characteristic of PLD is the stoichiometric transfer of ablated material onto the substrate.[91]

Typical deposition conditions in this work (Chapter 4) require a KrF laser (248 nm), base chamber pressure of 10^{-7} or 10^{-8} Torr, 10^{-2}-10^{-1} Torr of argon, rotation/raster of the target, elevated/ambient temperature of the substrate, laser energy between 40-350 mJ (depends on spot size to achieve desired fluence), pulse count 2000 – 96,000 and pulse frequency between 5-30 Hz. These conditions are modifiable depending on the desired film thickness and film morphology. For example, to produce a thicker film, the number of pulses can be increased. To produce a film with larger polycrystals, the substrate heater can remain on for a longer duration.

2.2 Densification and Post-Processing

Densification of as-synthesized powders is an important part of processing in order to assess bulk material properties such as the thermal conductivity, Seebeck coefficient and electrical conductivity. Post-processing involves grinding and polishing with SiC paper (400-600-800-1000-1200 grit) for measuring thermal conductivity using the laser flash method, which is described later in the chapter. If the measurement requires a prismatic bar (for example, simultaneous Seebeck and electrical conductivity measurement), post processing is grinding (400 and 600 grit), cutting with a silicon carbide slurry wire saw and final grinding (800-1000-1200 grits) and polishing to remove the graphite foil and ensure plane-parallel opposite surfaces. Acceptable bar dimensions are dependent on the capacity of the measurement system and consultation with measurement system operators or super users is highly recommended. For the ZEM-3, which is used in the simultaneous Seebeck and electrical conductivity measurement described later in the chapter, acceptable prismatic bars are at least 7.5 mm in length with at least

1.5 mm x 1.5 mm cross-section. The maximum length is 20 mm and the maximum recommended cross-section is 2.5 mm x 2.5 mm.

2.2.1 Uniaxial Hot Press

The uniaxial hot press combines temperature and pressure simultaneously to densify a given powdered material. A specific amount of material is weighed out according to calculation with respect to the density (either theoretically calculated or experimentally determined with a gas

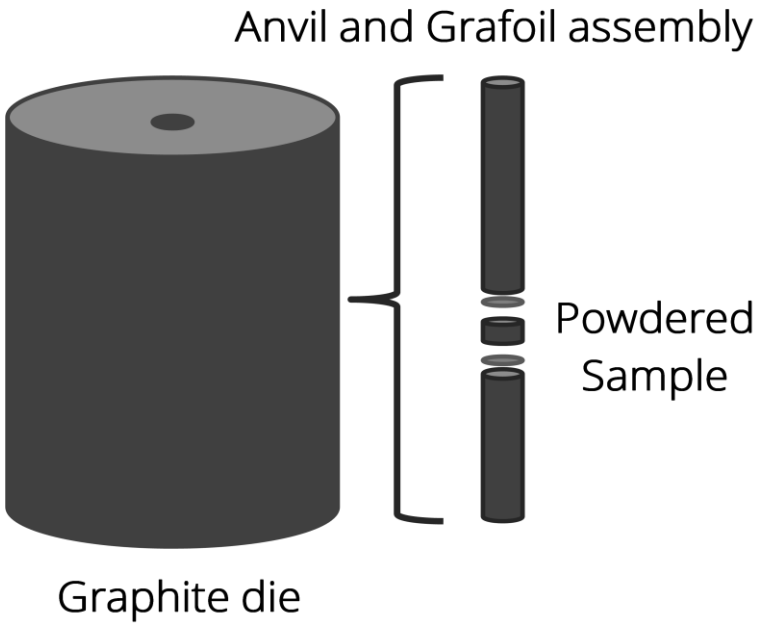

Figure 2-2: Uniaxial hot press assembly of die, anvil and Grafoil.

pycnometer), desired pellet thickness and die diameter. As shown in Figure 2-2, a graphite die is loaded with an anvil and a layer of Grafoil. Powder is inserted, pressed down, then another Grafoil cutout is placed on top and finally the plunger (a second anvil) is placed on top. This whole assembly is inserted into an integrated vertical graphite element vacuum furnace with hydraulically powered pressing graphite rams made by Astro Industries (HP4560-20). A pressure of up to 100 MPa is uniaxially applied to the die-anvil assembly and then evacuated to ~10^{-2} torr.

A steady flow of argon (20 ml/min) into the vacuum furnace prevents oxidation of the graphite components and provides an inert atmosphere for the densification process. A temperature profile is programmed into the controls. Once complete, the die is cooled to room temperature and the pellet is extracted with a bench top manual press.

2.2.2 Spark Plasma Sintering

Similar to the uniaxial hot press, spark plasma sintering (SPS) is another technique used to densify powder materials into pellets or bars using simultaneous application of elevated temperature and pressure. Uniaxial hot pressing requires significantly more than SPS. A typical uniaxial hot press duration is 4-8 hours but can be longer depending on the temperature profile. In contrast, SPS can complete a press cycle within a few minutes to forty-five minutes and also depends on the prescribed temperature profile. The difference between the two is that instead of a graphite heating element (or any other heating element such as molybdenum disilicide) surrounding the graphite die, high current is passed through the anvil and plunger, which heats up the sample very quickly. Die loadings were in between the platens of a FCT Systeme GmbH H-HP D 25-FL. 55 MPa of pressure was applied and the chamber was pumped down to ~10^{-3} torr.

2.2.3 Method for Verification of Pellet Density

The geometric density of the pellet is determined by measuring (with digital calipers) the thickness of the pellet, calculating its volume and then dividing its mass by the volume. Another method for determining density is through a gas pycnometer (Quantachrome Micro Ultrapyc

1200e). These values are compared to the theoretical density of the material to quickly assess phase integrity through the densification process and densification quality.

2.3 Characterization Techniques

A variety of characterization techniques were utilized to determine the structure and various properties of interest in the as-synthesized materials including copper lithium sulfide phases (Chapter 3) and Cu_4TiSe_4 (Chapter 4). Typical characterization techniques consist of powder X-ray diffraction, differential scanning calorimetry, and wavelength dispersive X-ray fluorescence.

2.3.1 Powder X-Ray Diffraction

The collection of powder X-ray diffraction (PXRD) patterns are used for phase identification, determination of impurity phases, atomic distribution and other information about the crystal structure. For powdered samples, specimens for PXRD are spread and filled uniformly into a rough indented area of a zero-background slide (special sample holder consisting of an off-axis cut single crystal). If the sample is monolithic or solid, the sample is mounted using an aluminum holder, clay and glass slides. The surface of the sample is made flush with the aluminum holder by pressing gently onto a hard and flat surface. This is done to meet the experimental requirements of the Bragg-Brentano geometry.[92] Specimens are loaded into a Rigaku Miniflex 600 operating at 40 kV and 15 mA with graphite monocrhomated Cu-Kα (λ = 1.54056 Å). If the samples were thin films on substrates, the diffraction patterns were taken on a rotating anode Rigaku Rotoflex operating at 40 kV and 100 mA. High temperature XRD powder patterns were collected under vacuum using a Rigaku Ultima IV X-Ray diffractometer.

2.3.2 Rietveld Refinement

Rietveld refinement is a technique which simulates a diffraction pattern based upon a model of the phase related to the experimentally taken diffraction pattern. It is an iterative process where a select number of different parameters which affect the simulated diffraction pattern, can be refined to match the experimental pattern through the least squares method. Rietveld refinement was predominantly used to determine lattice constants and atomic positions and occupation in the structure. For Rietveld refinement, the software package FULLPROF was utilized[93,94].

2.3.3 Single Crystal X-Ray Diffraction

Mounted single crystals are loaded into a STOE IPDS-2T diffractometer with a graphite monochromator using Mo Kα radiation (λ = 0.71073 Å) at 50 kV and 40 mA. The X-Area software package allows for initial indexing of the crystal based upon the recorded diffraction intensities. Further refinement was done using the SHELXTL package.[95,96]

2.3.4 Wavelength-Dispersive X-Ray Fluorescence

Wavelength-Dispersive X-Ray Fluorescence (WDXRF) is a fast, easy and non-destructive technique for determining the composition of a phase containing elements from fluorine to uranium. An X-ray source shines on the sample, and then the characteristic X-rays are "filtered" using specific crystals to diffract those characteristic X-rays and then collect the intensities on a detector. Specimens for WDXRF are prepared by loading samples (powdered or anything less than 1.5" in diameter) into Chemplex plastic cups lined with Prolene film.

2.3.5 Differential Scanning Calorimetry

Differential scanning calorimetry was used to record thermal signatures from the sample as compared to an empty crucible on a Netzsch DSC404 F1 Pegasus. Specimens for this measurement are prepared by loading approximately 30-50 mg of sample into a 2 mm x 3 mm quartz tube with a bulbed end. The small tube was sealed under residual pressure of 10^{-3} torr or lower. With both tubes loaded onto the sample carrier, 20 L /min of nitrogen was flowed through the chamber. The measurement recorded thermal signatures from room temperature all the way to 1273 K. Thermal signatures are analyzed for phase transitions, melting, and crystallization. If there were multiple or anomalous peaks for phase transitions, they were checked against phase diagrams in the ASM Phase Diagram Database in order to check for phase impurities which may be too small to diffract X-rays (cannot be 'seen' in PXRD).

2.3.6 X-Ray Photoelectron Spectroscopy

X-Ray photoelectron spectroscopy (XPS) was used to infer the oxidation states and bonding of atoms in the samples. Powder pressed into copper tape, or small 3 mm diameter hand-pressed pellets are loaded onto a sample bar. XPS spectra were collected on a Kratos Axis Ultra operating a monochromatic Al source at 15 kV and 10 mA.

2.3.7 Thermal Transport

Thermal conductivity describes a material's ability to conduct heat, which is dependent on temperature. This work utilizes a commercially available laser flash apparatus (LINSEIS LFA 1000) to measure the thermal diffusivity D and heat capacity at constant pressure C_p.

To prepare for measurement, a pressed pellet (either 10 mm or 12.7 mm in diameter) is ground to at least a smooth but shiny-matte finish (400-600-800 grit SiC paper). Both surfaces of

the pellet are coated with a thin layer of graphite spray to prevent reflection of the laser beam. Once loaded with a reference material (Pyroceram 9606), the chamber evacuated and an initial calibration setting of iris-aperture parameters, the measurement program begins to collect thermal diffusivity and C_p data. The sample is exposed to an IR laser, which then increases the temperature of the sample surface. A detector on the other side measures time for the temperature to rise. Based on the pellet thickness d, and $t_{1/2}$, the time to the half maximum of response, we can calculate the thermal diffusivity according to Equation 2-1.

Equation 2-1

$$D = 0.1388\frac{d^2}{t_{1/2}}$$

The software also requires the mass of the sample and mass of the reference, using them in conjunction with the applied laser energy to determine the C_p (in J/g°C) of the sample. Using the following relation, thermal diffusivity, Cp and sample density the calculation of the thermal conductivity is as follows in Equation 2-2:

Equation 2-2

$$\kappa = Dc_p\rho$$

The instrument's precision for thermal diffusivity data is +/- 5%.

2.3.8 Electrochemical Measurements: Cyclic Voltammetry and Galvanostatic Cycling

For the preparation of slurries with $Li_{4-x}CuS_2$ phases in Chapter 3, the as-synthesized phases are mixed with 5 wt% Polyvinylidine fluoride (Arkema, HSV761A) and 5 wt% Super P carbon (TimCal) in N-methyl-2-pyrrolidone (Sigma Aldrich) for 10 minutes in hardened steel jars using

a high-energy mill (SPEX SamplePrep 8000D). The slurry was then cast on copper foil (Alfa Aesar) with the thickness smoothed using a manual doctor blade. Electrodes were punched out using an arch punch. All processing was conducted in a glove box with argon working gas. The electrochemical measurement cell was prepared using Teflon Swageloks with Li-foil as counter and reference. Whatmann GF/D glass fiber filters were used as separators and soaked with 1 M $LiPF_6$ in 1:1 v/v ethylene carbonate:dimethyl carbonate (both from Sigm Aldrich) as the electrolytic solution. All measurements were conducted on a Bio-Logic SP-50 potentiostat.

Cyclic voltammograms were measured from 3.0 V to 1.7 V at a scan rate of 0.05 mV/s. Charge was calculated automatically by Bio Logic's EC-Lab software as area under the curve between the voltage limits of each cycle. The active material's mass was estimated by subtracting an average of ten punched out blank current collectors from the total electrode mass and then multiplying that difference by 0.9. The charge was divided by the estimated active material mass to obtain capacity.

For galvanostatic cycling, the lithium rich x = 3 sample was cycled at 0.1C-rate right after the CV curves. For the x = 2 composition, a different electrode was assembled into a half-cell for cycling because it exhibited the best performance through the CV testing. This half-cell was also cycled at 0.1 C-rate. The slow C-rate is to allow the electrochemical reactions be diffusion limited instead of kinetically limited. The potential window for the constant current cycling was set between 1.7 V and 3.0 V.

2.3.9 Electronic Transport

Seebeck coefficient and electrical resistivity were simultaneously measured on a commercially available four-point probe system (ULVAC-RIKO ZEM-3). Prismatic bars (~ 2

mm x 2mm x 7.5-9 mm) of each sample were cut from densified pellets using a silicon carbide slurry wire saw. Each side of the bar was polished to a mirror finish and mounted between the upper and lower electrode arms of the ZEM-3 with two thermocouple probes on the side as shown in Figure 2-3. To provide quality electrical contact between the upper and lower electrode arms with the sample, Grafoil pieces are placed at the prismatic bar ends. To test for contact quality with the bar and the thermocouple probes, the bar is loosely secured by the upper/lower electrode arms and its position is adjusted as the probes are brought closer to the bar. With correct alignment as spotted by human eye, the probes are brought into direct contact with the bar and the micrometer (which controls the probe) is turned three times. There is force from the probes applied onto the bar provided by springs within the system to provide electrical contact. Testing the contact quality involves running current through the PSU at room temperature and measuring voltage across the contact points with the probes. The system's multimeter readouts with incremental change in current applied should yield a linear I-V plot.

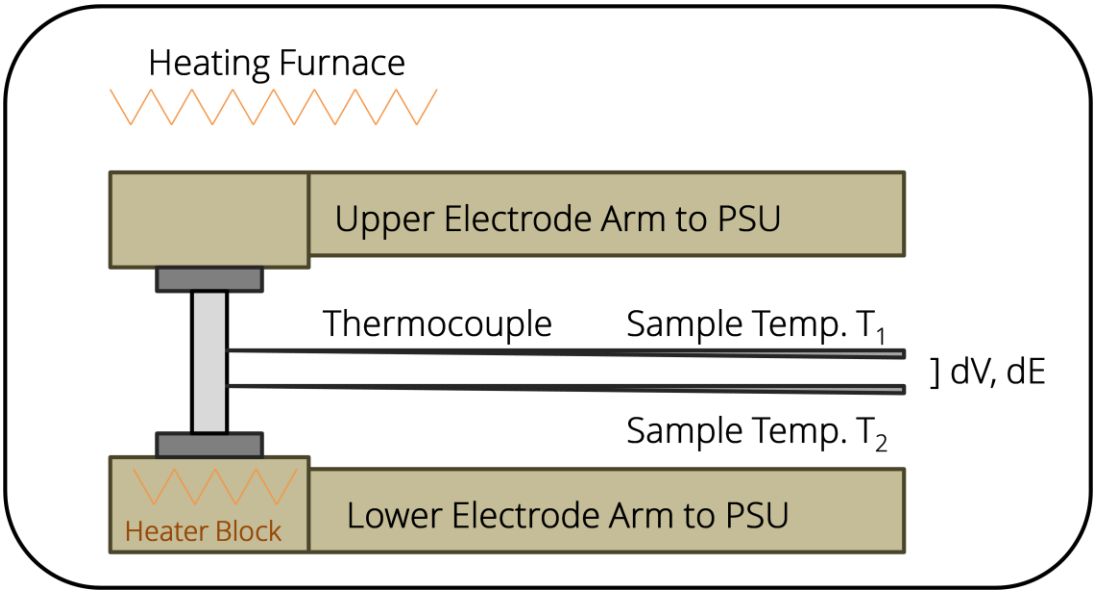

Figure 2-3 Schematic of ZEM-3 setup for simultaneous measurement of Seebeck coefficient and electrical resistivity.

To measure the the Seebeck coefficient, the heater block creates a temperature difference between top and bottom of the sample. Typical values for ΔT are 5, 10 and 15 °C for each base temperature step where they are the difference in temperature from base temperature at top and bottom.. The thermocouple probes measure T_1 and T_2. The dE comes from the thermal electromotive force through the bar. For resistivity, the constant power supply unit (PSU) supplies a constant current through the bar via the upper and lower electrode arms and dV can be measured between the thermocouples.

2.3.10 Scanning Electron Microscopy

Thin film samples were mounted on SEM stubs with carbon tape and then placed in an FEI Quanta 3D or FEI Nova Nanolab to take secondary electron images and take composition maps through their respective EDAX energy dispersive spectroscopy (EDS) detectors. SEMs raster an accelerated and focused beam of electrons across the surface of a sample. The interaction of the electrons with the sample's surface will primarily emit secondary electrons, back-scattered electrons (BSE), diffracted BSE, visible light and photons with characteristic X-rays. This work primarily uses the secondary electron detectors and EDS detectors in the aforementioned SEMs to collect secondary electron images and composition maps respectively.

2.3.11 UV-VIS-IR Spectroscopy for Band Gap Determination

Diffuse optical reflectance spectra are collected on a Varian Cary 5000 UV-vis-NIR spectrometer equipped with a Harrick Praying Mantis diffuse reflectance accessory. They are performed at Duquesne University under the direction of Professor Jennifer Aitken. Barium sulfate ($BaSO_4$) is used as the 100% reflectance standard. 2500 to 200 nm was scanned at a 600

nm/min rate.[97] The Kubelka-Munk relationship (Equation 2-3) was used to convert percent reflectance to absorption (α).[98]

Equation 2-3

$$\alpha / s = F(R) = \frac{(1-R)^2}{2R}$$

2.3.12 Interference-Enhanced Spectroscopic Ellipsometry

For the measurement of the index of refraction (n) and the extinction coefficient (k) of a thin film, a spectroscopic ellipsometer (J.A. Woollam Co. M-2000) is used. These measurements were performed with collaboration with Dr. Cheng Zhang under the direction of Professor Jay Guo. An ellipsometer contains a light source, a polarization generator, a sample stage, a polarization analyzer and a detector. The light source and polarization generator generate a monochromatic light beam which has linear polarization (equal s- and p-planes, in phase). When the beam interacts with the sample, it becomes elliptically polarized light. The polarization analyzer and detector are able to determine Ψ (related to a ratio of the s- and p- planes in the reflected light) and Δ (phase). The measurement is repeated for two additional incident angles φ. Mathematical models are required to generate the same signature from experimental data in order to extract n and k. Different parameters (n, k and film thickness) of the models are altered and then the Ψ and Δ are calculated from the model to check with experimentally measured Ψ and Δ to check for consistency. The model-fit cycles will continue until the Ψ and Δ from the model matches with the Ψ and Δ from experiment.[99]

In the case of another sought after quantity, film thickness, the film is required to be grown on a substrate with another thin film layer where the optical properties are well-known. This method is known as interference-enhanced method.[100] In this work, thin films are grown on 500 μm (100) silicon with 300 nm of thermal oxide on top. The additional thermal oxide layer

facilitates the decoupling of either film thickness or absorption coefficient contributions to Ψ and Δ. This experimental set up and modeling reveal the quantities n, k and film thickness.

The extinction coefficient (k) is then converted to absorption coefficient using the following relationship:

Equation 2-4 $$\text{Absorption Coefficient } \alpha = \frac{4\pi k}{\lambda} = 10{,}135{,}462Ek$$

The extinction coefficient is unitless and λ is in meters, which makes the absorption coefficient's units m^{-1}. The wavelength can also be first converted into energy (in eV) and then the calculation becomes multiplying a constant and two experimental variables together.

Chapter 3 Thermal and Electrochemical Behavior of $Cu_{4-x}Li_xS_2$ Phases

3.1 Introduction

CuS and Cu_2S are being investigated as promising cathode materials for applications in low-voltage Li and Na ion batteries[101-103]. For instance, previous studies focusing on the electrochemical performance of various Cu_2S-based cathode materials demonstrated relatively stable cycle performance with high specific capacity ranging from 230 mA*hr*g^{-1} for Cu_2S nanowire array on Cu substrate[101] to 270 mA*hr*g^{-1} for Cu_2S/tubular mesoporous carbon composite[102]. In these systems, it is suggested that during the first discharge process, Cu_2S reacts with Li ions to produce Li_2S and Cu metal according to the chemical reaction (Equation 3-1).

Equation 3-1
$$Cu_2S + 2Li^+ + 2e^- \rightarrow 2Cu + Li_2S$$

CuS with its high theoretical capacity of 560 mA*hr*g^{-1} and high electronic conductivity of 10^{-3} S/cm, is an attractive cathode material for high-powered rechargeable battery systems[104,105]. Several investigations of CuS as a cathode material in an Li/CuS coin cell revealed a large capacity of 530 mA*hr*g^{-1} during the first discharge followed by a rapid drop in the capacity in subsequent charge–discharge cycles[32,104,105]. However, the cathodic reaction mechanism during the charge–discharge process is still not clear. Early investigations suggested a two-step reaction where CuS reacts with Li ions to form Li_2S and Cu_2S according to reaction in Equation 3-2

followed by the reaction of Cu_2S with Li ions to generate Li_2S and Cu metal according the reaction in Equation 3-3 [34,106-110]

Equation 3-2 $$CuS + 2Li^+ + 2e^- \rightarrow Cu_2S + Li_2S$$

Equation 3-3 $$Cu_2S + 2Li^+ + 2e^- \rightarrow 2Cu + Li_2S$$

It was later proposed that the first discharge step consisted of the insertion of Li ions into the CuS crystal to form $CuLi_xS$ ($x < 2$) according to the reaction in Equation 3-4 followed by the decomposition of $CuLi_xS$ ($x < 1$) intermediate into CuS, Cu_2S and Li_2S according to the reaction in Equation 3-5[107,110,111].

Equation 3-4 $$CuS + xLi^+ + xe^- \rightarrow CuLi_xS$$

Equation 3-5 $$CuLi_xS \rightarrow (1-x)CuS + \frac{x}{2}Cu_2S + \frac{x}{2}Li_2S$$

At sufficiently low voltage, the Cu_2S formed in reaction (Equation 3-5) subsequently reacts with Li ions to produce Li_2S and Cu metal according the reaction (Equation 3-3). The above reaction mechanisms suggest that in addition to the operating voltage, the stability and reversibility of the charge– discharge process in Cu_2S/Li and CuS/Li half-cells may be related to the fraction, x, of Li incorporated into the cathode materials (Cu_2S or CuS) during the first discharge process. Therefore, determining the optimum fraction of incorporated Li that could favor a stable and reversible charge–discharge process with maximal capacity, under suitable experimental conditions, would drastically enhance the electrochemical performance of Cu_2S/Li

and CuS/Li half-cells paving the way for their widespread use as rechargeable Li-ion batteries in commercial devices. One elegant approach to address this problem is to synthesize lithiated Cu_zLi_yS phases, with controlled Cu:Li ratio and to investigate their electrochemical behavior of as cathode materials in Cu_zLi_yS/Li half-cells.

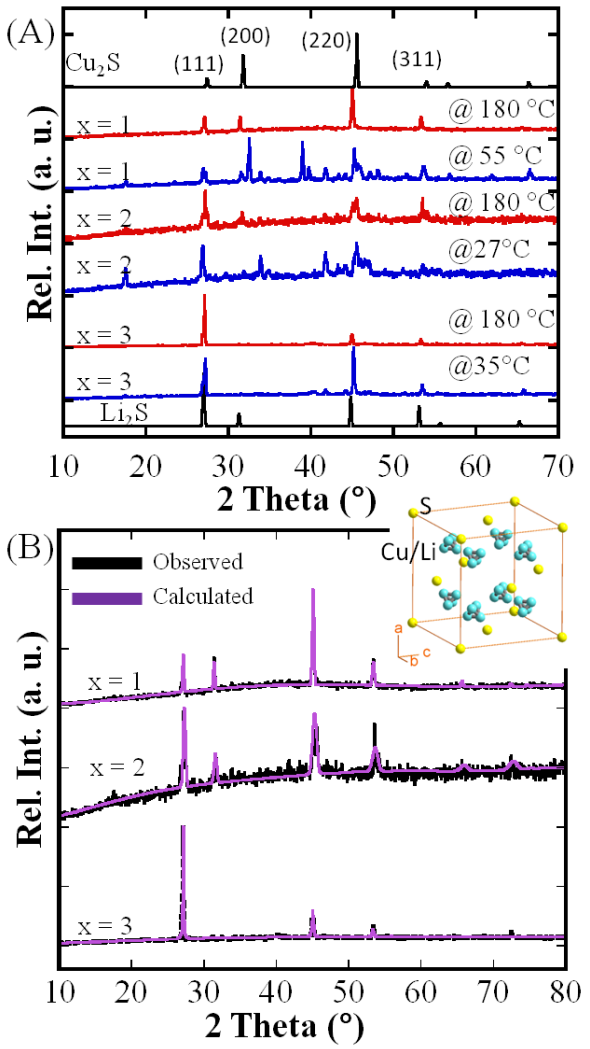

Figure 3-1: (A) Temperature dependent X-ray powder diffraction patterns of the $Cu_{4-x}Li_xS_2$ series compared with calculated powder patterns of Cu_2S and Li_2S. (B) Le Bail fitting of the high temperature X-ray powder patterns of Cu_3LiS_2 (x = 1), $Cu_2Li_2S_2$ (x = 2) and $CuLi_3S_2$ (x = 3). Inset: model structure of the $Cu_{4-x}Li_xS_2$ series at high temperature.

3.2 Synthesis of and Experimental Information on $Cu_{4-x}Li_xS_2$ Phases

For the $Cu_{4-x}Li_xS_2$ (x = 1, 2, 3) phases, stoichiometric amounts of Li_2S (Alfa Aesar 99%), S (Alfa Aesar, 99.9%) and Cu (Alfa Aesar, 99.9%) were ground in an agate mortar and inserted into Al_2O_3 crucibles (Almath, UK) which are then sealed in 14 x 16 mm ID x OD quartz tubes. The quartz tubes containing the phases were ramped to 300°C in 10 hours and maintained isothermal for 24 hours. This low temperature step allows for sulfur, the lowest melting element in the mixture, to react with the rest of the mixture containing much higher melting element and binary. After the 24 hour isothermal step, the furnace is ramped to 550°C in 5 hours and the samples are annealed

for another 72 hours. The furnace power was turned off to allow the samples to cool to room temperature. The quartz ampoules containing the samples are then broken open inside an argon-filled glovebox, extracted, reground and resealed in the same powder-crucible-quartz configuration. They were reheated again at 550°C at 100°C/hr and dwelled at that temperature for 72 hours before air-cooling to room temperature. These samples are stored in the glovebox to prevent reaction with air and moisture.

After synthesis, small amounts of ground samples were taken out for X-ray powder diffraction (PXRD), differential scanning calorimetry, pycnometry, laser flash and electrochemical measurements. The room temperature PXRD patterns were collected using a Rigaku Miniflex 600 with graphite monochromator operating Cu-Kα (λ = 1.54056 Å) at 40 kV and 15 mA in reflection geometry. High temperature XRD powder patterns were collected under vacuum using a Rigaku Ultima IV X-Ray diffractometer. The unit cell parameter and structure model for $Li_{4-x}Cu_xS_2$ (x = 1, 2, 3) phases were obtained by fitting the high temperature XRD patterns using the Le Bail method in the FullProf software package[93,94].

3.3 Results and Discussion

3.3.1 PXRD, Le Bail Fitting and DSC

The phase purity and structure of the synthesized compounds was probed using powder X-ray diffraction (XRD) at various temperatures shown in Figure 3-1a. A close comparison of the XRD patterns near room temperature for samples with various Cu:Li ratio (x values) suggests that $Cu_{4-x}Li_xS_2$ phases are not isostructural as each of the $Cu_{4-x}Li_xS_2$ phases adopts a unique crystal structure at room temperature. While the XRD pattern at room temperature of the sample

with x = 3 is comparable to that of the cubic structure of Li_2S, additional peaks observed on the XRD patterns of samples with x = 1 and x = 2 suggest lower symmetry structures for both phases near room temperature. Unfortunately, the exact structure type of these phases could not be

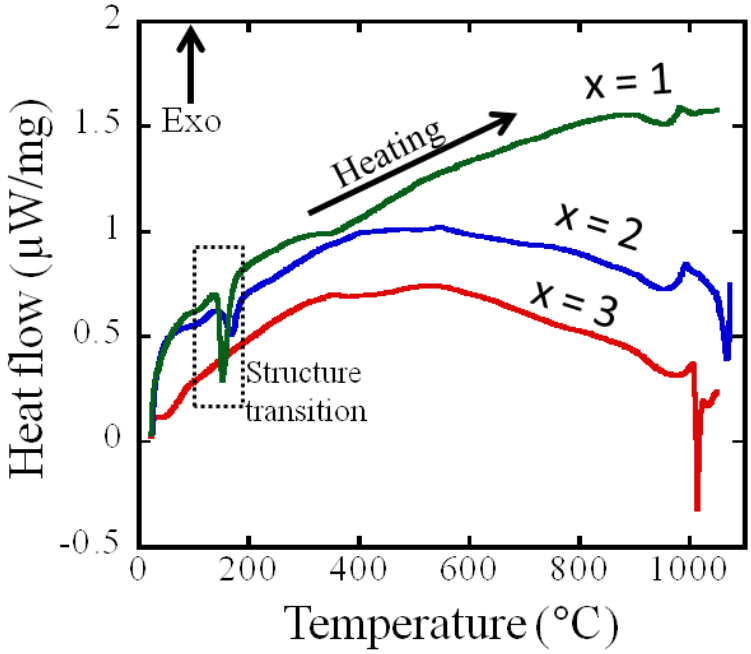

Figure 3-2: Differential scanning calorimetry (DSC) of $Cu_{4-x}Li_xS_2$ showing endothermic peaks of phase transition from low-symmetry structure to the high temperature cubic phase for x = 1 and x = 2.

accurately identified.

In order to assess the single-phase nature of the synthesized $Cu_{4-x}Li_xS_2$ phases, differential scanning calorimetry (DSC) was performed from 25 °C to 1150 °C. The DSC heating curves showed that the melting temperature (T_m) of the $Cu_{4-x}Li_xS_2$ phases decreases with increasing Li content (x value) from T_m > 1050 °C for x = 1 to T_m = 1000 °C for x = 3 (Figure 3-2). Interestingly, the DSC heating curves for the compositions with x = 1 and 2 showed an additional endothermic peak at ~140 °C. To probe the origin of this endothermic peak, XRD patterns of various $Cu_{4-x}Li_xS_2$ phases were collected at 180 °C (Figure 3-1). A careful comparison of the low temperature (T < 140 °C) and high-temperature (T > 140 °C) XRD

patterns of $Cu_{4-x}Li_xS_2$ phases with x = 1 and x = 2 indicate a transition from a low-symmetry structure at temperatures below 140 °C to a cubic structure at higher temperatures. Therefore, one can conclude from the combination of DSC and temperature dependent XRD data that the synthesized $Cu_{4-x}Li_xS_2$ samples are single-phase and adopt a cubic structure at temperatures above 140 °C.

Table 3-1 Le Bail fitting parameters and lattice parameter (a) from XRD patterns of $Cu_{4-x}Li_xS_2$ phases at 180°C. Density (ρ) and thermal conductivity (κ) of $Cu_{4-x}Li_xS_2$ phases are at room temperature.

Composition	x = 0	x = 1	x = 2	x = 3	x = 4
R_f	-	3.05	5.39	3.27	-
χ^2	-	1.80	3.04	3.04	-
a (Å)	5.628(6)[112]	5.706(2)	5.664(2)	5.705(2)	5.716(2) [113]
$\rho_{(Measured)}$ (g/cm^3)	-	4.57(2)	3.67(2)	2.75(2)	-
$\rho_{(Calculated)}$ (g/cm^3)	5.93[112]	4.68(2)	3.75(2)	2.66(2)	1.66 [113]
κ(W/m·K)	~1.0 [114]	0.7 (2)	1.0(2)	1.2(2)	-

The Le Bail fitting of the high temperature (at 180 °C) XRD patterns of $Cu_{4-x}Li_xS_2$ indicates that the compounds are isostructural with the end members Cu_2S (x=0)[112] and Li_2S (x=4)[113] (Figure 3-1b). Starting with the crystal structure of Cu_2S[112], acceptable matching between the intensity distributions of the high temperature XRD patterns of $Cu_{4-x}Li_xS_2$ samples and the calculated patterns (Figure 3-1b) was obtained by randomly distributing Cu and Li atoms in the metal positions occupied by Cu in the structure of Cu_2S. The fitting parameters, R_f and χ^2, as well as the calculated unit cell parameters of the high temperature cubic $Cu_{4-x}Li_xS_2$ phases are summarized in Table 3-1. To further confirm the purity of the synthesized $Cu_{4-x}Li_xS_2$ phases, we measured the "true" density of the polycrystalline powders and compared to the density calculated using unit cell parameters obtained from the fitting of the high temperature XRD data (Table 3-1). The small difference of less than ±3% between the measured and calculated density of $Cu_{4-x}Li_xS_2$ phases is within the precision (±5%) of our pycnometer suggesting successful

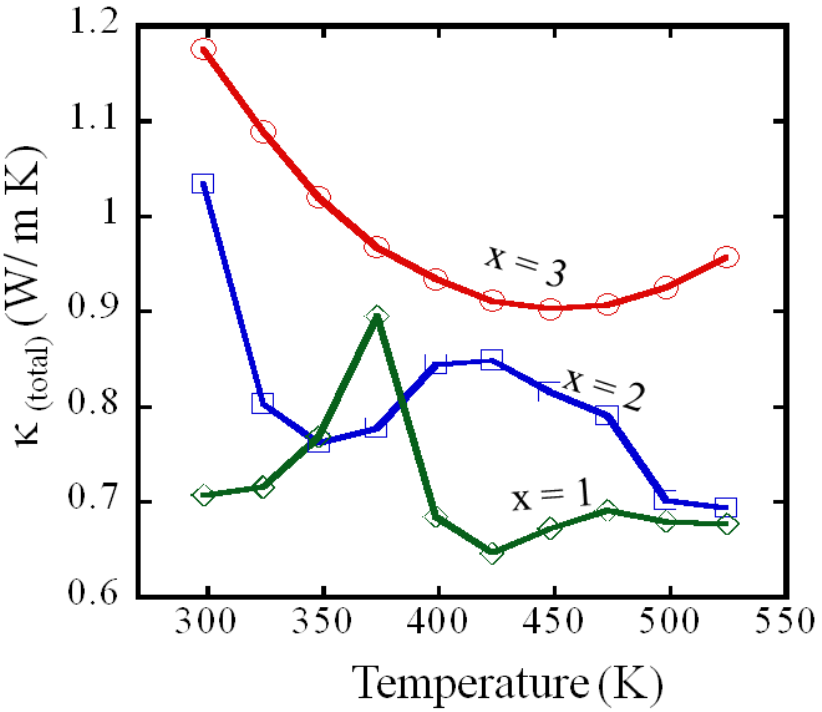

Figure 3-3 Temperature dependence of the thermal conductivity of the $Cu_{4-x}Li_xS_2$ phases

synthesis of high purity samples of $Cu_{4-x}Li_xS_2$ phases. It appears from the above analysis of XRD, DSC and pycnometry data, that at temperatures above 140 °C, the synthesized phase pure $Cu_{4-x}Li_xS_2$ materials are isostructural to Cu_2S (or Li_2S), whereas below 140 °C, compositions with x=1 and x=2 undergo structural rearrangement to a unique structure with lower symmetry.

3.3.2 Thermal Conductivity

The temperature dependence of the thermal conductivity of the synthesized $Cu_{4-x}Li_xS_2$phases is shown in Figure 3-3. At room temperature, the thermal conductivity increases with Li concentration (x-value) from 0.7 W/m K for x = 1 to 1.15 W/m K for the sample with x = 3. This trend is consistent with the reduction of Cu disorder in the $Cu_{4-x}Li_xS_2$ crystal lattice arising from

an increase in Li content. The thermal conductivity of $CuLi_3S_2$ (x = 3) decreases exponentially with rising temperature, reaching a minimum value of 0.9 W/m K at 450 K and increases thereafter with further increase in temperature. Below 450 K, the reduction in the thermal conductivity is associated to enhanced phonon scattering due to an increase in lattice vibrations with temperature. However, thermal activation of electrons to the conduction band above 450 K results in a bipolar conduction leading to a small increase in the total thermal conductivity with increasing temperature. For $Cu_{4-x}Li_xS_2$ compositions with x=1 and x=2, the temperature dependence of the thermal conductivity showed anomalous behavior around 410 K, which is associated to the structural transition from the low-symmetry phase below 410 K to the high temperature cubic structure. At this temperature, the transition of Cu atoms from ordered to disordered behavior in the crystal structure induces to a sudden large increase in the heat capacity leading

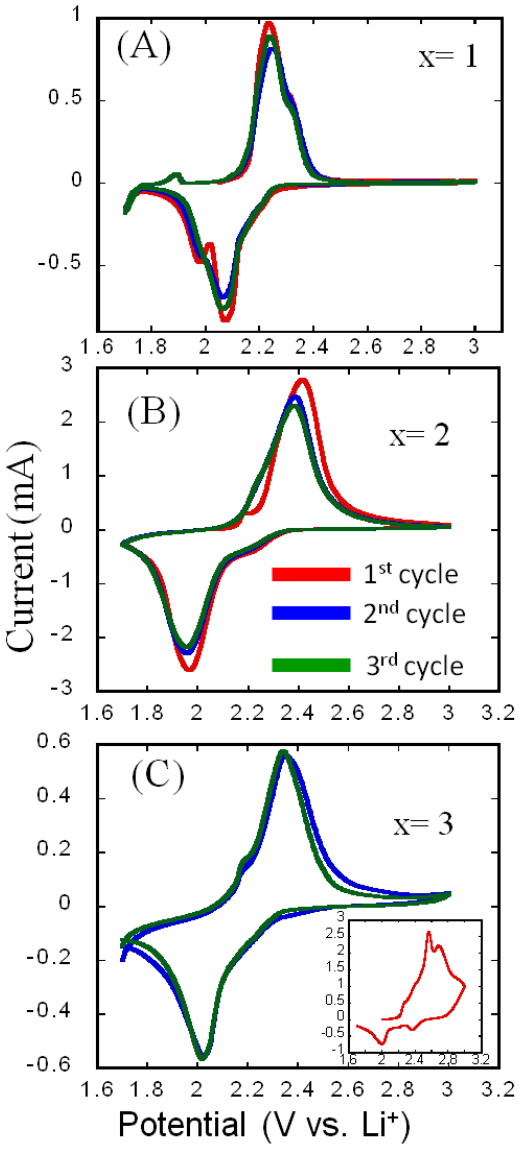

Figure 3-4 Electrochemical performance of $Cu_{4-x}Li_xS_2$/Li half-cells in the voltage range from 1.7 – 3.0 V vs. Li^+/Li through cyclic voltammetry.

to the observed increase in the thermal conductivity. Interestingly, the thermal conductivity of samples with $x = 1$ and $x = 2$ reach ~0.7 W/m K at 575 K. The drop in the thermal conductivity of both $x = 1$ and $x = 2$ samples above 410 K is presumably due to the large degree of Cu disorder in the cubic structure.

3.3.3 Electrochemical Behavior

To investigate the nature of the discrepancies observed in the electrochemical performance of various CuS/Li half-cells, we have performed cyclic voltammetry (CV) on various $Cu_{4-x}Li_xS_2$/Li half-cells (Figure 3-4). We observed that the stability of the charge–discharge process decreases with increasing Li content, whereas the charge capacity during the first cycle increases with Li content. For instance, the charge/discharge capacities observed during the first cycle are of 46 mA h g^{-1}/46 mA h g^{-1} for $x = 1$, 180 mA h g^{-1}/165 mA h g^{-1} for $x = 2$ and 93 mA h g^{-1}/91 mA h g^{-1} for $x = 3$.

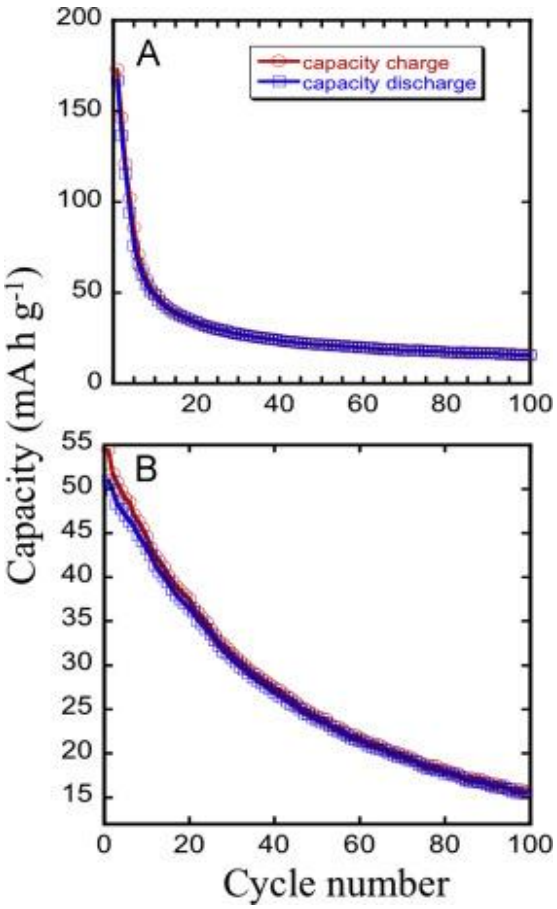

Figure 3-5 Galvanostatic cycling profile of the compositions x = 2 (A) and x = 3 (B) over 100 cycles at C/10.

These results indicate that the maximum capacity and reversibility of the charge/discharge process is achieved when the Cu/Li ratio in $Cu_{4-x}Li_xS_2$ is equal to unity ($x = 2$). Since promising

capacity was observed for compositions with x = 2 and x = 3, half-cells of both compositions were fabricated and their stability were tested by galvanostatic cycling measurements (100 cycles) at C/10 rate (Figure 3-5). The x = 1 composition was not tested galvanostatically because of its inherently low capacity from the CV measurement. For composition with x = 2 (Figure 3-5A), the galvanostatic cycling measurement was performed using a newly constructed half-cell. Therefore, the capacity measured at the beginning of the test was similar to the value extracted from the CV (173 mA h g^{-1}) curves. However, the capacity fades dramatically in 40 cycles to 20 mA h g^{-1} and appears to be more stable thereafter. For the composition with x = 3 (Figure 3-5B), the galvanostatic cycling (GC) test was performed on the same half-cell used for the CV experiment. This explains the small capacity of ~55 mA h g^{-1} (compared to the ~400 mA h g^{-1} from the CV experiment) measured at the beginning of the GC experiment. This indicates that much of the irreversibility occurred after the CV measurement so that there was much less active material in the half-cell at the beginning of the GC test. For both compositions, x = 2 and x = 3, the diminishing capacity with the cycling can be attributed to continuing loss of sulfur due to the formation of lithium sulfides and polysulfides, which decreases the amount of active material available for electrochemical energy storage and work[115]. However, given the much slower capacity fade with cycling after 40 cycles, observed for the composition with x=2 one can argue that the stability and reversibility of capacity during the charge/discharge of a $Cu_{4-x}Li_xS_2$/Li cell is related to possible cathodic chemical reactions. For example, starting from a Cu_3LiS_2/Li half-cell, a possible cathodic chemical reaction during the charge process is as follows:

Equation 3-6 $$Cu_3LiS_2 \rightarrow xCuS + xCu_2S + (1-x)Cu_3LiS_2 + xLi^+ + xe^-$$

The experimental capacity of 46 mA h g^{-1} during first charge indicates that x=0.4Li^+ ions are removed from the Cu_3LiS_2 structure leading to the formation of an equivalent amount of CuS. During the discharge process the electrochemically active CuS reacts with Li^+ions to form CuLiS accordingly to the reaction in Equation 3-7:

Equation 3-7 $$xCuS + xLi^+ + xe^- + xCu_2S + (1-x)Cu_3LiS_2 \rightarrow xCuLiS + xCu_2S + (1-x)Cu_3LiS_2$$

The newly formed CuLiS phase coexists with unreacted (1−x)Cu_3LiS_2 and the Cu_2S phase formed during the first charge process. The stability of subsequent charge/discharge cycles suggests a full removal/insertion of 0.4Li^+ ions between CuLiS and CuS accordingly to the reaction in Equation 3-8

Equation 3-8 $$xCuS + xLi^+ + xe^- \leftrightarrow xCuLiS \ (x = 0.4)$$

The reduction of Cu^{2+} in CuS to Cu^+ enables the insertion of an equivalent mole of Li^+ions. Therefore the low capacity observed for the Cu_3LiS_2/Li half-cell (Figure 3-4) arises from the small amount of electrochemically active CuS phase form during the first charge process.

When starting from the $Cu_2Li_2S_2$/Li half-cell, the cathodic reaction during the first charge process is as follows according to the reaction in Equation 3-9

Equation 3-9 $$Cu_2Li_2S_2 \rightarrow 2yCuS + (1-y)Cu_2Li_2S_2 + 2yLi^+ + 2ye^-$$

The experimental capacity of 180 mA h g^{-1} during the first charge indicates that $2y=1.4Li^+$ ions are removed from the $Cu_2Li_2S_2$ structure during the first charge process. The observed discharge capacity of 165 mA h g^{-1} suggests that approximately $1.3Li^+$ions are inserted into the electrochemically active CuS accordingly to the reaction in Equation 3-10

Equation 3-10

$$2y\mathrm{CuS} + (1-y)\mathrm{Cu_2Li_2S_2} + 2y\mathrm{Li^+} + 2y\mathrm{e^-} \rightarrow \mathrm{Cu_2Li_2S_2}$$

The removal a large fraction of Li^+ ions from CuLiS during the charge process and the nearly full reinsertion of Li^+ ions into CuS during discharge is presumably due to the ability to maintain the electroneutrality of CuLiS and CuS phases through the oxidation or reduction reaction between Cu^+ and Cu^{2+} as well as minimizing change in their crystal lattice during the charge–discharge process.

For the $CuLi_3S_2$/Li half-cell, a very large charge capacity of 393 mA h g^{-1} was observed suggesting that ~$2.2Li^+$ ions were removed from the $CuLi_3S_2$ structure during first charge. The corresponding cathodic reactions during the first charge process can be represented as follows with the following reaction in Equation 3-11:

Equation 3-11

$$\mathrm{CuLi_3S_2} \rightarrow \mathrm{CuS} + \mathrm{Li^+} + \mathrm{Li_2S} + \mathrm{e^-}$$

During the first discharge, the very low capacity of 91 mA h g^{-1} observed corresponds to the reinsertion of only ~$0.4Li^+$ ions into the structure of CuS while Li_2S is electrochemical inactive in this voltage window. The cathodic reaction during the first discharge can therefore be represented by the reaction in Equation 3-12

Equation 3-12

$$CuS + Li^+ + Li_2S + e^- \rightarrow CuLiS + Li_2S$$

Following the electrochemical data obtained from various $Cu_{(4-X)}Li_{(X)}S_2$/Li half-cell, one can conclude that the specific capacity and optimal stability of CuS/Li half-cell are related to the concentration, or flux, of Li^+ ions inserted during various discharge cycles. By maintaining a balance between the amount of Cu and Li (Li:Cu = 1:1) in the discharged material $CuLi_xS$, it may be possible to achieve a large reversible specific capacity and high stability upon charge–discharge of CuS/Li half-cell.

3.4 Conclusions

In summary, we have synthesized several compositions of the $Cu_{4-x}Li_xS_2$ series and investigated the effect of Cu:Li ratio on their crystal structure, thermal conductivity and the electrochemical performance of $Cu_{4-x}Li_xS_2$/Li half-cell. We found that each member of the series (x = 1, 2 and 3) has a unique XRD pattern at room temperature suggesting that the $Cu_{4-x}Li_xS_2$ series is not a solid solution of binary Cu_2S and Li_2S phases. The compositions with x = 1 and x = 2 crystallize with a low-symmetry structure at room temperature and undergo structural transformation to a cubic structure at temperatures above 140 °C. Le Bail fitting of the high temperature XRD patterns suggested that the compositions with x = 1 and x = 2 are isostructural to Cu_2S at temperatures above 140 °C whereas the lithium rich (x = 3) composition is isostructural to Li_2S in the measured temperature range and exhibits no phase transition until melting. Thermal transport data at 300 K suggest an increase in the thermal conductivity of $Cu_{4-x}Li_xS_2$ phases with decreasing Cu:Li ratio, which is attributed to a reduction in the degree of Cu-

disorder in the crystal structure. Upon increasing the temperature, the thermal conductivity of Cu-rich samples (x = 1 and x = 2) drastically decreases to ~0.7 W/m K, which is associated with enhanced phonon scattering arising from the superionic conductivity of Cu^{+} ions in the high temperature cubic structure of $Cu_{4-x}Li_xS_2$ phases. Cyclic voltammetry and galvanostatic cycling data from $Cu_{4-x}Li_xS_2$/Li half-cells showed that the stability of the charge – discharge process decreases with Cu:Li ratio (increasing x value) while the initial charge capacity increases with Cu:Li ratio. We observed that the optimum composition for maximum initial capacity and reversibility of the charge/discharge process is achieved when the Cu:Li ratio in $Cu_{4-x}Li_xS_2$ is equal to unity (x = 2). We attribute the observed electrochemical performance of CuLiS/Li half-cell (x = 2) to the ability to maintain the electroneutrality of CuLiS and CuS phases through the oxidation or reduction reaction between Cu^{+} and Cu^{2+} as well as minimizing change in their crystal lattice during the charge–discharge process. These findings demonstrate that maximum capacity and high stability of CuS/Li cells can be achieved by controlling the level of Li^{+} ions inserted during the discharge process.

Chapter 4 Cu_4TiSe_4: A Promising Photovoltaic Material with Ultra-Large Absorption Coefficient

4.1 Introduction

Solar-cell research has focused on the development of low-cost highly efficient materials. More recently popular material systems include metal-halide perovskite, organic-inorganic hybrid perovskite[116], and copper metal chalcogenides (CMC) such as $CuInSe_2$[15], $CuIn_{1-x}Ga_xSe_2$ (CIGS)[13,19]. The large absorption coefficient (at least 10^4 cm^{-1}) of these materials coupled with the ability to engineer their bandgap through chemical substitutions enable the realization of solar cells devices with power conversion efficiency exceeding 20%.[13,15,19,117,118] Although the efficiencies remain inferior to that of single junction solar cell devices such as crystalline silicon (25.6%),[119,120] and GaAs thin-film (28.8%),[121] the ability of perovskite solar cells[122-124] and CMC-based materials[125] provide a cost advantage that could pave the way to terawatt-scale deployment of photovoltaic technologies. Despite the promise of these material systems, thermal instability associated with hybrid perovskites[116], restriction on the use of heavy metals (Cd, Pb etc.) and the limited global supply for In are roadblocks to large scale deployment of the existing leading perovkite and chalcogenide-based technologies. To address these issues, earth abundant copper chalcogenides such as kesterites, $Cu_2SnZn(S,Se)_4$ (CZTS), obtained through chemical substitution of In^{3+} atoms in $CuIn(S,Se)_2$ by Zn^{2+} and Sn^{4+}, have been investigated.[125,126] However, the efficiencies of solar cell devices based on these materials remain around 12.6% due to unavoidable anti-site defects such as Cu_{Zn} and Zn_{Cu}.[10,127-129] Therefore, it appears that

achieving low-cost, earth-abundant copper chalcogenide solar cells with high efficiency requires the development of new chemical compositions and crystal structures rather than a simple variation of the chemistry of existing structures. Here, we report discovery of a new ternary phase Earth-abundant CMC, ternary copper titanium selenide, Cu_4TiSe_4 (may also be referred to as "CTSe" herein), and demonstrate its potential as a promising light-absorber for ultra-thin low-cost high-effiency solar cells.

4.2 Synthesis and Experimental Information for Cu_4TiSe_4

4.2.1 Synthesis by Solid State

Elemental powders of copper (99.5%, Alfa Aesar), titanium (99.5%, Alfa Aesar) and selenium (99.5% Sigma Aldrich) were weighed out in a stoichiometric ratio of 4:1:4 and ground in an agate mortar until homogeneous. The mixture was then flame-sealed in an evacuated (~10^{-3} Torr) quartz tube and placed in the furnace. The furnace was first ramped to 300 °C over 10 hours and held steady for 24 hours to allow the selenium to react with the rest of the elements. Then the temperature was increased to 550 °C, held for 120 hours and subsequently, the ampoules were cooled to room temperature over 24 hours. The sintered powder product was reground in the agate mortar and then resealed in quartz tubes. The temperature profile for the second annealing was up to 700 °C over 7 hours and held there for 168 hours before being cooled down to room temperature over 24 hours. For single crystal growth, 250 mg of the product was sealed and annealed at 800 °C for 10 days, just below the major transition in the DSC. After single crystal growth, a suitable crystal was picked and mounted onto a thin glass

fiber attached to a hollowed aluminum rod. A suitable crystal has at least regular geometry (square, triangular or hexagonal) facets that are shiny or reflective of light.

4.2.2 Thin Film Fabrication

A one-inch diameter and three-eighths inch thick target was produced by cold pressing and annealing as-synthesized Cu_4TiSe_4 powder. The powder was loaded into a steel die between two

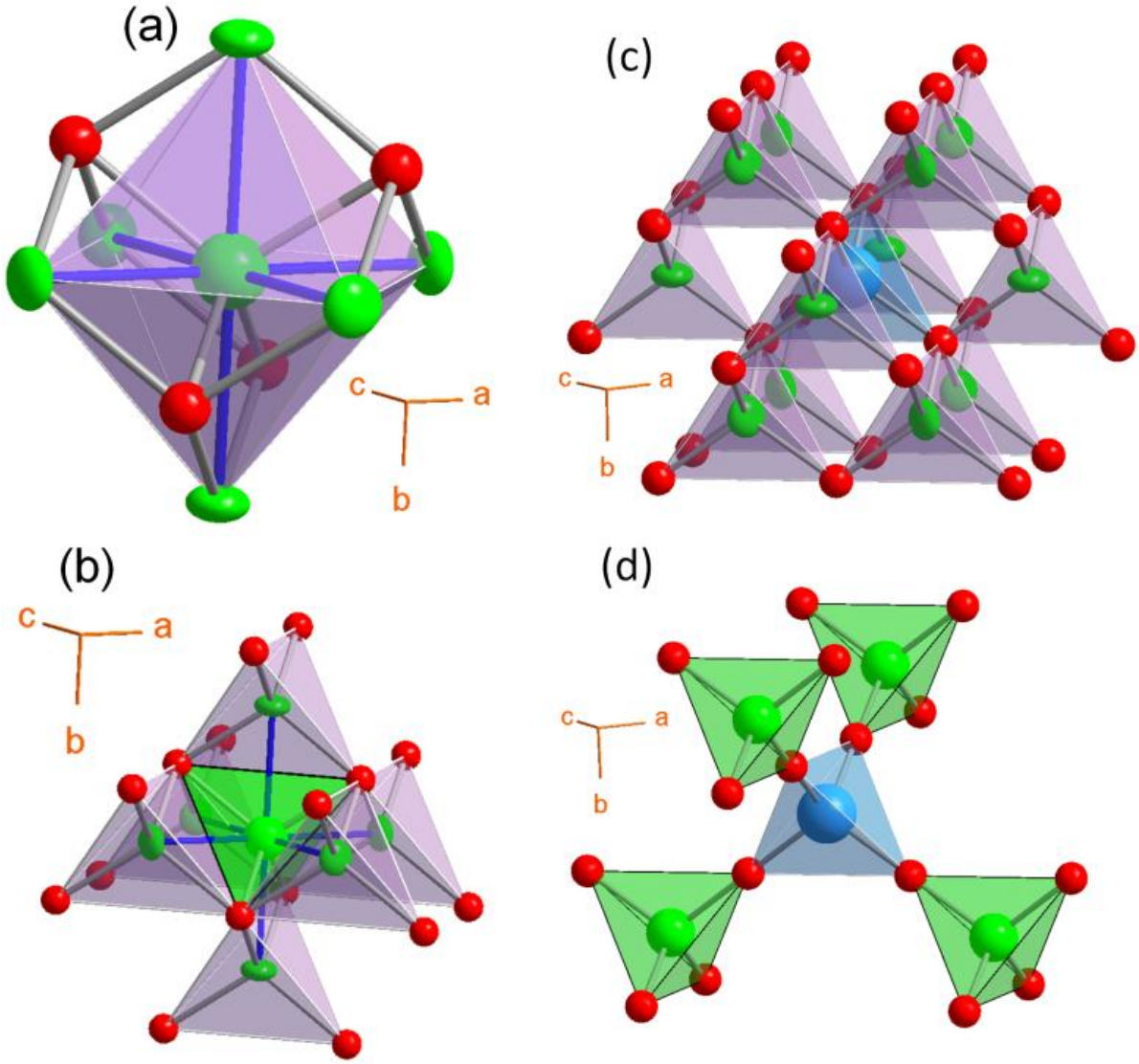

Figure 4-1:Coordination environment of metal atoms in CTSe structure. a) $[Cu_4Se_4]^{4-}$ anionic cluster consisting of a Cu-centered hexanuclear octahedral $[Cu]_6$ cluster capped by Se atoms on four of the eight triangular faces; b) environment of Cu(1) and Cu(2) and their connectivity within the $Cu_4Se_4]^{4-}$ anionic cluster. $Cu(2)Se_4$ tetrahedron share all edges with $Cu(1)Se_4$ tetrahedra, $Cu(1)Se_4$ tetrahedra exclusively share corners with each other and $Cu(2)Se_4$ tetrahedra are isolated from each other; c) $TiSe_4$ tetrahedron shares only corners with $Cu(1)Se_4$ tetrahedra; d) $TiSe_4$ tetrahedron shares only corners with $Cu(2)Se_4$ tetrahedra and TiSe4 tetrahedra are isolated from each other.

sheets of Grafoil and consolidated under ambient atmosphere. The target was hydraulically pressed in a steel die at 395 MPa and subsequently annealed at 300 ºC for 8 hours in a vacuum furnace. After cooling to room temperature, the target's surface was ground with SiC paper (320-400-600-800-1000 grit) to remove the Grafoil and give the target's surface a matte finish. After target and substrate (500 μm Si with 300 nm thermal oxide, obtained from the collaborator Dr. Cheng Zhang from Prof. Jay Guo's laboratory) was loaded into a Thermionics deposition chamber and base pressure of ~10^{-6} mbar was achieved. Argon was flowed in to raise the chamber pressure to 7.4 x 10^{-3} mbar. The substrate was heated to 500 ºC at a rate of 20 ºC per minute. The target was pre-ablated with 300 shots at 2 Hz with KrF exciplex laser applying an average fluence of 2.6 J/cm^2. For film growth, 6000 shots at 5 Hz were applied to the target.

4.2.3 Single Crystal X-Ray Diffraction

A single crystal of CTSe, with approximate dimensions 0.05 × 0.05 × 0.05 mm^3 obtained from the high temperature annealing step was mounted on the tip of a glass fiber using epoxy glue. Intensity data were collected at 300 K on a STOE IPDS-2T diffractometer using a graphite-monochromated Mo-Kα radiation (λ = 0.71073 Å). The intensity data was indexed in the face centered cubic (FCC) Bravais lattice with unit cell parameter *a* = 11.2936(2) Å, and eight formula units per unit cell (Z = 8). The structure solution was obtained by direct methods in the space group *F*-43*c* (No. 219) and refined by full-matrix least-squares techniques using the SHELXTL software package.[95,96] The asymmetric unit cell contains three crystallographically independent metal positions M1(24*d*), M2(8*a*) and M3 (8*b*) and one Se atom position (32*e*). In the initial refinement cycle, Cu atoms were located at 24*d* (Cu1) and 8*b* (Cu2) sites with Ti occupying the 8*a* site. The refinement of this model resulted in R_1 = 7.5%. However, the atomic

displacement parameter of Ti was four times larger than that of Cu1 and Cu2. By exchanging the position of Cu2 (8*a*) and Ti (8*b*) atoms, the electroneutrality of the compound is maintained and the refinement of this model yielded R_1 = 5.1% with the atomic displacement parameter of Ti dropping by 50%. In the final refinement iteration, secondary extinction correction and anisotropic displacement parameters were included for all atoms.[95,96] This resulted in a final R_1 ~ 4%. The final charge-balanced composition of the crystal obtained from the refinement was $(Cu^{+})_4(Ti^{+4})_(Se^{-2})_4$. The assigned oxidation states of Cu and Ti atoms were also confirmed by bond valence sum (BVS) calculations. Additional details on the structure refinement and summary of crystallographic data are given in Table 4-1. Table 4-2 provides atomic coordinates and isotropic displacement parameters of all atoms and Table 4-3 summarizes selected inter-atomic distances. The graphical representation of the crystal structure was created using the graphical software Diamond[130] with ellipsoid representations (98% probability level) for all atoms.

Figure 4-1 shows the coordination environment and connectivity between various metal tetrahedra in the crystal structure of CTSe. Similar to the structure of most copper selenide based solar absorber materials such as $Cu_2ZnSn(Se,S)_4$ (CZTSeS) and $CuInSe_2$ (CIS), all metal atoms adopt tetrahedral coordination with Se.[125,126] The only substantial structural difference between CTSe and on the zinc blende structures is in the three dimensional (3D) connectivity of metal tetrahedra. In CIS, CIGS and CZTSSe, the 3D network is exclusive formed by corner sharing between tetrahedrally coordinated metal atoms (Cu, Sn, In, Zn or Ga), while metal tetrahedra ($CuSe_4$ and $TiSe_4$) in CTSe share both edges and corners in all directions to build the 3D framework of $[Cu_4Se_4]^{4-}$ anionic clusters (Figure 4-1). The edge-sharing observed between $Cu(1)Se_4$ and $Cu(2)Se_4$ tetrahedra in the structure of CTSe presumably results from the smaller

fraction of structural vacancies in the compound when compared to zincblende structure. For example, a unit cell of CTSe is equivalent to eight unit cells (2x2x2 superstructure) of a *fcc* (faced centered cubic) lattice Se atoms in which 5/8 of the tetrahedral sites (total of 40 tetrahedral sites per unit cell of CTSe) are occupied in an ordered fashion by Cu and Ti, whilst the remaining 3/8 (24 sites) are vacant. In an equivalent 2x2x2 superstructure of $CuInSe_2$, the *fcc* lattice is formed by Se atoms with half (32 sites) of the available tetrahedral site occupy by Cu/In (50/50). The larger fraction of occupied tetrahedral sites in CTSe structure results in edge-sharing and corner-sharing tetrahedra, whereas only corner-sharing connectivity between tetrahedral is observed in zincblende structures. This difference in the fraction of occupied tetrahedral sites and connectivity between tetrahedra leads to a slightly higher density for CTSe (5.69 gcm^{-3}) and higher structural stability when compared to cubic (sphalerite) $CuInSe_2$ (5.57 g/cm^{-3}),[16] which exhibits structural transition to higher density (5.77 g/cm^{-3}) low symmetry chalcopyrite structure at room temperature.[131] The Cu – Se bond distances in CTSe range from 2.4328(2) Å for Cu(2) – Se to 2.4407(6) Å for Cu(1) – Se, which is comparable to the Cu – Se bond length of 2.435 Å observed in $CuInSe_2$. The Ti – Se bond length of 2.4584(2) Å is 3.7% shorter than the bond distance of 2.553 Å reported in $TiSe_2$.[132]

4.2.4 Powdered X-Ray Diffraction

Powdered X-ray diffraction patterns were recorded on a Rigaku Miniflex 600 with graphite monochromator operating Cu-Kα (l = 1.54056 Å) at 40 kV and 15 mA in reflection geometry. The scan condition was from 10° 2θ to 70° 2θ at 2°/second. To check the films grown on SiO_x/Si substrate, diffraction patterns were recorded on a rotating anode Rigaku Rotoflex operating at 40 kV and 100 mA. Resultant powder patterns were loaded into MDI JADE 2010 and compared

with patterns in the PDF-4+ database as well as a simulated powder pattern from the single crystal solution.

Table 4-1: Selected crystallographic data for Cu_4TiSe_4 at 300 K.

Crystal system; space sroup	F-43c; (219)
Formula weight (g/mol)	1235.8
Density (ρ_{cal}) (g/cm^3)	5.69815
Lattice parameter (Å) $a = b = c$	11.2936(13)
Volume (Å^3); Z	1440.45(29); 4
Crystal size (mm)	[0.05] x [0.05] x [0.05]
Crystal shape, color	Faceted cubic, dark gray
Radiation (Å)	$\lambda(MoK_\alpha) = 0.71073$
μ (cm^{-1})	327.8
Diff. electron density (e/ Å^3)	+2.20 to -1.78
Transmission factor	0.2997 – 0.6709
2range; index range	$6.2° \leq 2\theta \leq 59.80°$; $-15 \leq h \leq 15$; $-15 \leq k \leq 15$; $-14 \leq l \leq 15$
R_1 (Fo>4σ(Fo))[a]	0.0414
wR_2 (all)[b]	0.1025
Goodness of fit	1.030

[a] $R_1 = \Sigma||F_o|-|F_c||/\Sigma|F_o|$; [b] $wR_2 = [\Sigma w(F_o^2-F_c^2)^2/\Sigma w(F_o^2)^2]^{1/2}$

Table 4-2: Atomic coordinate,s Wyckoff positions (W.P.), site occupancy factors, and equivalent isotropic displacement parameters (U_{eq} in $Å^2$) for all atoms in Cu_4TiSe_4.

Atom	W.P.	S. O. F.	*X*	*Y*	*Z*	U_{eq}
Se1	32e	0.33333	0.12432(8)	0.12432(8)	0.12432(8)	0.01274
Cu2	24d	0.25000	¼	0	0	0.01536
Cu1	8a	0.08333	0	0	0	0.02828
Ti1	8b	0.08333	¼	¼	¼	0.04238

U_{eq} is defined as one-third of the trace of the orthogonalized U_{ij} tensor.

Table 4-3: Selected inter-atomic distances in Cu_4TISe_4

Bond Type	Bond Distance (Å)
Cu2-Se1$^{iii, iv, v}$	2.4407(6)
Cu1-Se1^{iii,vii,viii}	2.4318(2)
Ti1-Se1$^{xi, xii, xiii}$	2.4584(2)

Operators for generating equivalent atoms:
(i) y, z, x; (ii) z, x, y; (iii) x, −y, −z; (iv) 0.5−y, x, −z; (v) 0.5−y, -x, z; (vi) 0.5+y, x, z; (vii) −x, y, −z; (viii) −x, −y, z; (ix) −y, z, -x; (x) z, −x, −y; (xi) x, 0.5−y, 0.5-z; (xii) 0.5−x, 0.5−y, z; (xiii) 0.5−x, y, 0.5−z.

To assess the phase purity and structure of the as-synthesized bulk polycrystalline powder and the PLD fabricated thin-films of CTSe, X-ray diffraction patterns were recorded and

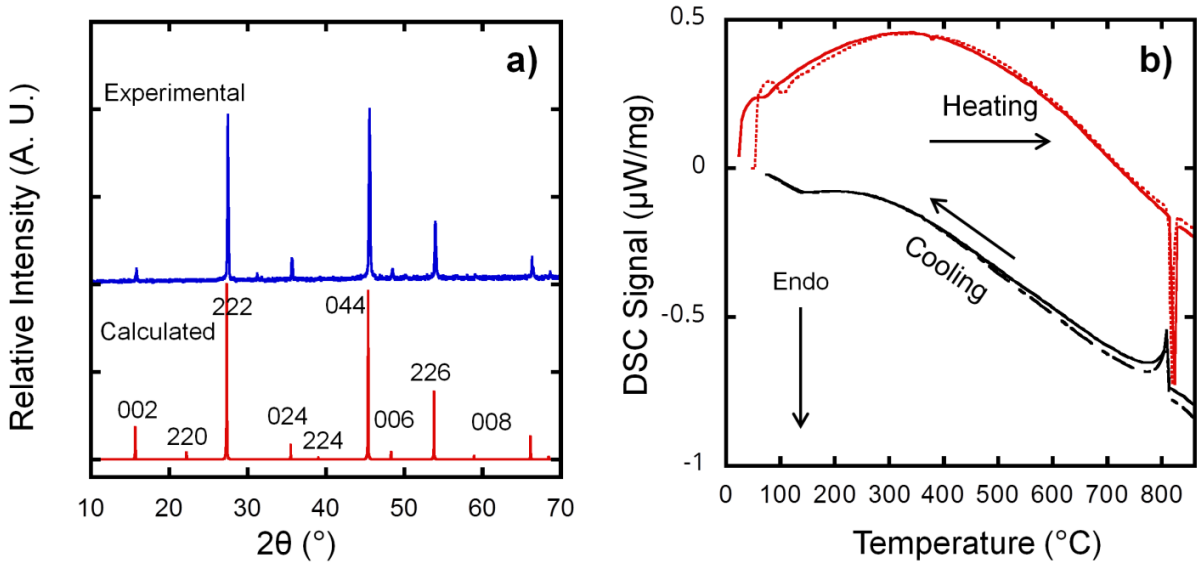

Figure 4-2: a) Powered X-ray diffraction of the synthesized polycrystalline powder of CTSe compared to theoretical pattern calculated using single crystal data. The excellent matching in both peak position and relative intensity indicates successful synthesis of single-phase powder of CTSe. b) Differential scanning calorimetry (DSC) heating and

compared to the theoretical pattern of CTSe calculated using single crystal structure data (Figure 4-2 and Figure 4-3). The powder patterns for the bulk powder samples were collected in reflection geometry on a Rigaku Miniflex 600 powder diffractometer operating under 40 kV and 15 mA using a monochromated Cu-Kα radiation (λ = 1.5418 Å). XRD patterns for the films grown on SiO_x/Si substrate were recorded on a rotating anode Rigaku Rotoflex operating at 40 kV and 100 mA. As shown in Figure 4-2a, there is a promising match in both the position and relative intensity of various peaks observed on the experimental diffraction of the as-synthesized polycrystalline CTSe powder and the simulated powder diffraction pattern calculated using single-crystal data. This suggests successful large-scale synthesis of bulk polycrystalline powder of CTSe as single-phase.

The phase purity of the synthesized CTSe polycrystalline powder was also confirmed through measurement of the true density using He gas pycnometry (Quantachrome Ultrapyc 1200e MUPY-30 pycnometer). Hand pressed pellets of CTSe was loaded into the sample chamber with known volume and He gas was used to flow purge and pressurize the chamber to 15 psi. The volume of CTSe extracted from this measurement along with the sample weight enabled the calculation of the true density, which was found to be 5.77(6) gcm^{-3}. This value is comparable, within the instrument precision of 5%, to the theoretical density of 5.69(8) gcm^{-3}, confirming the single-phase nature of the synthesized CTSe polycrystalline powder.

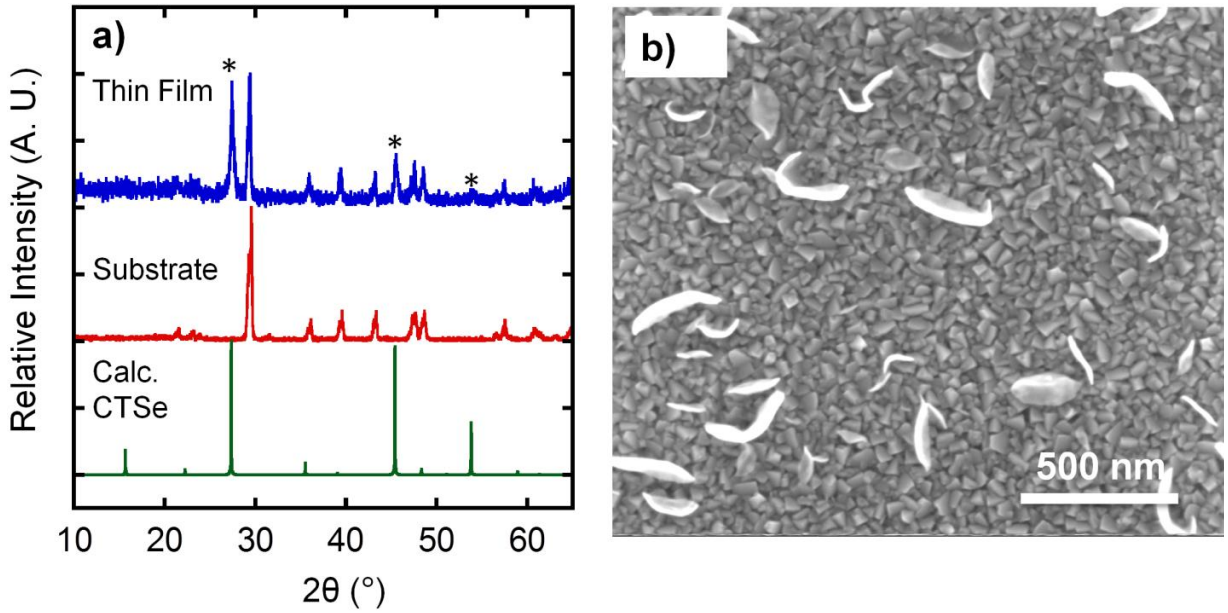

Figure 4-3: a) Powder X-ray diffraction patterns of PLD-deposited CTSe film compared to the X-ray diffraction pattern of the bare substrate and the theoretical pattern calculated from single crystal data. The asterisks (*) indicate peaks from CTSe. b) Scanning electron microscopy (SEM) image of CTSe film deposited using PLD, revealing the uniform grain size and morphology.

A comparison of the diffraction pattern obtained from the PLD deposited thin-film of CTSe (Figure 4-3a) with the diffraction patterns of bare substrate and the theoretical pattern from

single crystal data suggests successful formation of CTSe thin-film using PLD technique. All diffraction peaks from CTSe thin film can be associated to peaks from the bare substrate (thermal oxide + silicon) and high intensity peaks from the theoretical pattern of CTSe. Careful comparison of the relative intensity of the observed (222) and (044) peaks from the XRD pattern of CTSe thin film to the corresponding peaks on the theoretical pattern of CTSe revealed a preferential growth along (222) plane. The microstructure of the PLD deposited film was also examined using scanning electron microscopy (SEM). SEM analysis was performed using a Philips XL-30 with a tungsten filament and operating at 20 keV. The deposited CTSe thin film consists of densely packed prismatic grains with uniform particle size of approximately 70 nm (Figure 4-11b).

4.3.5 Chemical Analysis

The chemical composition of the synthesized powder of CTSe was determined using wavelength dispersive X-ray fluorescence (XRF) spectroscopy. Polycrystalline powder of CTSe was suspended onto Chemplex XRF cup with 0.3 μm thick Prolene film. The specimen was loaded into a Rigaku Supermini200 equipped and data collections were performed using Pd source (operating at 50 kV, 200 W) under flowing helium gas. The resulting composition in atomic percent is Cu (45.9%), Se (43.7%) and Ti (10.4%), which is comparable to the nominal atomic percentages of 44%, 44% and 11% for Cu, Se, and Ti, respectively. Similar composition (within the precision of the respective techniques) was obtained from the energy dispersive spectroscopy (EDS) analysis of hot pressed pellet of the synthesized materials used as target for the fabrication of CTSe thin film using pulse laser deposition technique. EDS analysis of the target (post-deposition) performed using scanning electron microscope (SEM, FEI Nova

Nanolab) confirmed the chemical composition of the target as Cu (47.8% +/- 0.7%); Ti(10.5% +/- 0.1%); Se(41.7% +/- 0.6%), which is consistent with the composition of the starting polycrystalline powder sample. The stoichiometry of the deposited film was also determined by EDS analysis and the measured atomic composition of Ti (11% ± 0.5), Cu (41% ± 3) and Se (48% ± 3) is consistent with the composition of the starting target.

4.3.6 DSC

The thermal stability and phase purity of the synthesized polycrystalline powder of CTSe was probed using differential scanning calorimetry (DSC). Approximately 30 mg of finely ground polycrystalline powder were sealed inside a small quartz tube (2 mm x 3 mm) under a residual pressure of 10^{-3} Torr. A sealed blank quartz tube was used as the reference. The measurement was performed from room temperature to 850º C in two heating and cooling cycles under flowing nitrogen gas. Heating and cooling curves on both cycles showed a single endothermic thermal event at 820 ºC and a single exothermic event as the same temperature, indicating a congruent melting and crystallization of the compound (Figure 4-2b). In addition the similarity of the DSC curves in both heating and cooling cycles confirmed the thermal stability of the structure.

4.2.7 Ellipsometry and Tauc Fitting

A spectroscopic ellipsometer (J.A. Woollam Co. M-2000) is used to measure the index of refraction (n) and the extinction coefficient (k) of CTSe thin film. The measurement was carried out at three incident angles of 55°, 65°, and 75°. The ellipsometer measures the amplitude and phase difference of the s- and p-polarized light after their reflection off the sample. Afterwards, an inverse calculation (modify parameters n, k, and film thickness, compare with experimental

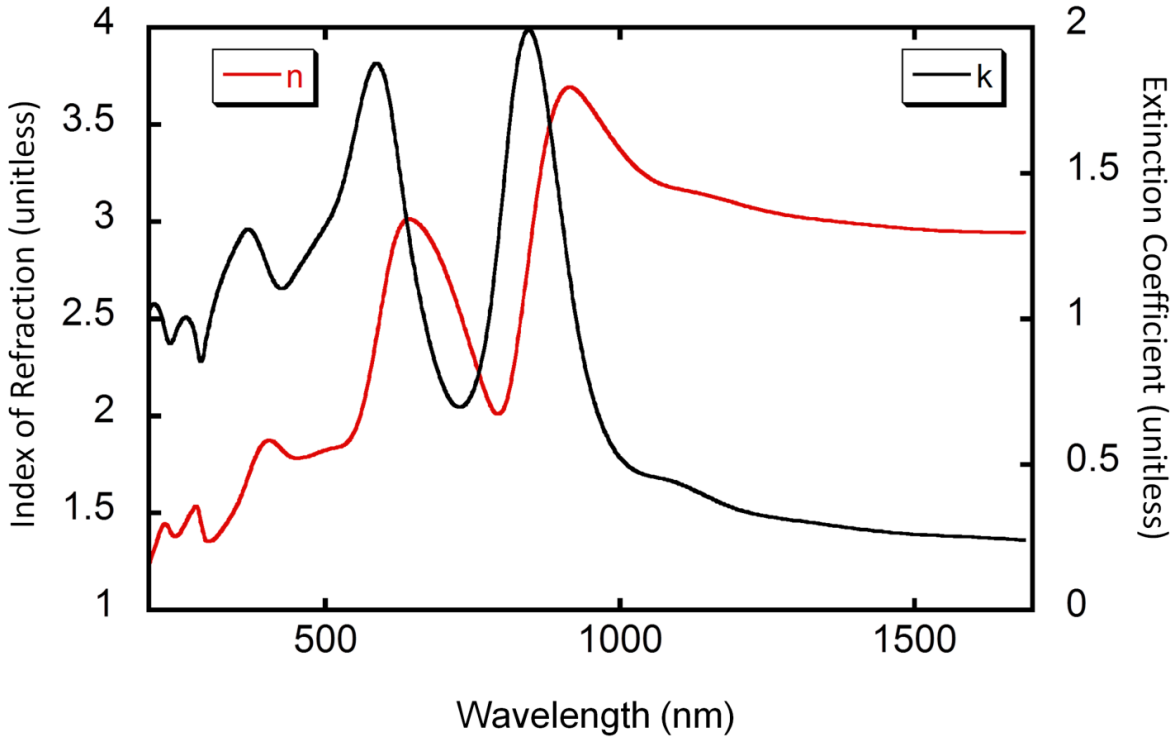

Figure 4-4: Index of refraction (n, red) and the extinction coefficient (k, black) as a function of wavelength exctracted from ellipsometry data.

data, and refine parameter cycles) was done in order to extract the optical properties of the film.

Since the deposited CTSe film is thin and semi-transparent in certain wavelength ranges, the incident light will penetrate through the film and reach the Si substrate. In order to separate the effect of light absorption by the Si substrate, and accurately determine the refractive index of the deposited CTSe thin-film, a thin layer (~300 nm) of thermal oxide was first deposited on the Si

substrate prior to the CTSe film deposition. The additional thermal oxide layer facilitates the decoupling of either film thickness or absorption coefficient contributions to Ψ and Δ, by providing additional reflected light, and thus, additional information for an accurate evaluation of the refractive index and thickness of the CTSe film during the ellipsometry data fitting process (interference enhancement method).[133,134] The ellipsometry data was fitted with a B-spline model that takes into account the Kramers–Kronig relation. This experimental setup and modeling

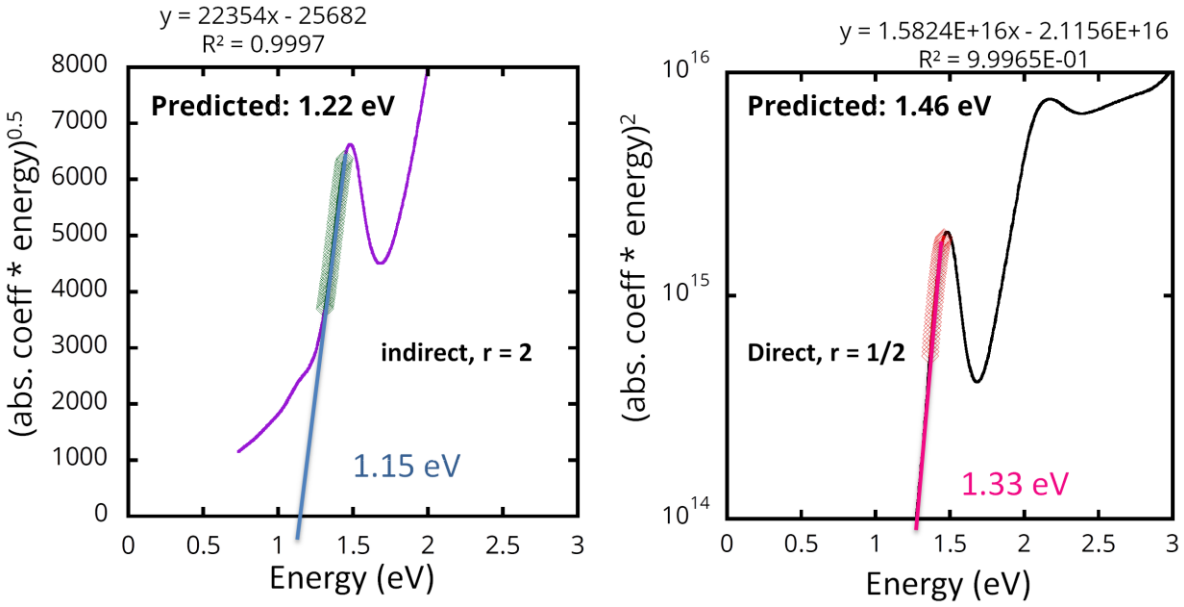

Figure 4-5: Tauc analysis for the determination of optical band gap. a) indirect (r = 2) and b) allowed direct (r = ½)

determine the quantities n, k and the film thickness. The index of refraction n and the extinction coefficient k are shown in Figure 4-4. Ellipsometry measurements were obtained by Dr. Cheng Zhang from Prof. Jay Guo's group in the Electrical Engineering and Computer Science department at the University of Michigan.

4.2.8 Absorption Coefficient and Optical Band Gap

Using the extinction coefficient (k) determined from the fitting of the spectroscopic ellipsometry data (Figure 4-4), we are able to calculate the absorption coefficient using the

expression $\alpha = 4\pi k/\lambda = 10{,}135{,}462Ek$, where α is the absorption coefficient in inverse meters, k is the extinction coefficient, and E is energy in eV. The absorption coefficient is then used for Tauc analysis[135] using the equation $y = (\alpha h\nu)^{(1/r)}$, where h is Planck's constant, ν is frequency and r is a constant (r = 2 for allowed indirect transition and r = ½ for direct allowed transition). Fitting the linear portion of the transformed absorption coefficient vs. energy curve enabled determination of both direct and indirect band gaps as the linear regression's x intercept as shown in Figure 4-5a and Figure 4-5b.

4.3.9 Electronic Transport Measurement

Specimens for simultaneous measurement of the thermopower and electrical conductivity were fabricated by pressing polycrystalline CTSe powder with a uniaxial hot press using graphite dies and plungers. 100 MPa of pressure was applied with the hydraulic system and the furnace shell was evacuated and flushed with argon several times before maintain a constant 20 L/min flow of argon for the remainder of the pressing time. The furnace temperature was increased to 450 ºC at a scan rate of 200 ºC/hr, dwelled for 4 hours and finally ramped down to room temperature at 100 ºC/hr. rectangular bars specimen, ~2.0 x 2.1 x 9.5 mm, were cut from the pressed pellets using a wire saw and SiC slurry, then polished to mirror finished using SiC papers. The upper/lower arm contacts with the sample bar have Grafoil sheets to provide uniform contact. The thermocouple probes are in direct contact with the bar with the electrical contact quality supplied by the springs from the measurement system (See Chapter 2 for more detail). The thermopower and the electrical resistivity were measured simultaneously from room temperature to 525 ºC using an ULVAC-RIKO ZEM-3 apparatus (4-point measurement). The instrument's precision on the electrical resistivity and the Seebeck coefficient data is ± 4%.

CTSe exhibits p-type semiconducting behavior as indicated by the positive values of the thermopower and the nearly exponential increase in the electrical conductivity with increasing temperature (Figure 4-6). The thermopower rapidly increases from 30μV/K at 300 K to 200 μV/K at 800 K. The electrical conductivity initially remains constant at 1 S/cm from 300K to

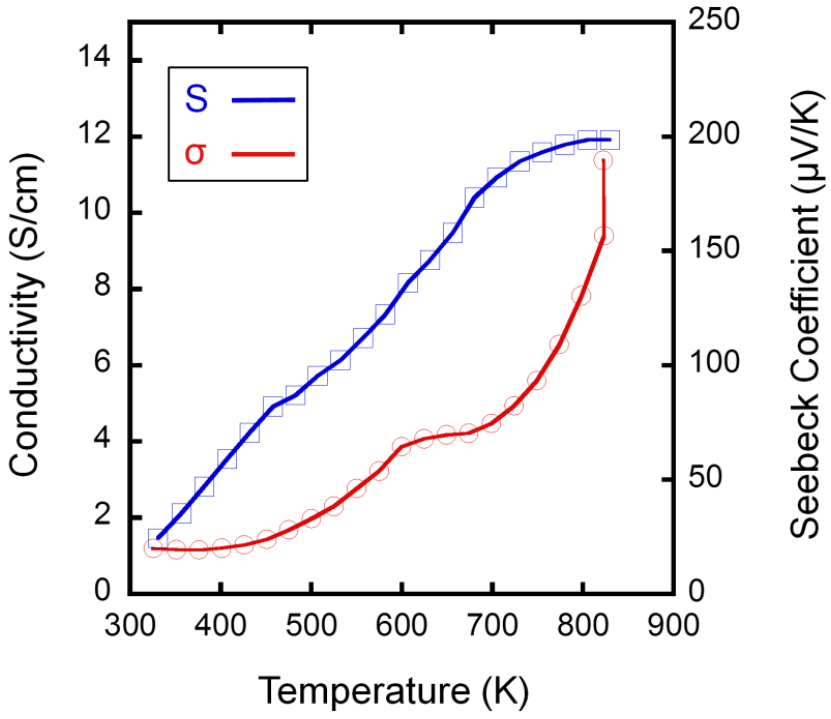

Figure 4-6: Temperature dependence of the thermopower (S) and electrical conductivity (σ) of CTSe. The positive values of the thermopower indicate holes as the majority carriers and the gradual increase of the electrical conductivity with rising temperature is consistent with the intrinsic semiconducting behavior of the compound.

450 K and thereafter slowly increase with rising temperature to 4S/cm at 600 K. Beyond this temperature, the electrical conductivity drastically increase with further increase in temperature reaching 11 S/cm at 800 K.

4.3 Theoretical Calculations for Cu_4TiSe_4

4.3.1 Phonon Dispersion

A collaboration with Mingfei Zhang through Prof. Liang Qi's group in the Materials Science & Engineering Department at The University of Michigan provided the calculations to determine

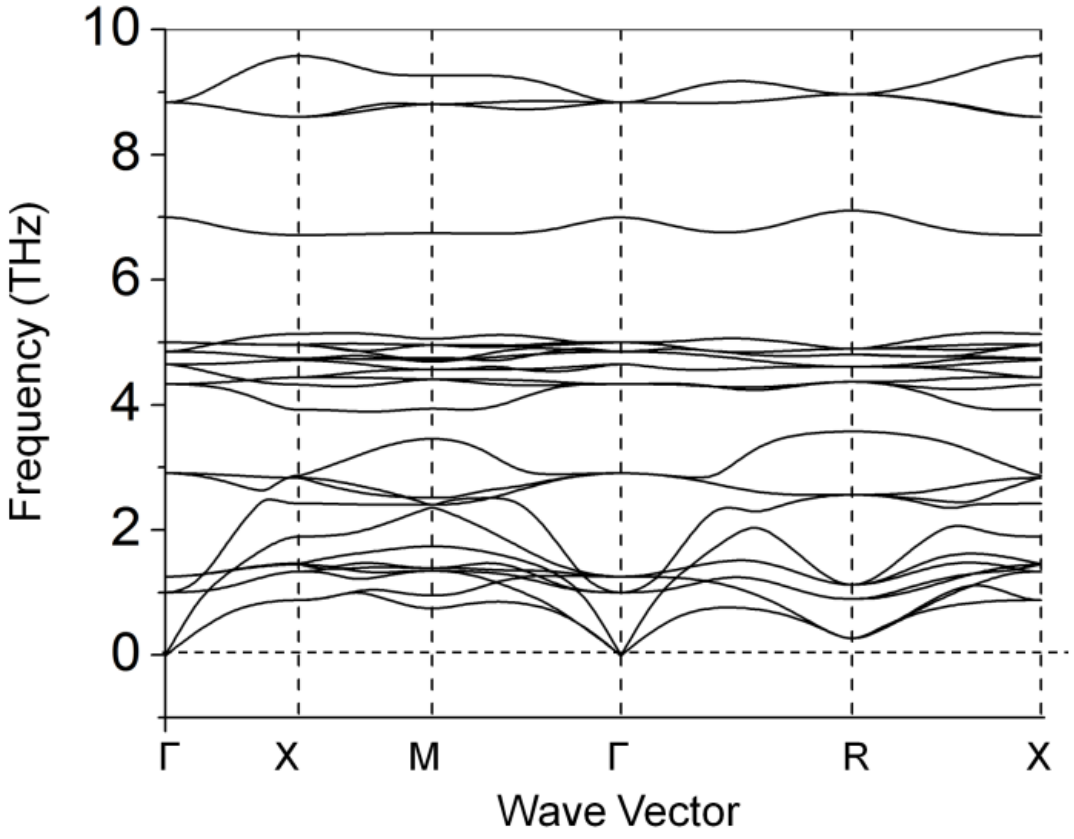

Figure 4-7: Calculated phonon dispersion relation of CTSe. No negative phonon frequencies are observed throughout the Brillouin Zone, indicating the dynamic stability of CTse upon small inhomogeneous deformation.

the phonon dispersion and the mechanical elastic constants of Cu_4TiSe_4. Density functional theory (DFT) calculations were performed with the Vienna ab initio simulation package (VASP)[136,137] within the projector augmented wave (PAW) formalism[138,139]. For the exchange-correlation functional we employed the generalized gradient approximation (GGA) as parameterized by Perdew, Burke, and Ernzerhof (PBE)[140]. For the sampling of the Brillouin zone we employed the Monkhorst-Pack scheme with a grid of 15 × 15 ×15 for CTSe supercell.[141] The cut-off energy for the plane wave basis was 400 eV, and the convergence criterion for the

electron-density self-consistency cycles was 10−6 eV. Three independent elastic constants c_{11}, c_{12} and c_{44} of CTSe cubic crystal structure were calculated based the derivatives of the total energy as functions of the specially designed strain.[142] The phonon dispersion relation of CTSe (Figure 4-7) was determined along high symmetry k-points path in the Brillouin zone using the Phonopy package[143] based on the force constants obtained from VASP calculations. The phonon frequencies are positive throughout the Brillouin zone, validating the dynamic stability of the material, thus it should be stable under any small inhomogeneous deformation inside its crystal structure.

4.3.2 Electronic Band Structure

For the electronic band structure and calculation of electronic and optical properties, a collaboration with Logan Williams from Prof. Kioupakis Group was formed. Density functional and many-body perturbation theory calculations for the band structure and optical properties were performed using the Vienna *Ab initio* Simulation Package (VASP).[144-147] The GW series of Projector Augmented Wave (PAW) pseudopotentials was used.[139,148] 11, 12, and 6 valence electrons were included for Cu, Ti, and Se respectively. Forces on all atoms were relaxed to under 0.005 eV/Å. The plane wave basis set cutoff was set at 700 eV. The electronic convergence criterion was set at 10^{-8} eV. Multiple levels of theory were used. The hybrid functional of Heyd, Scuseria, and Ernzerhof (HSE06)[149,150] was used to relax the crystal structure and to obtain the starting point for subsequent many-body perturbation theory calculations. Quasi-particle (QP) corrections based on the GW method (G_0W_0)[151] along with the maximally localized Wannier function method as implemented in the wannier90 code[152] were used to determine the quasiparticle band structure throughout the Brillouin zone. The dielectric

functions and the optical absorption coefficient were obtained with the Bethe-Salpeter equation (BSE) method.[153,154] Gamma-centered grids of 4x4x4 kpoints were used for all calculations. Convergence parameters of 1440 bands, a 300 eV GW basis set energy cutoff, and a value of 200 for NOMEGA were used in G_0W_0 calculations. BSE calculations included 32 occupied and 28 unoccupied bands.

4.3.3 Photovoltaic Conversion Efficiency

The upper limit of the estimated photovoltaic conversion efficiency (EPCE) as a function of thickness of the absorber layer was calculated according to a modified version of the Shockley–Queisser limit as shown in Figure 4-12.[155] The impedance matching factor, or fill factor, and the ratio of open circuit voltage to band gap voltage were left constant at the values expected for full absorption of light into the materials, as tabulated by Rühle[156]. The spectrum losses were modified to account for the fraction of light that would be absorbed for a given thickness, using material absorption coefficients that were interpolated throughout the energy range specified in the AM1.5G solar spectrum[157]. Due to incomplete data for CdTe[12], the absorption coefficient from 4.145 eV to 4.429 eV was assumed to remain constant at the 4.145 eV value; this region of the solar spectrum has a negligible effect on the final result due to the small phonon flux in this region and the relatively high absorption coefficients in this region compared to the 1-3 eV range. For these calculations, the band gap and absorption coefficient data are used as inputs into the modified version of the Shockley-Queisser limit.

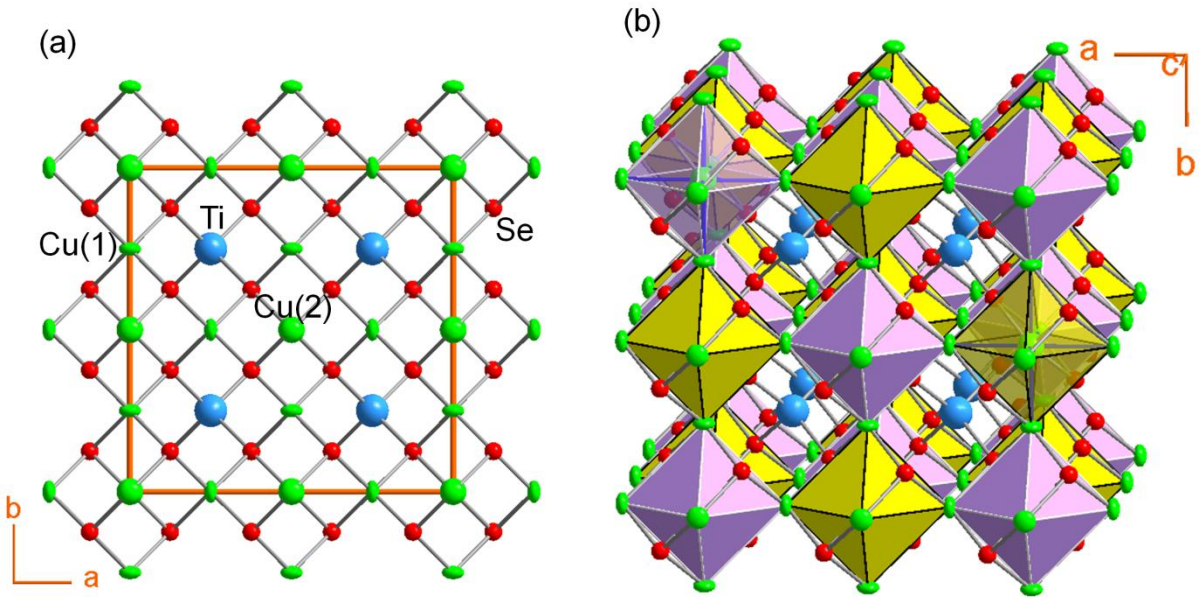

Figure 4-8 [001] view of Cu_4TiSe_4 b) Building blocks $[Cu_4Se_4]^{4-}$ anionic cluster and Ti^{4+} cation. $[Cu_4Se_4]^{4-}$ clusters formed two interpenetrated face centered cubic (fcc) lattices (purple clusters formed fcc as well as yellow clusters). The Ti^{4+} ions are located

4.4 Results and Discussion

CTSe crystallizes in the noncentrosymmetric cubic space group F-43*c* (No. 229) at ambient conditions with lattice parameter *a* = 11.2936 (2) Å and adopts a new structure type that can be regarded as a 2a×2a×2a superstructure of sulvanite (Cu_3VS_4)[158] (Figure 4-8a,b,). Chemically, CTSe is an analog of CZTS where $2Cu^+$ and Ti^{4+} replace the six positive charges from Zn^{2+} and Sn^{4+} cations. Similarly to the zincblende-type structure of CIS, CIGS and CZTSSe, which features a characteristic 3D network of tetrahedrally coordinated metal atoms, MSe_4, (M = Cu, Sn, In, Zn or Ga), Cu and Ti metal atoms in CTSe are also tetrahedrally coordinated by selenium. However, while metal tetrahedra in zincblende-type compounds share only corners to form the 3D network, $CuSe_4$ tetrahedra ($Cu(1)Se_4$ and $Cu(2)Se_4$) in CTSe share both edges and corners in all directions to build a 3D framework of $[Cu_4Se_4]^{4-}$ anionic clusters (Figure 4-8b). Within the $[Cu_4Se_4]^{4-}$ clusters, $Cu(2)Se_4$ tetrahedra share all edges with $Cu(1)Se_4$ tetrahedra, while $Cu(1)Se_4$

tetrahedra exclusively share corners with each other (Figure 4-1 a,b,c). The resulting spatial arrangement of $Cu(1)Se_4$ and $Cu(2)Se_4$ tetrahedra is topologically equivalent to the sulvanite structure (with $Cu(2)Se_4$ corresponding to VS_4 and $Cu(1)Se_4$ corresponding to CuS_4). Using the $[Cu_4Se_4]^{4-}$ clusters as building units, the 3D structure of CTSe can simply be described as two interpenetrated face centered cubic (*fcc*) lattices in which Ti^{4+} atoms are located at tetrahedral interstices within the channels (Figure 4-8b). This structural representation of CTSe, based on the Cu-centered $[Cu_6]$ octahedral cluster, $Cu@[Cu]_6$, is also topologically similar to a double-perovskite structure. The $TiSe_4$ tetrahedra in the structure of CTSe are isolated from each other and share only corners with $Cu(1)Se_4$ and $Cu(2)Se_4$ tetrahedra (Figure 4-1d). The unique composition and structural features of CTSe, compared to zincblende-type solar absorbers, give rise to promising electronic and optical properties that were theoretically and experimentally investigated in this work.

Band-structure calculations with hybrid density functional and many-body perturbation theory reveal that CTSe is an indirect-gap semiconductor with a 1.22 eV gap from M to Γ

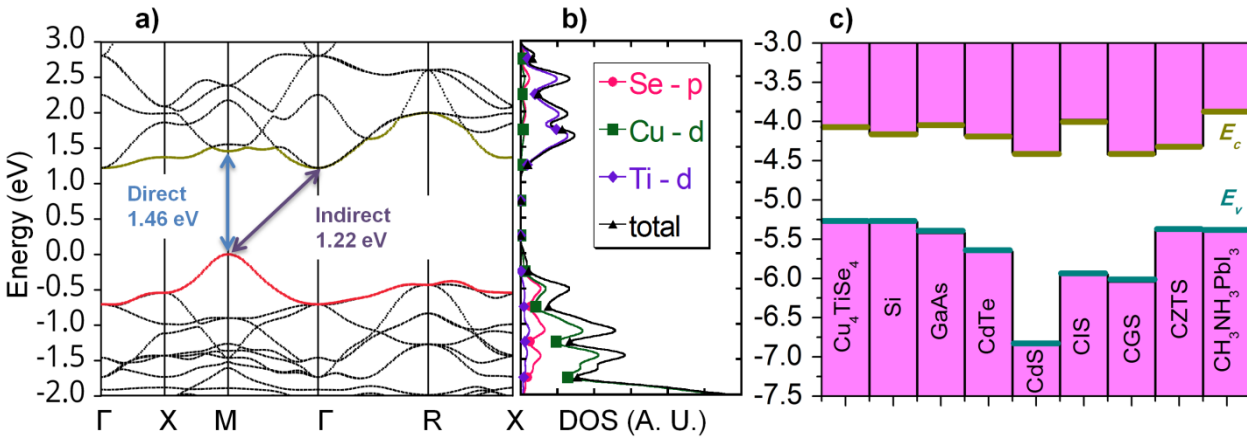

Figure 4-9 a) Calculated band structure and b) DOS of Cu_4TiSe_4. c) Band alignment of Cu4TiSe4 relative to other materials for PV.

(Figure 4-9a). However, the minimum direct gap (at M), which determines the onset of optical absorption, is only slightly larger at 1.46 eV and close to the Shockley-Queisser optimal value.[155] What makes CTSe particularly promising for solar cells, however, is the large density of states (DOS) near the band edges (Figure 4-9b), which gives rise to optical absorption coefficients larger than 10^5 cm^{-1} throughout the visible range (Figure 4-10). The large DOS derives from the flat valence (which consists of Cu 3*d* and Se 4*p* orbitals) and conduction (composed of Ti 3*d* states) bands. As a result of this unique band structure, CTSe is a promising absorber material for thin-film solar cells compared to GaAs, CIGS, and CZTS (which feature broad *s*-type conduction bands with a lower density of states), and CTSe thin-film solar cells reach comparable efficiencies at a much lower thickness. The calculated absorption coefficient of CTSe is compared to experiment and other absorber materials in Figure 4-10. CTSe is predicted to outperform all established absorber materials in the 1.1-2.8 eV range that contains most of the terrestrial solar spectral irradiance.

To probe the theoretically predicted interesting optical properties of Cu_4TiSe_4, polycrystalline powders were prepared through solid-state reaction of the elements at moderate temperatures. The agreement, in both peak positions and intensity distributions, between the experimental X-ray powder diffraction pattern and the theoretical pattern generated using single crystal structure data confirms the single-phase nature of the as-synthesized polycrystalline powder. (Figure 4-2a) In addition, the true density of the synthesized material measured using helium gas pycnometry was found to be 5.77(6) g cm^{-3}. This value is slightly larger than the theoretical density of 5.69(8) g cm^{-3} calculated from the crystal structure data.

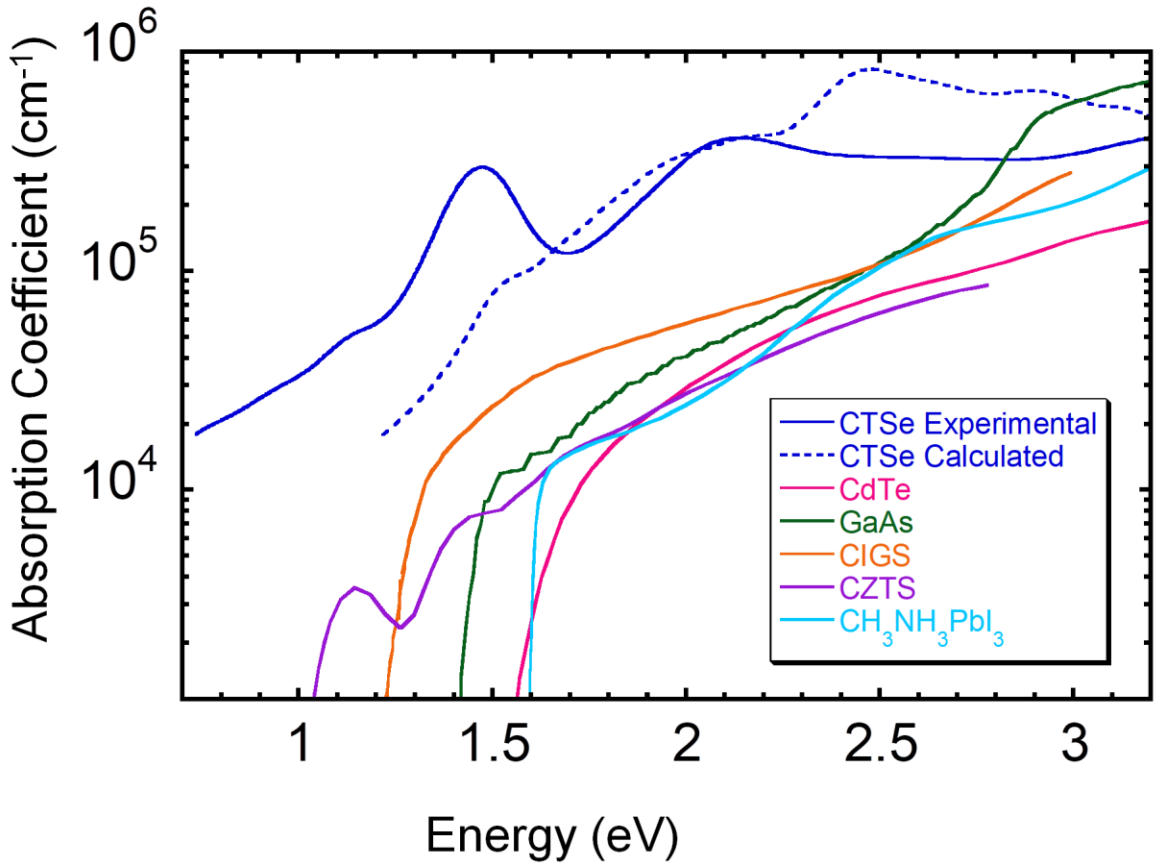

Figure 4-10: Theoretical and experimental absorption coefficients of CTSe compared to leading solar absorber materials such as CdTe[12], GaAs[17], CIGS[14], CZTS[159], and $CH_3NH_3PbI_3$[20]. CTSe outperforms all established solar-absorber materials in the 1.1-2.8 eV range.

This small deviation of 1.4% is within the instrument precision of ± 5% further confirming the high purity of the synthesized material. Further confirmation of the single-phase nature of the synthesized Cu_4TiSe_4, polycrystalline powders was obtained from differential scanning calorimetry (DSC) measurement. DSC curves recorded for two successive heating and cooling cycles show a single endothermic peak of melting at 850 ºC on heating and a single exothermic peak of crystallization at 850 ºC on cooling indicating a congruent melting and crystallization of the compound (Figure 4-2b). No sign of phase transition and decomposition of the sample were detected on the DSC curves suggesting a good thermal stability of the compound.

To further investigate the structural stability of CTSe, we applied density functional theory (DFT) calculations to determine (1) the formation energy, (2) the three independent cubic elastic constants (c_{11}, c_{12} and c_{44}), and (3) the phonon dispersion relation of CTSe. The formation energy of CTSe, based on the chemical reaction $2CuSe_2 + 2Cu + Ti \rightarrow Cu_4TiSe_4$, is -3.03 eV per formula unit, which indicates a strongly exothermic reaction and suggests that CTSe is thermodynamically stable relative to $CuSe_2$, Cu, and Ti. Moreover, the calculated elastic constants for CTSe are C_{11} = 90.75 GPa; C_{12} = 67 GPa; and C_{44} = 21.33 GPa, which satisfy the Born elastic stability criteria for a cubic structure at zero external pressure[160] [(C_{11}-C_{12}) > 0, C_{44} > 0, and (C_{11} + 2C_{12}) > 0]. In addition, the phonon dispersion relation of CTSe (Figure 4-7) displays no imaginary frequencies, indicating the stability of CTSe with respect to spontaneous structural transformations by dynamic lattice vibrations.[161] Therefore, the thermodynamic, elastic and dynamic stability of CTSe, coupled with the congruent melting and crystallization observed from DSC curves, implies a relatively facile fabrication of crystalline CTSe thin films using various deposition methods, starting from high density targets of the synthesized polycrystalline powders.

Therefore, thin-films of CTSe on 300 nm SiO_x/Si substrates were fabricated by pulsed laser deposition (PLD) in order to investigate their optical properties as well as the potential of CTSe as a solar material. The structure and chemical composition of the films post deposition were confirmed by X-ray diffraction and scanning electron microscopy - energy dispersive X-ray spectroscopy (SEM-EDS) (Figure 4-11 and Figure 4-3). Careful comparison of the X-ray diffraction patterns of CTSe thin films, with that of bare substrate and the calculated theoretical pattern of CTSe revealed that the X-ray diffraction pattern of the resultant thin film matches the substrate's pattern and includes the 3 major peaks ((222), (044) and (226)) from the CTSe phase.

However, the CTSe peaks exhibit large differences in the relative intensity. The intensity of the (222) peak is larger (at least three times) than that of (044), which suggests that the film is polycrystalline with a strong orientation towards (222). SEM images reveal that the deposited CTSe films consist of finely aggregated polycrystalline particles (35~60 nm) with larger and thinner flakes that most likely result from "splashback" during the deposition process. The stoichiometry of the deposited film was confirmed by EDS analysis and is consistent with the composition of the target. The composition mapping of the films also reveals a uniform distribution of the elements (Figure 4-11).

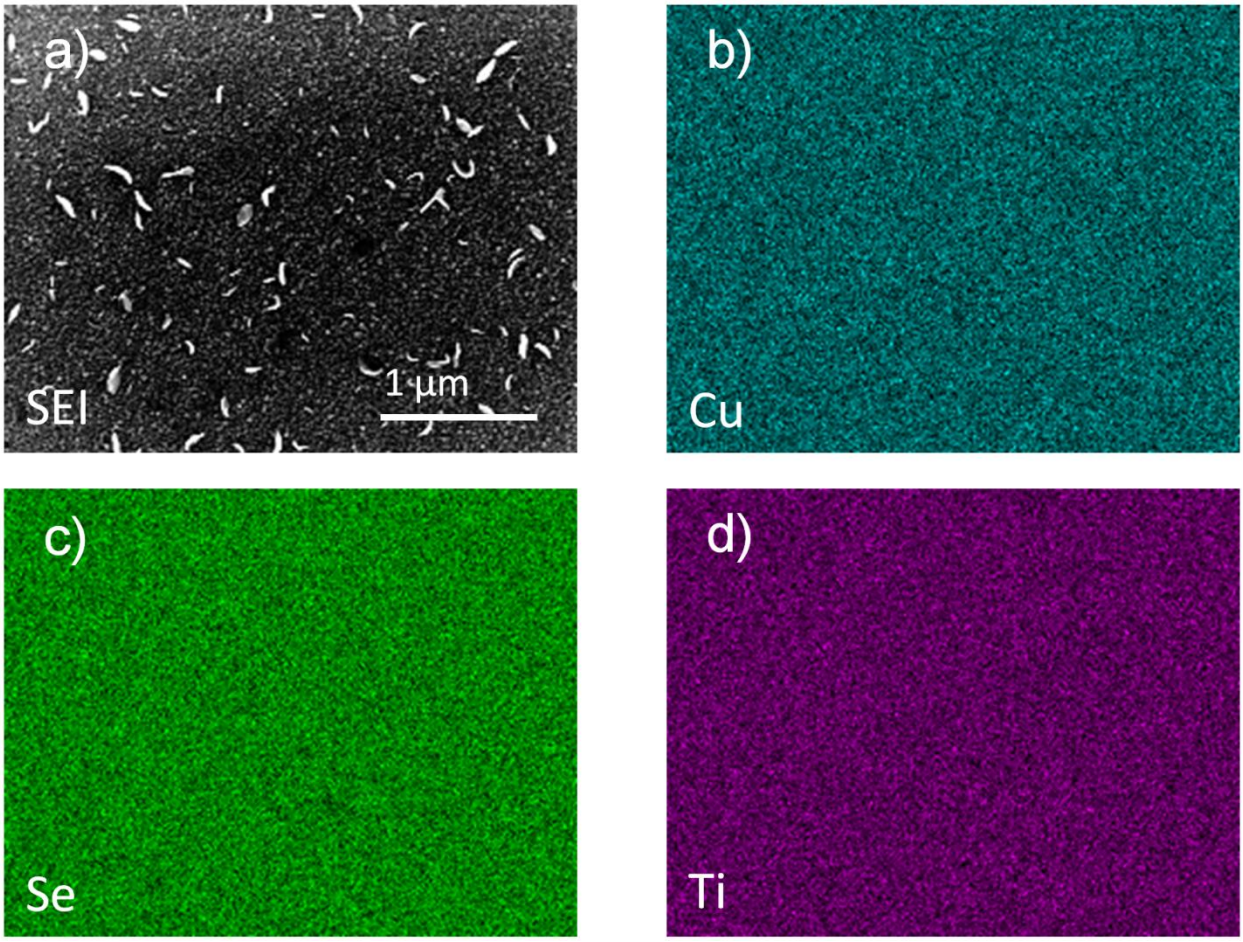

Figure 4-11: SEM image and composition mapping of CTSe thin film. a) Secondary electron image of the area. Qualitative EDS maps showing the distribution of b) Cu, c) Se and d) Ti.

The optical properties of the deposited films were characterized by the reflection-type interference-enhanced spectroscopic ellipsometry from 200 nm to 1680 nm. The measured refractive index (n) and extinction coefficient (k) of CTSe (Figure 4-5) show a broadband absorption in the visible and near-infrared (near-IR) range and two strong absorption peaks around 650 nm and 900 nm, respectively. The peak at the band gap is due to excitonic effect, which can be seen in GaAs-based systems[162-164] and the broad absorption prior to the band gap is due to defects in the film and a common characteristic of thin film based on similar transition metal chalcogenide materials.[165] The absorption coefficient of CTSe calculated using the extinction coefficient from ellipsometry data is plotted in Figure 4-10 and compared to our theoretical predictions and other materials. Both the predicted and the measured absorption coefficient of CTSe are larger than 10^5 cm^{-1} and greater than the absorption coefficients of most traditional solar absorbers such as CdTe, GaAs, CIGS, CZTS, and Si within the range 1.1 eV to 2.8 eV, where most of the light in the terrestrial solar spectrum resides. Careful analysis of the absorption curves using Tauc fitting enables the determination of experimental indirect band gap of 1.15 eV and direct band gap of 1.34 eV (Figure 4-5ab).

These values are comparable to the theoretically predicted indirect (1.22 eV) and direct (1.46 eV) band gaps of CTSe, and are well within the Shockley–Queisser range of optimal band gaps (1.1-1.5 eV). In addition, the indirect gap of CTSe favors long minority-carrier lifetimes and precludes the re-emission of the absorbed photons and the need for photon recycling, in contrast to direct-gap solar absorbers such as GaAs. Moreover, the small energy difference (~0.2 eV) between the direct and indirect gaps results in only a small additional energy loss due to carrier thermalization. These data offer the possibility of creating CTSe based solar cells of equal or superior efficiency to CdTe or GaAs cells at a fraction of the thickness.

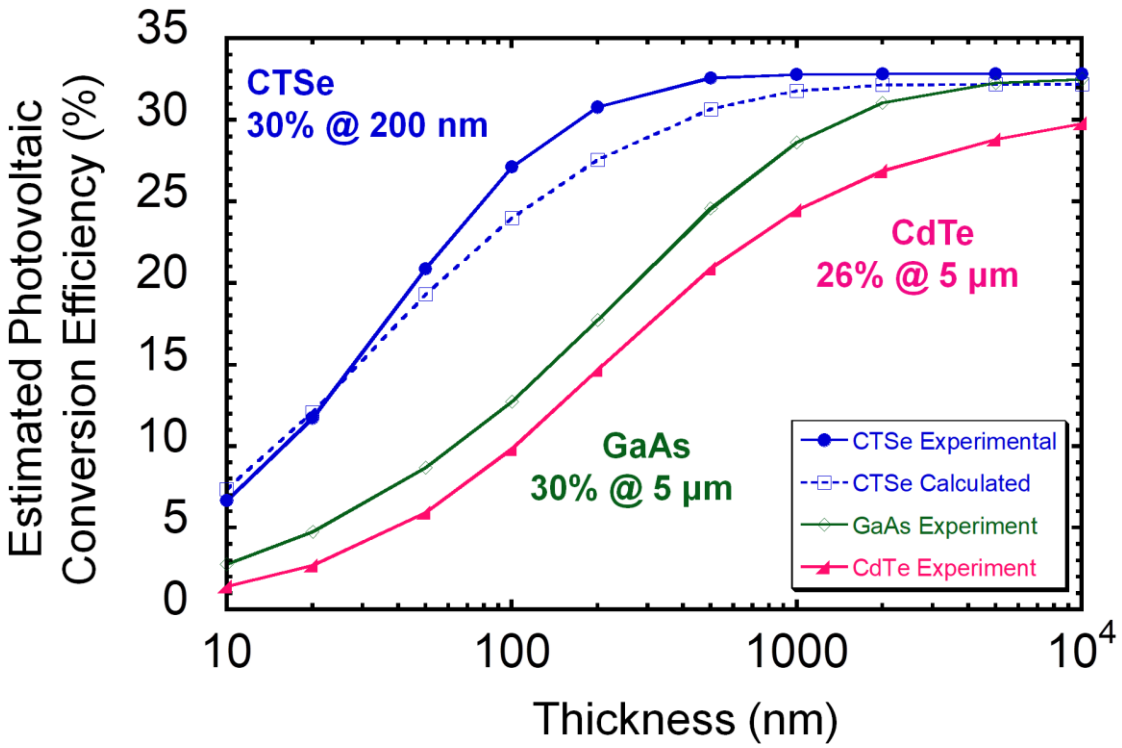

Figure 4-12: Estimated photovoltaic conversion efficiency (EPCE) as a function of thickness for CTSe compared to CdTe[12] and GaAs[17]. CTSe reaches an efficiency of 30% for a thickness of 200 nm, approximately one order of magnitude thinner than typical CdTe or GaAs devices (1.5 - 5 µm).

To quantify the advantages of CTSe for thin-film solar cells, we determined the upper limit of the estimated photovoltaic conversion efficiency (EPCE) as a function of absorber thickness and compared to that of GaAs, CdTe. The EPCE upper limit was calculated by evaluating the fraction of incident light absorbed for each wavelength in the AM1.5G solar spectrum, as determined by the absorption coefficient (Figure 4-10), and by including the spectral losses in the Shockley–Queisser limit [155-157].The fill factor and the ratio of the open-circuit voltage to the band gap voltage were left at their full absorbance values for this analysis. As shown in Figure 4-12, the estimated maximum efficiency of CTSe obtained using both the predicted and the measured absorption coefficients is significantly larger than that of GaAs and CdTe at low film

thickness. This result is supported by the ultra-large absorption coefficient of CTSe throughout the 1.1 eV – 2.8 eV range, which enables higher efficiencies at approximately one order of magnitude lower film thickness compared to CdTe and GaAs. For instance, a maximum EPCE of 30% is anticipated for a 0.2 μm CTSe thin film compared to 5 μm GaAs film for similar EPCE value. This analysis suggests the potential for the production of high-efficiency and flexible CTSe-based solar cell devices at low cost, paving the way to sustainable large-scale deployment of lightweight, high-efficiency solar cells based on absorber materials from cheap and environmentally friendly elements. Temperature dependent electronic transport measurement revealed that CTSe is a *p*-type semiconductor (Figure 4-6). The thermopower increases with temperature from 30 μV/K at 300 K to 200 μV/K at 800 K whereas the electrical conductivity increases from 1 S/cm at 300 K to 11 S/cm at 800 K. The analysis of the band alignment of CTSe relative to other leading p-type solar absorber materials such as Si, GaAs, CdTe, CdS, CIS, CGS, CZTS and $CH_3NH_3PbI_3$ is shown is Figure 4-9c. The conduction band minimum (CBM) of CTSe is located 4.06 eV below the vacuum level and the valence band maximum (VBM) is located 5.28 eV below the vacuum level. This places the band edges very close to those of GaAs (-4.00 eV and -5.39 eV), CdTe (-4.18 eV and -5.66 eV) and $CH_3NH_3PbI_3$ (-3.88 eV and -5.39 eV), a halide perovskite that is currently the focus of intense research efforts for solar cell applications.[122] The similarity of the band-edge positions to established solar absorbers indicate that CTSe may be compatible with commercial solar-cell architectures and manufacturing technologies, which should accelerate the development of optimal CTSe-based devices.

4.5 Conclusion

In summary, we discovered a new Earth-abundant ternary copper titanium selenide, CTSe, and assessed its potential as a promising solar absorber for low-cost, scalable, high-efficiency, single junction solar cells. CTSe adopts a new cubic structure type in which $CuSe_4$ tetrahedra share both corners and edges to form a 3D framework topologically similar to double perovskite with isolated $TiSe_4$ tetrahedra located within the channels. The unique structural feature of CTSe results in optimal theoretical/experimental band gaps of 1.22 eV/ 1.15 eV (indirect) and 1.46 eV/ 1.34 eV (direct), in the optimal range according to the Shockley-Queisser analysis. The Ti 3*d* orbital character of the conduction band results in ultra-large absorption coefficient ($\sim 10^5$ cm^{-1}) throughout the visible, outperforming most traditional absorbers such as CZTS, CIGS, GaAs and CdTe in the 1.1–2.8 eV range. A CTSe material thickness of only 200 nm is needed to outperform GaAs and CdTe solar cells that are typically a few microns thick. In addition, CTSe was found to be stable from energetic, elastic and dynamic aspects, which significantly enhances the prospect of realizing scalable, low-cost, high-efficiency, lightweight, and environmentally friendly next generation solar cells.

Chapter 5 $Cu_4TiSe_{4-x}S_x$: Band Gap Engineering for Cu_4TiSe_4 Photoabsorber Layer in Photovoltaic Solar Cell Device

5.1 Introduction

From the previous chapter, it was experimentally determined that the indirect and direct band gaps of Cu_4TiSe_4 are 1.15 eV and 1.33 eV respectively. These band gaps fall under the range of energy levels of sunlight which are most abundant on earth. To be able to harness higher energies, the band gap would need to be altered and a relatively straightforward method for accomplishing that is to use chemical substitution. For increasing band gaps in a metal-chalcogenide systems, the chalcogen is replaced with one that is one row above in the same group on the periodic table. For instance, tellurium can be replaced with selenium and/or sulfur and selenium can be replaced with sulfur. Conversely, sulfur can be replaced with selenium or tellurium to decrease the band gap. In this work, the chemical substitution in Cu_4TiSe_4 uses sulfur to replace selenium. The substitution of selenium with sulfur should result in larger band gaps in Cu_4TiSe_4. However, there will be a limit to how much sulfur can replace selenium without completely altering the structure because the structure of Cu_4TiS_4 is tetragonal.[166] Once the structure is completely altered, then the properties will strongly deviate from the originally intended properties.

5.2 Experimental

5.2.1 Synthesis

Elemental powders of copper (99.5%, Alfa Aesar), titanium (99.5%, Alfa Aesar), selenium (99.5%, Sigma Aldrich), and Sulfur (99.5%, Alfa Aesar) were weighed out in a stoichiometric ratio according to the series formula $Cu_4TiSe_{4-x}S_x$ (x = 0.05, 0.1, 0.5, 1.0, 1.5, and 2). Mixtures of each composition are sealed into quartz ampoules under 10^{-3} torr residual pressure. The ampoules are then gently heated in the furnace from room temperature to 300 °C over 12 hours, and then remain isothermal for 24 hours. This is a low temperature step to allow the chalcogenide elements to pre-react with the other elements in the mixture and prevent deposition in other areas of the ampoule. After the first isothermal period, the temperature is increased to 550 °C over 6 hours, where the temperature will remain isothermal for 96 hours. After the second isothermal step, the furnace is brought down to room temperature over 24 hours. The ampoules are broken open in an argon-filled glovebox and the resultant samples are ground into a powder. Samples are stored in the glovebox until further characterization or processing.

5.2.2 PXRD

Powdered X-ray diffraction patterns of the $Cu_4TiSe_{4-x}S_x$ (x = 0.05, 0.1, 0.5, 1.0, 1.5, and 2) series was recorded using a Rigaku Miniflex 600 with graphite monochromator operating Cu-Ka (λ = 1.54056 Å) at 40 kV and 15 mA in Bragg-Brentano geometry. The scan condition was from 10° to 70° 2θ at 2°/second. The resultant patterns were compared to the powder pattern for Cu_4TiSe_4 and Cu_4TiS_4 generated from single crystal data.

5.2.3 DSC

25-30 mg of each member of the $Cu_4TiSe_{4-x}S_x$ (x = 0.05, 0.1, 0.5, 1.0, 1.5, and 2) series was placed in 2 mm x 3 mm quartz tubes and sealed under 10^{-3} Torr residual pressure. The samples

were then loaded into a Netzsch Pegasus 404 F1 Differential Scanning Calorimeter with a blank quartz tube of approximately the same mass as the total mass of the sample and its respective quartz tube. Thermal events were recorded between room temperature and 1000 K with heating rate of 20 K/min under flowing (20 L/min) nitrogen gas.

5.2.4 Band Gap Determination from Diffuse Reflectance Spectroscopy

$Cu_4TiSe_{4-x}S_x$ (x = 0.05, 0.1, 0.5, 1.0, 1.5, and 2) series were collected on a Varian Cary 5000 UV-vis-NIR spectrometer equipped with a Harrick Praying Mantis diffuse reflectance accessory.

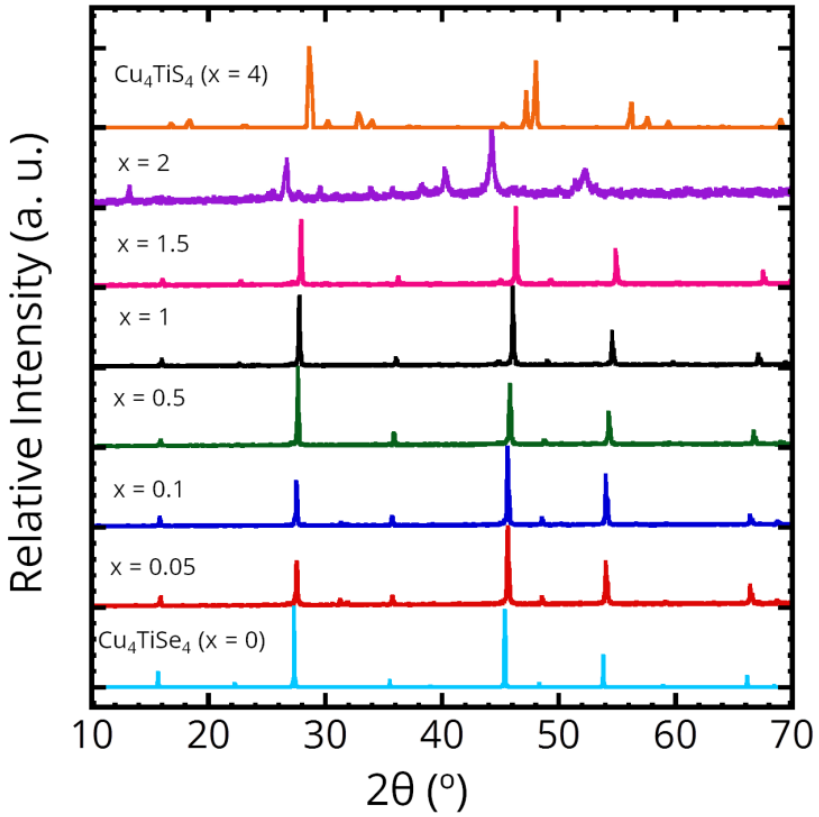

Figure 5-1: Powdered X-ray diffraction patterns comparing the members of the $Cu_4TiSe_{4-x}S_x$ series with the end member compounds, Cu_4TiSe_4 and Cu_4TiS_4.

These measurements were performed through a collaboration with Dr. Stanislav Stoyko under the direction of Professor Jennifer Aitken at Duquesne University. $BaSO_4$ was the 100%

reflectance standard. Scans were made from 2500 nm to 200 nm at a rate of 600 nm per minute. The percent reflectance was converted to absorption using the Kubelka-Munk relationship and wavelength was converted to energy. Using the equations for Tauc analysis[135], the data was transformed for determining indirect and direct band gaps and then linear regions were selected for linear regression (see Chapter 2 for details). With the equation for the linear regression computed, the x-intercept, band gap, of this equation was easily obtained.

5.3 Results and Discussion

5.3.1 Phase and Thermal Signatures

The powdered X-ray diffraction patterns comparing the members of the $Cu_4TiSe_{4-x}S_x$ (x = 0.05, 0.1, 0.5, 1.0, 1.5 and 2.0) series with the end member compounds, Cu_4TiSe_4 and Cu_4TiS_4 are shown in Figure 5-1. From the most minor substitution amount to x = 1.5, the pattern resembles the selenium parent compound. The x = 1.5 value translates to 11% at (at % is computed for the entire nominal composition at the substitution value) of Se substitution with S. At x = 2 (16% at of Se substitution with S), the structure changes from the higher symmetry cubic structure to a lower symmetry. It is not presently identifiable with known patterns in the PDF 4+ database. It is not similar to the tetragonal Cu_4TiS_4 pattern either.

However, as compared with the Cu_4TiSe_4 base pattern, the large peaks at 28, 46 and 54 degrees 2 theta are present but shifted to the left. The shifting to the lower angle indicates a much larger unit cell in comparison with Cu_4TiSe_4. With respect to the rest of the series, the major peaks shift slightly more to the right with each increase in selenium substitution with sulfur. This observation is resonable considering that sulfur has a smaller atomic radius than selenium.

In light of the thermal signatures from DSC as shown in Figure 5-2, the melting temperature becomes progressively lower with additional sulfur replacing selenium. The melting temperature decrease is initially from 850 °C for Cu_4TiSe_4 to 820 °C, then progressively lower towards 800 °C with increasing substitution of sulfur with selenium. The lowest melting onset is from x = 1.5, being exhibited at 760 °C. In the thermal signatures of x = 0.05 and x = 0.1, they exhibit an additional two pairs of peaks (375/350 °C during heating cycle and 550/530 °C during cooling cycle) which may correspond to phase impurity. It is unlikely that these pairs of peaks at 375/350 °C and 550/530 °C have to do with structural transitions because the rest of the members of the series do not exhibit such peaks; the remaining members of the series are transition-free up until their melting point. The amount of impurity is also not detected in the powdered X-ray diffraction patterns, which indicates that these impurities in the x = 0.05 and x = 0.1 powders do not have large enough crystallite aggregates to diffract X-rays, but are able to be detected through DSC measurement.

Another interesting feature of the series up until x = 1.5 is that the melting peaks (760 °C – 840 °C) are very sharp in comparison with crystallization which means that the material will melt congruently.

However, upon crystallization (cooling curve at 700 °C – 800 °C), there is an abrupt release of energy which is spread over a much wider temperature range as compared to the melting peak. The parent Cu_4TiSe_4 structure has many atoms that are moving around through all the vacant

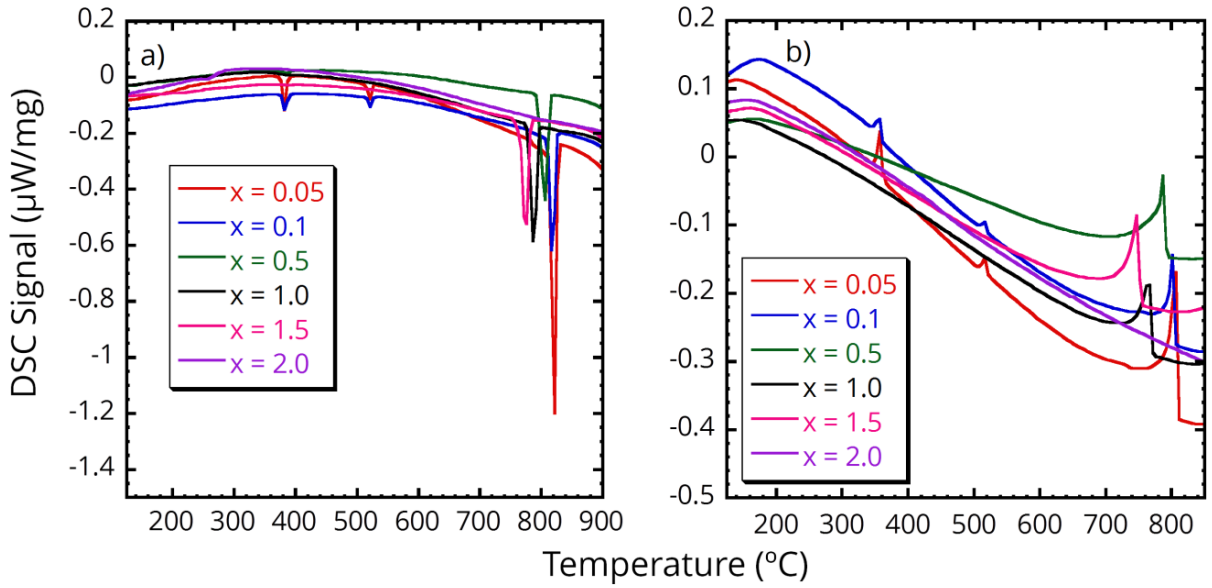

Figure 5-2: Thermal signatures from DSC of the $Cu_4TiSe_{4-x}S_x$ series. a) heating and b) cooling.

sites (25% of the sites are vacant) before finding their lowest energy state.

Because x = 2 is very different than the parent structures, it is not unusual to differ from the other thermal signatures of the other series members. x = 2 does not exhibit a melting, crystallization or any phase transition in the measured temperature range. Because the melting point was not observed in this temperature range, it is possible that the melting and crystallization temperatures are much higher than is possible to measure safely (in consideration of the instrument's longevity). It is possible that the melting temperature of x = 2 exceeds 1200 °C.

The absorbance spectra of all the synthesized members are shown in Figure 5-3. All of the series members up to x = 1.5 show gradually increasing low absorption up until the onset at the band gap, where there is a sharp increase in the absorption as a function of energy. In the case of x = 2, due to its very different structure, its optical absorption is much different than the rest of the series. The absorption starts at very low energies with an increase in less than 100 meV until around 1.3 eV, where the absorption start to level off and then decrease at 1.4 eV. This behavior

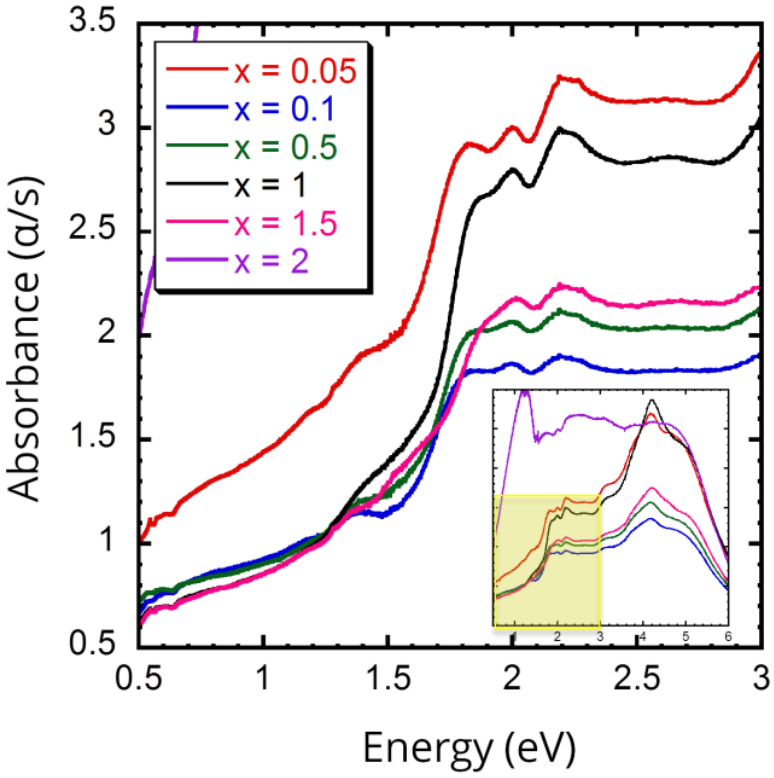

Figure 5-3: Absorbance spectra as a function of energy taken through diffuse-reflectance UV-VIS-IR spectroscopy. The inset of the figure is a zoomed out version is to illustrate the unlikeness of the x = 2 absorbance spectrum.

is similar to a semimetal. Utilizing the Tauc analysis method to determine the band gap, a summary of indirect and direct band gaps have been tabulated in Table 5-1.

With respect to the small increase in sulfur as indicated by the x = 0.05, the direct band gap increases 0.16 eV, but the indirect band gap decreases by about 0.2 eV. The increase is expected due to the change in band structure which sulfur contributes. However, the decrease in indirect band gap may also be due to the very small amount of phase impurity detected by DSC. In general, the direct band gap monotonically increases with increasing sulfur fraction. However, there is nonlinear bowing of the band gap with increase in sulfur content up until x = 1.5. At x = 1.5, there is a slight decrease from x = 0.1, but still larger than the original 1.34 eV band gap of the parent compound Cu_4TiSe_4.There is no detectable trend of the indirect band gap, which may be due to small impurities or how sulfur affect the band structure. The band structure (E-k diagram, see Figure 4-9 in Chapter 4) of the parent compound is flat as compared to other direct gap semiconductors and silicon, so alterations to the parent Cu_4TiSe_4 compound may be much more profound.

Table 5-1: Tabulation of direct and indirect band gaps for the compositions in the $Cu_4TiSe_{4-x}S_x$ (x = 0.05, 0.1, 0.5, 1.0, 1.5, and 2) series as compared to the Cu_4TiSe_4 end member.

Composition	Direct Allowed (r=1/2)	Indirect Allowed (r=2)
Cu_4TiSe_4	1.34 eV	1.11 eV
$Cu_4TiSe_{3.95}S_{0.05}$	1.50 eV	0.895 eV
$Cu_4TiSe_{3.9}S_{0.1}$	1.53 eV	0.977 eV
$Cu_4TiSe_{3.5}S_{0.5}$	1.56 eV	1.03 eV
Cu_4TiSe_3S	1.64 eV	1.23 eV
$Cu_4TiSe_{2.5}S_{1.5}$	1.61 eV	0.984 eV
$Cu_4TiSe_2S_2$	~ 0.07 eV	~ 0.79 eV

5.4 Conclusion

Through solid state synthesis, we created a series of $Cu_4TiSe_{4-x}S_x$ (x = 0.05, 0.1, 0.5, 1.0, 1.5) compound with identical structure to its parent compound, Cu_4TiSe_4. There is a small shift (~0.5 degrees 2theta) of the phase peaks to higher angles in PXRD, which indicates that the lattice parameter becomes smaller. The lattice parameter difference is minor, but must be accounted for if lattice matching upon a specific substrate is required. With the small addition of sulfur (x = 0.05 to x = 1.0), it is demonstrated that the band gap is alterable from 1.34 eV to 1.64 eV. However, the consequences of the addition of sulfur (in fractions x = 0.05 to 1.5) will also reduce the melting temperature of the compound from 850 ºC in Cu_4TiSe_4 to 760 ºC in $Cu_4TiSe_{2.5}S_{1.5}$.

Chapter 6 Tuning the Optical, Electronic, and Thermal Properties of $Cu_3NbS_{4-x}Se_x$ Through Chemical Substitution

6.1 Introduction

New sustainable materials made from earth-abundant elements with tunable band gap within the energy range from 1 eV to 3 eV are of great interest for various optoelectronic applications. Along this line, copper chalcogenides with the sulvanite structure (Cu_3VS_4) are of great interest in the scientific community. Owing to their compositional flexibility, these systems enable band gap engineering within a wide range (from 0.93 eV for Cu_3VTe_4 to 2.6 eV for Cu_3TaS_4)[53,167,168] This paves the way to applications in photovoltaic devices[169], solar water splitting cells[170] and transparent conducting materials (TCMs) for use in organic light emitting diodes, solar cells and flat panel displays.[171] Despite this potential use of sulvanite compounds, there has not been significant attention paid to the synthesis and elucidation of their crystal structures and functional properties.[172] Among known sulvanite compounds, V_3CuS_4 has garnered substantial attention as host materials for lithium intercalation[173] and as an absorbing

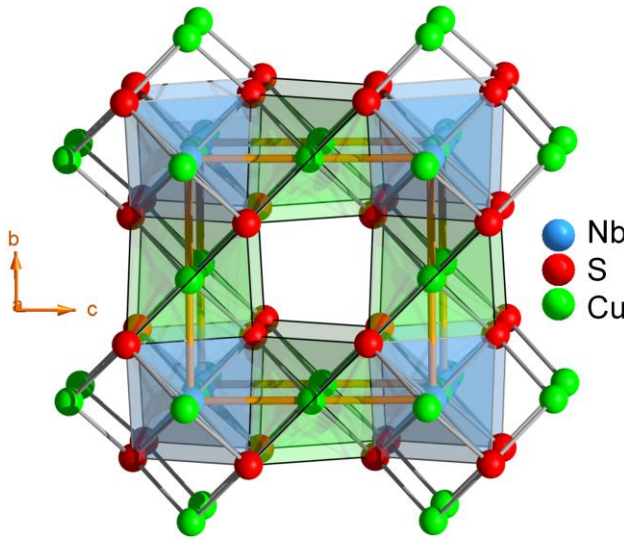

Figure 6-1 Crystal structure of Cu_3NbSe_4 and Cu_3NbS_4.

layer photovoltaics[174] applications. However, its isostructural homologues can be obtained through chemical substitution of (1) V by Nb, or Ta and (2) S by Se or Te, have received far less attention in comparison.[53,54,168,172] Recently, research utilizing first-principle calculations have predicted some of their optical and electronic properties.[53,54,168,172] Interesting, these phase were thought to be p-type materials, which for optoelectronics and thermoelectrics, are lacking in comparison with respect to the development and availability of n-type materials. These works provided insight into the potential of Cu_3NbSe_4 and Cu_3NbS_4 (among other compounds) for photovoltaic and p-type optically transparent semiconductor applications. Crystals of Cu_3NbSe_4 have been reported to have a red-orange color while Cu_3NbS_4 has been described as having either orange or greenish color.[55] Furthermore, it was predicted that the direct gaps and indirect gaps are 2.31eV and 1.82 eV for Cu_3NbS_4 and 1.95 eV and 1.64 eV for Cu_3NbSe_4.[53,54,168,172] These band gaps are not suitable for p-type transparent semiconductor applications, but there is potential a solid-solution series with these two compounds through partial substitution of S by Se in the structure of $Cu_3NbS_{4-x}S_x$. Such substitution could enable tuning the band gap from 2.31 eV for Cu_3NbS_4 to 1.95 eV for Cu_3NbSe_4. Thus, this strategy would enable materials covering upper-green to upper-yellow range of band gaps for optoelectronic devices. In addition, such S to Se substitution will enable tuning the lattice parameter to match that of the GaAs substrate, which should facilitate epitaxial growth of single crystal thin film of $Cu_3NbS_{4-x}Se_x$ on GaAs substrate for various optoelectronic devices.

Cu_3NbSe_4[175] and Cu_3NbS_4[176] crystallize in the primitive cubic space group P-43m (#215) with lattice parameters of 5.638(1) Å and 5.501(2) Å respectively. The crystal structure contains two tetrahedrally coordinated metal atoms, $NbSe_4$ and $CuSe_4$. The Cu atom is located at 3d position whereas the Nb atom occupied the 1a position. In the three-dimensional structure, six

crystallographically equivalent $CuSe_4$ tetrahedra share corners to form an octahedral cluster around the $NbSe_4$ tetrahedron, which in turn share edge with each of the six $CuSe_4$ tetrahedra. The resulting [Nb@$Cu_{6/2}$]Se4 cluster Figure 6-1 can be regarded as the building block for the formation of the primitive cubic lattice. Interestingly, the lattice parameter of Cu_3NbSe_4 (a = 5.638 Å) is practically identical to that of GaAs (a = 5.653 Å), whereas the lattice parameters of Cu_3NbS_4 (a = 5.50 Å)[176] is similar to that of Si (a = 5.431 Å). There is a 0.265% lattice mismatch between the structures of Cu_3NbSe4 and GaAs, which satisfies the precondition for low residual strain (or even strain-free) epitaxial growth of Cu_3NbSe_4 films on GaAs substrate. One could reasonably expect a dislocation at approximately every 380 planes. The lattice mismatch between Cu_3NbS_4 and Si is slightly larger, 1.3%, but is also within a suitable range for epitaxial growth of strained Cu_3NbS_4 thin films on Si substrate.

Through examination of the $Cu_3NbS_{4-x}Se_x$ series in light of Rume-Hothery rules for substitutional solid solutions, we expect that the formed compounds will be part of a solid solution.[177,178] The first rule states that the difference in atomic radius of the solute and solvent atoms must be less than or equal to 15%. Given that atomic radii of selenium and sulfur are 115 pm and 100 pm[179] respectively, this first rule is satisfied. The second rule states that the crystal structures of the solute and solvent must be similar. This second rule is also satisfied when considering that Cu_3NbS_4[180] has similar crystal structure with Cu_3NbSe_4.[175] They both have the same space group P-43m (#215) and similar lattice parameters 5.5001 Å (Cu_3NbS_4) and 5.6381 Å (Cu_3NbSe_4). [175,180] The third and fourth rules state that both solute and solvent need to have the same valency and similar electronegativity. With respect to those rules, sulfur and selenium have the same valency in their respective ternary phases and the electronegativies are reported to be 2.58 (sulfur) and 2.55 (selenium) on the Pualing scale.[181] Thus, the satisfaction of the Rume-

Hothery rules for the ternary phases predict that the $Cu_3NbS_{4-x}Se_x$ series should be a solid solution series.

To date, there has not been significant insight into the measurement of the electronic, optical and thermal properties of these compounds.[53,55,158,167,168,174-176] These measurements are necessary to probe their thermoelectric performance as well as confirming their predicted p-type semiconducting behavior. Here, we report of the optical, electronic and thermal properties of the $Cu_3NbS_{4-x}Se_x$ series (x = 0, 0.1, 0.2, 0.4, 0.6, 0.8, and 4). We show that these materials feature holes as the majority carrier for electronic conduction through careful measurement of the Seebeck coefficient. The effects of sulfur substitution by selenium on the refined lattice parameters; thermal stability; optical band gaps; thermal conductivity; and electronic transport properties are discussed.

6.2 Experimental

6.2.1 Synthesis

Elemental powders of niobium (99.5%, Alfa Aesar), copper (99.5%, Alfa Aesar), and selenium (99.5%, Sigma Aldrich) and/or sulfur (99.5%, Alfa Aesar) were weighed the appropriate stoichiometric ratios for the x values (x = 0, 0.1, 0.2, 0.4, 0.6 and 0.8) and then manually ground with agate mortar and pestle until homogeneously mixed. These mixtures were then flame-sealed in evacuated (~10^{-4} Torr) quartz tubes and placed in a tube furnace. The temperature profile is programmed for ramping to 573 K over 10 hours and held steady for 24 hours to allow the selenium and sulfur to react with the rest of the elements. Next, the furnace temperature was increased to 823 K in 4 hours, held for 120 hours and finally cooled to room

temperature over 24 hours. The sintered powder products were again manually ground with an agate mortar and pestle. After grinding, the polycrystalline powders of Cu_3NbS_4 sample and all intermediate compositions (varying x-values) exhibited a very fine consistency with a light olive green color whereas the Cu_3NbSe_4 powder yields a reddish-orange color. All handling was conducted in an argon-filled glovebox and the synthesized materials were stored within the glovebox prior to structural characterization and material processing in order to avoid the possibility any oxidation which may affect the resultant properties.

6.2.2 PXRD and DSC

X-ray diffraction patterns of the as-synthesized powders were recorded on a Rigaku Miniflex 600 with graphite monochromator operating Cu-Ka (λ = 1.54056 Å) at 40 kV and 15 mA in Bragg-Brentano geometry. The scan condition was from 10° to 70° 2θ at 2°per second. The resulting powder patterns were compared with patterns in the PDF-4+ database as well as theoretical powder pattern simulated using single crystal data[176,175] from the Inorganic Crystal Structure Database (ICSD). Structural data from the reference files were used for the Rietveld refinement of the lattice parameters of the synthesized compounds using the FULLPROF software package.[182]

Approximately 30 mg of $Cu_3NbS_{4-x}Se_x$ powder was sealed in a small quartz DSC tube under a residual pressure of ~10^{-3} Torr and loaded into a Netzsch Pegasus 404 F1 Differential Scanning Calorimeter with a blank quartz tube of approximately the same mass. The DSC data were recorded on heating and cooling between room temperature and 1273 K with heating rate of 20 K/min under flowing (20 L/min) nitrogen gas. The measurement was repeated on the same sample to check for thermal stability.

6.3.3 Band Gap determination

Optical diffuse reflectance spectra of the $Cu_3NbS_{4-x}Se_x$ (x = 0, 0.1, 0.2, 0.4, 0.6, 0.8, and 4) x series were collected on a Varian Cary 5000 UV-vis-NIR spectrometer equipped with a Harrick Praying Mantis diffuse reflectance accessory. BaSO4 was the 100% reflectance standard. Scans were made from 200 nm to 2500 at a rate of 600 nm per min. The percent reflectance was converted to absorption using the Kubelka-Munk relationship and wavelength was converted to energy.

6.3.4 Thermoelectric Measurement

The as-synthesized powders were densified into 10 mm diameter and 2.5-3mm thick pellets using a 20 ton uniaxial hot press. The pressing conditions were 100 MPa and 723 K (for samples with $x \leq 0.8$) or 923 K (for the Cu_3NbSe_4 sample) for 4 hours. Cu_3NbSe_4 failed to fully densify with the lower annealing temperature of 723 K. After densification, the pellets were ground and polished to mirror finished surface on both sides. A thin layer of graphite was sprayed on both sides of the pellets and then loaded into the laser flash apparatus Linseis LFA 1000. Thermal diffusivity data was collected from room temperature to 623 K under dynamic vacuum. The thermal conductivity was calculated from the thermal diffusivity data using the relationship $\kappa = DC_pd$, where D is the measured thermal diffusivity, C_p is the heat capacity and d is the geometrical density of the pellet. A Pyroceram 9606 reference material was measured alongside each sample. The instrument precision for the thermal diffusivity data is +/- 3%. The heat capacity used for the thermal conductivity calculations were extracted from the laser flash data.

To decouple the electronic contribution to the thermal conductivity, the Wiedemann-Franz law was used to calculate the electronic contribution to the thermal conductivity. The electronic contribution was subtracted from the total thermal conductivity (measured through the laser flash method) to determine the lattice thermal conductivity.

Hot pressed pellets for each composition were cut using a wire saw with SiC slurry to produce bar specimen of about 9 mm x 2mm x 2.5 mm.

The bars were used for simultaneous measurement of the thermopwer and electrical conductivity using an ULVAC-RIKO ZEM-3 system.The electrical resistivity and Seebeck coefficient data were recorded from room temperature to 598 K with ΔT increments of 5 K, 10 K and 15 K. The measured data were used for the calculation of the power factor ($S^2\sigma$), where S is the thermopwer, and σ is the electrical conductivity.

6.3 Results and Discussion

6.3.1 Phase and Thermal Signature

Figure 6-2 shows the powder X-ray diffraction patterns of $Cu_3NbS_{4-x}Se_x$ series. A comparison of the measured XRD patterns to the theoretical patterns of Cu_3NbS_4 and Cu_3NbSe_4 from single crystal data indicates that the intermediate compositions are isostructural to the two end members. No diffraction peak from impurity phases or unreacted elements could be observed on the XRD patterns suggesting complete substitution of S by Se in the crystal structure of Cu_3NbS_4.

All patterns were indexed to P -43m (#215) and the lattice parameters of the selected compositions of the series were refined using Rietveld methods (Table 6-1). The refined values of the lattice constant of Cu_3NbSe_4 and Cu_3NbS_4 were 5.655(6) Å and 5.5006(8) Å respectively

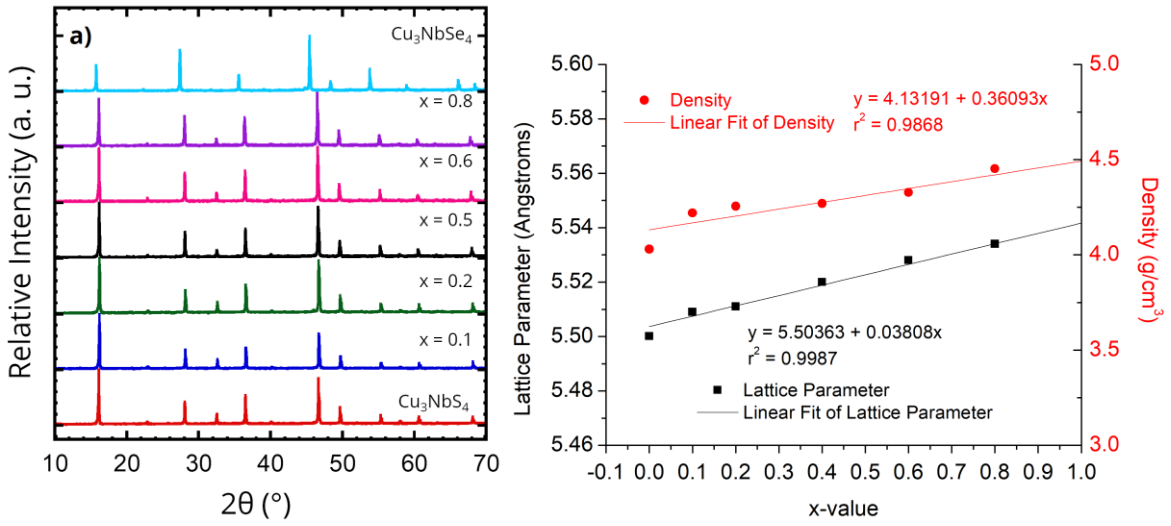

Figure 6-2: a) Powdered X-ray diffraction of the as-synthesized $Cu_3NbS_{4-x}Se_x$ (x = 0, 0.1, 0.2, 0.4, 0.6, 0.8 and 4) powders. Inset: full range which includes the x = 4 value.

and have agreement factors . These values are comparable (within 0.3%) to the reported lattice parameter for Cu_3NbSe_4[175] and Cu_3NbS_4[176] (Table 6-1). The lattice parameter of the intermediate composition increases with increasing x values (increasing Se content), which is consistent with the substitution of small sulfur atoms by the slightly larger selenium atom within the structure of Cu_3NbS_4. The plot of the lattice parameter and density as a function of Se content Figure 6-2b) exhibits an agreement with the linear relationship (Vegard's law and Roth-Humery rules) anticipated for a substitutional solid solution because the r^2 (goodness of fit) in both cases exceeds 0.95. However, it is also possible that the slight deviation from linear relationships (for both density and lattice parameter as a function of Se content) because of atomic site disorder

where the Se is not all going into the S site but instead in an interstitial position. This can be alleviated with longer annealing time at the elevated temperature (550 °C) than the allotted time described in this work (823 K for 240 hours instead of 120 hours, for example). Another factor which can contribute to the observed deviation is due to accuracy of the composition.

Table 6-1: Resultant fitting values, lattice parameters, densities and thermal conductivity for Cu_3NbS_4 and Cu_3NbSe_4.

Composition	R_f	$\chi 2$	a ref. (Å)	a refined (Å)	ρ_{calc} * (g/cm^3)	ρ_{meas} (g/cm^3)	$\kappa_{323\ K}$ (W/m-K)
Cu_3NbS_4	6.27	2.59	5.501	5.501	4.11	4.030	2.71
Cu_3NbSe_4	7.63	2.43	5.638(1)	5.655(6)	5.55	5.569	2.91
$Cu_3NbS_{3.9}Se_{0.1}$ (x = 0.1)	5.10	1.96		5.508561	4.14	4.220	3.91
$Cu_3NbS_{3.8}Se_{0.2}$ (x = 0.2)	7.18	3.50		5.511339	4.18	4.255	3.57
$Cu_3NbS_{3.6}Se_{0.4}$ (x = 0.4)	8.24	2.4		5.519742	4.25	4.270	2.61
$Cu_3NbS_{3.4}Se_{0.6}$ (x = 0.6)	9.86	1.53		5.527641	4.33	4.328	2.93
$Cu_3NbS_{3.2}Se_{0.8}$ (x = 0.8)	8.47	1.61		5.533970	4.40	4.453	2.86

*** for the solid solution members, the calculated density uses the refined lattice parameter.**

The measured densities for the $Cu_3NbS_{4-x}Se_x$ series are comparable, within the precision (±5%) of the pycnometer, to the calculated densities obtained using the refined lattice parameters. The reported density is an average over 20 measurements and the standard deviation on each density measurement (for the member in the series) through the gas pycnometer is 0.003 g/cm^3.

Figure 6-3a and b show the first heating and cooling differential scanning calorimetry (DSC) curves for the $Cu_3NbS_{4-x}Se_x$ series. All samples showed a single endothermic peak of melting upon heating from room temperature to 1300 K indicating the formation of nearly single-phase samples. The sulfur-rich compositions melt incongruently at ~1086K, and crystallize on cooling at 1059 K with a minor impurity phase. A much better thermal stability is observed for the selenium phase, which melts congruently at much higher temperature (1200 K) and crystallizes at without decomposition at 1150 K.

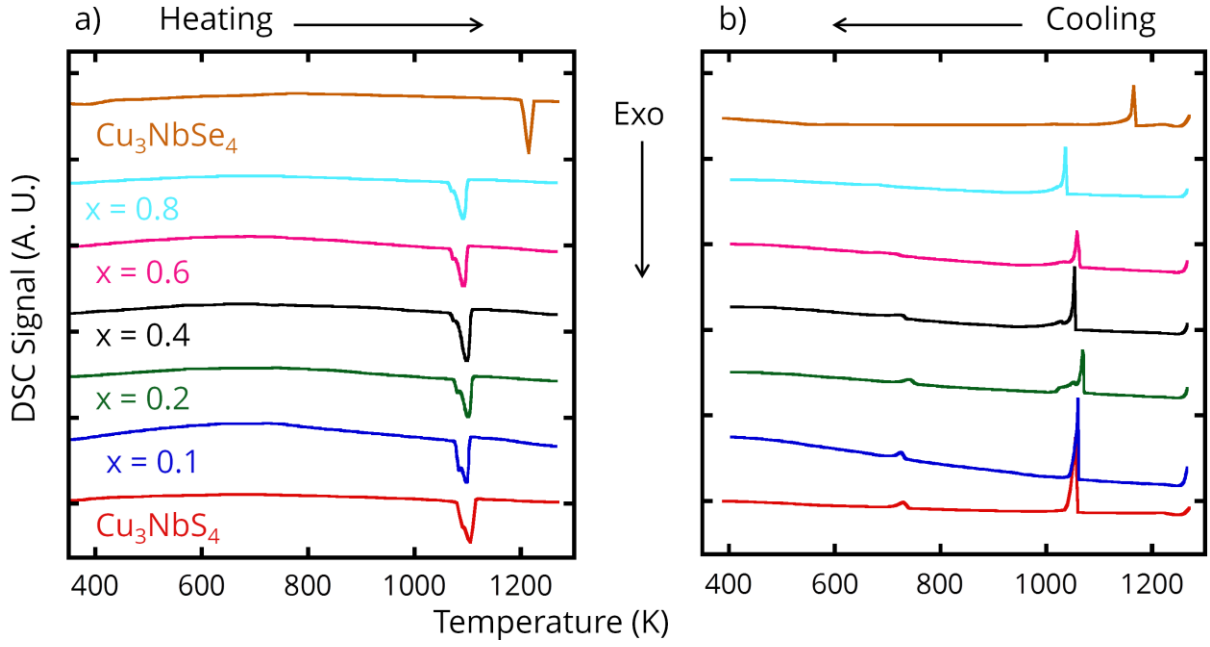

Figure 6-3: DSC curves from one heating and cooling cycle of the $Cu_3NbS_{4-x}Se_x$ series.

For Cu_3NbS_4, the first heating has no observable transitions until a large peak at 1081 K which is identified as melting as shown in Figure 6-3a. The crystallization onset is 1059 K. These two transition temperatures are consistent for both cycles. On the first cooling, there is a peak at 733 K which corresponds to the peak on the second heating and cooling. The ASM phase diagram reports that there are transition temperatures of 708 K and 780 K respectively for Cu_2S

and CuS which are close to the observed peak.[183] The reactions which take place at those temperatures are Cu + $Cu_{1.8}S$ Dig ht ➔ Cu_2S ht for 708 K and L + $Cu_{1.8}S$ dig ht ➔ CuS rt for 780 K.[183] This is not unreasonable considering that Cu_3NbS_4 melted and possibly formed pockets where the composition in that space fulfilled the composition range and temperature requirement

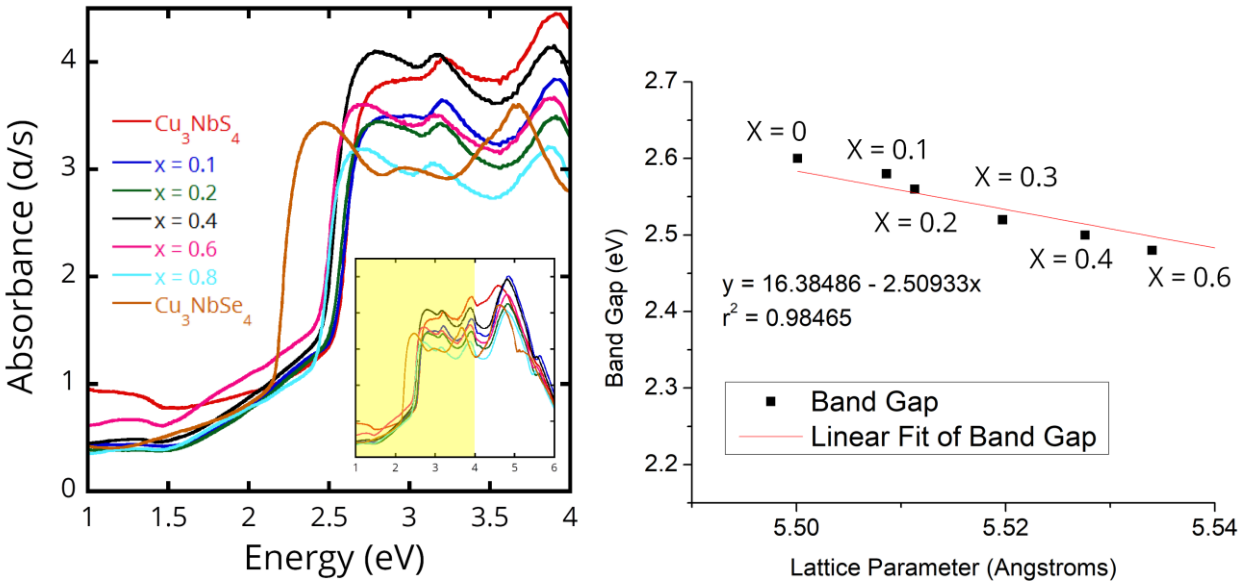

Figure 6-4: a) Absorbance as a function of energy for the $Cu_3NbS_{4-x}Se_x$ series. b) Band gaps plotted as a function of lattice parameter for each x-value in the $Cu_3NbS_{4-x}Se_x$ series.

for those reactions to take place. Given that the onset is about 723 K upon heating, it seems more likely that the involved transition is for Cu + $Cu_{1.8}S$ into Cu_2S.

For Cu_3NbSe_4, there are no observable transitions between room temperature and the melting temperature as shown in Figure 6-3a. The melting temperature is consistent at 1106 K in Figure 6-3a. Recrystallization peaks are observed at 1164 K and 1125 K in Figure 6-3b. The reduction in the recrystallization temperature may be due to atomic arrangement being more disordered due to the melting of the compound. The extra peak that appears may be a niobium selenide. If so, it can be concluded that the material decomposes slightly once heated past melting for all compositions.

The other members of the solid solution series resemble signatures similar to the Cu_3NbS_4 which is reasonable considering that less than 25% of the sulfur has been substituted with selenium. The onset of melting decreases slightly from 1081K to 1060K for x = 0.8. There also appears to be a phase transition shortly before melting because of the shoulder associated with the larger main peak or possibly incongruent melting. For practical purposes, it is not unreasonable to associate the shoulder's onset as the melting temperature since that is the temperature which the original structure is no longer stable.

6.3.2 Optical Band Gap

Table 6-2: Table of Compositions and their respective band gaps as measured through the energy for peak dA/dE(E) and Tauc fitting for direct allowed transition.

Composition	**Energy for Peak in dA/dE(E)**	**Direct Allowed (r=1/2)**
Cu_3NbS_4	2.6 eV	2.55 eV
$Cu_3NbS_{3.9}Se_{0.1}$	2.58 eV	2.53 eV
$Cu_3NbS_{3.8}Se_{0.2}$	2.56 eV	2.50 eV
$Cu_3NbS_{3.6}Se_{0.4}$	2.52 eV	2.46 eV
$Cu_3NbS_{3.4}Se_{0.6}$	2.50 eV	2.44 eV
$Cu_3NbS_{3.2}Se_{0.8}$	2.48 eV	2.43 eV
Cu_3NbSe_4	2.2 eV	2.17 eV

Figure 6-4**a** depicts the UV-Vis optical absorption spectra of the synthesized compositions in the $Cu_3NbS_{4-x}Se_x$ series. All samples show an increase in absorbance above energy range from 2.1 eV to 2.5 eV, which suggests that the band gaps for various compositions in this series lies somewhere between 2.1 eV and 2.5 eV. The peak from the first derivative of the absorbance versus energy and the band gap determination from Tauc analysis are compiled in Table 6-2. It can be observed from Table 6-2, that the energy where the peak in the derivative of absorbance

versus energy occurs matches well with the values from Tauc analysis for direct allowed transition. The agreement of the derivative for the peak energy and band gap determined from Tauc analysis suggests that the optical band gaps obtained from the optical measurement are direct gaps. It is interesting to note that the band gap of 2.6 eV for Cu_3NbS_4 corresponds well with a photon energy in the lower bound of blue and upper bound of green, whereas the band gap of 2.2 eV for Cu_3NbSe_4 is in the upper bound of yellow and lower bound of green. Therefore, the substitution between S and Se in the structure of both Cu_3NbS_4 and Cu_3NbSe_4 enables tuning the direct band gap of intermediate compositions between 2.2 eV and 2.6 eV, which covers the full range of green band gap. In comparison with theoretical works, the reported direct band gaps were 2.31 eV for Cu_3NbS_4 and 1.85 Cu_3NbSe_4, which are lower than what was measured in this work.[53] For known experimental work, Cu_3NbSe_4 has had its direct band gap measured through optical absorption method and was reported to be 2.45 eV for direct.[55] The main difference between this work and the reported value is due to the synthesis method: Grima-Gallardo *et al.* [55] utilized the melt-anneal technique which is prone to formation of second phases.

These investigations pave the way for further exploration of optoelectronic devices operating within this energy range. For example, selected compositions from this series can be used as p-type transparent conducting layer (electrode) in solar cell devices based one thin-film silicon, GaAs, chalcopyrite, organic, perovskite, etc. Additional potential use of such transparent electrodes includes organic and inorganic LEDs (OLEDs, LEDs), smart windows, and liquid-crystal displays (LCDs). One can also envision optoelectronic devices with optical emission in the blue and green regions.

It is interesting to note that large change in the optical band gap of $Cu_3NbS_{4-x}Se_x$ series with only a small various in the lattice parameter. For example, increasing the lattice parameter

by only 0.6% results in a 0.13 eV drop in the optical band gap (Figure 6-4b). This implies that one can envision engineering an optoelectronic device, which requires a series of band gaps, while maintaining an excellent lattice coherency at the interfaces between successive electrodes. The optical band gap of each of the electrodes within such device can be precisely tuned to produce the desired photon wavelength, by controlling the degree of Se to S substitution within the $Cu_3NbS_{4-x}Se_x$ series. Examples of successful implementation of this strategy can be found in literature such as aluminum gallium nitride (AlGaN) where the band gap can be tailored for $Al_xGa_{1-x}N$ from 3.4 eV (x = 0) to 6.2 eV (x = 1).[184]

6.3.3 Thermoelectric Potential

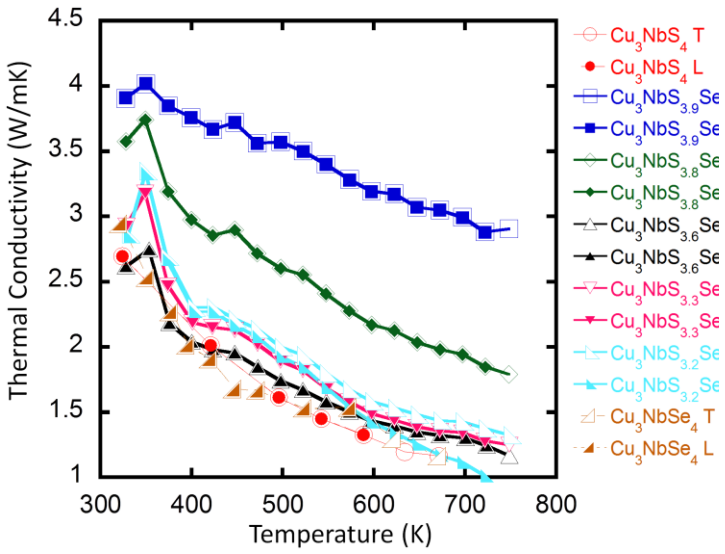

Figure 6-5: Thermal conductivity of Cu_3NbSe_4 (blue) and Cu_3NbS_4 (red).

Figure 6-5 shows the themal conductivity of the $Cu_3NbS_{4-x}Se_x$ series calculated from the thermal diffusivity data obtained from the laser flash method as described in Chapter 2. The thermal conductivity at 323 K for Cu_3NbS_4 and Cu_3NbSe_4 are 2.91 W $m^{-1}K^{-1}$ and 2.71 W $m^{-1}K^{-1}$ respectively. The thermal conductivity decreases drastically with increase in temperature. The observed decrease in the thermal conductivity is associated with an increase in phonon scattering due to an increase in lattice vibrations with temperature. The magnitude of the decrease diminishes after about 473 K.

At 673 K, the thermal conductivities are 1.16 W $m^{-1}K^{-1}$ for both compositions. The electronic contribution to the thermal conductivity (κ_{elec}) estimated from the electrical conductivity using Wiedemann-Franz law, $\kappa_{elec} = \sigma LT$, where $L = 2.44x10^{-8}$ W Ω K^{-2} is the Lorenz number, is negligible given the very low electrical conductivity of both Cu_3NbS_4 and Cu_3NbSe_4 phases (Figure 6-6). Therefore, the total thermal conductivity in these compounds are dominated by the lattice contribution (κ_{catt}). Interestingly, the thermal conductive of the intermediate compositions are comparable or higher than that of the two end members. For instance, the substitution of 2.5% sulfur by Se (x = 0.1) drastically increases the total thermal conductivity from 2.6 to 3.9 W $m^{-1}K^{-1}$ at 327 K. The observed behavior suggests that the introduction of this fraction of Se further stabilizes the Cu_3NbS_4 crystal lattice. Indeed, the x = 0.1 sample maintains the largest thermal conductivity at high temperatures. Further increasing the Se content to 5% (x = 0.2) result in a sharp drop in the thermal conductivity at high temperatures indicating effective mass fluctuation phonon scattering due to the intermixing of Sulfur and Selenium within the crystal lattice. The effect of mass fluctuation phonon scattering increases with the incorporation of 10% Se (x = 0.4) within the Cu_3NbS_4 crystal lattice. The lowest lattice thermal conductivity, ~ 1 W $m^{-1}K^{-1}$ at 775 K was observed for the composition with x = 0.8 and is attributed to a stronger contribution of mass fluctuation to phonon scattering in this sample.

Figure 6-6a-d show the temperature dependent electrical conductivity, Seebeck coefficient, power factor and ZT for selected compositions of the $Cu_3NbS_{4-x}Se_x$ series. The sample with x = 0 (Cu_3NbS_4) exhibits the lowest values of the electrical conductivity starting from 14 S/m at 306 K and slightly decreases to 3.4 S/m at 598 K. The selenium counterpart (x = 4) showed larger values of the electrical conductivity starting from 190 S/m at 306 K, which is over 10 times higher than the value observed for Cu_3NbS_4,and increases to 202 S/m at 323 K.

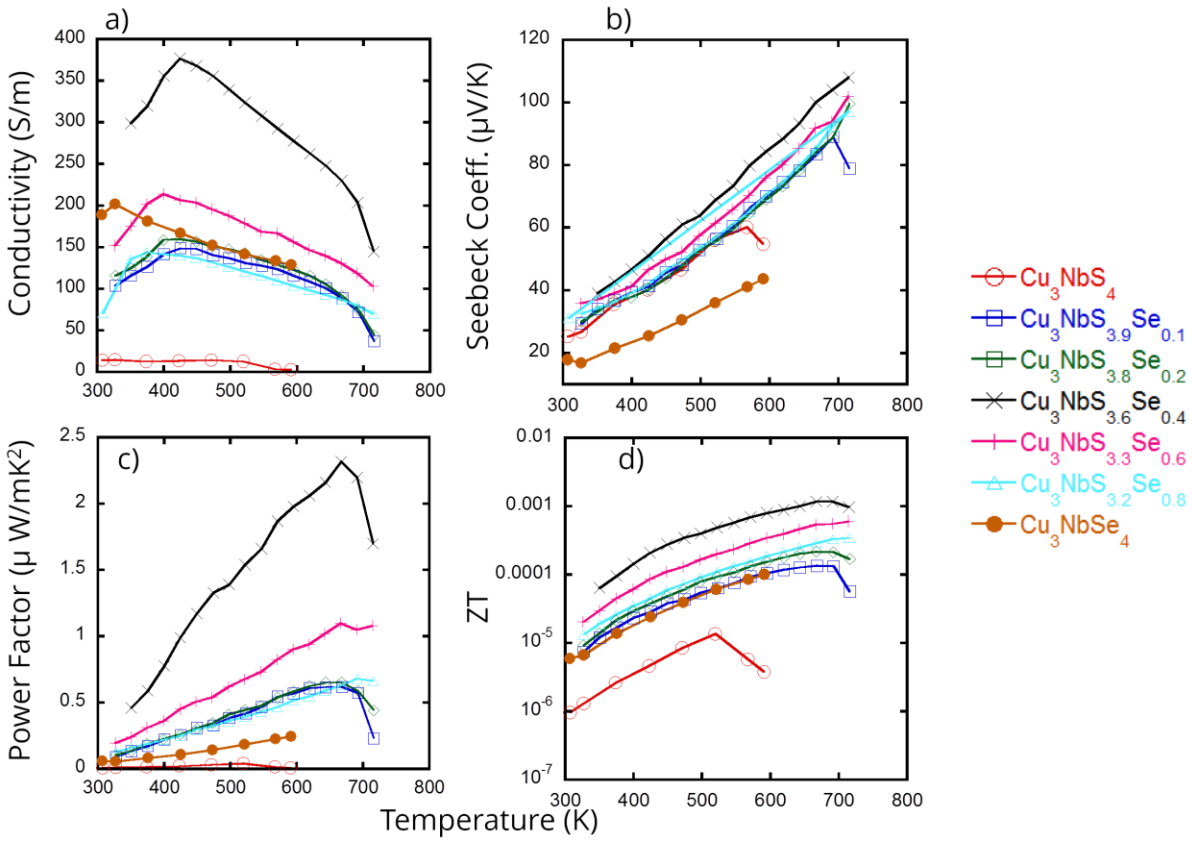

Figure 6-6: a) electrical conductivity, b) seebeck coefficient, c) power factor and d) ZT of Cu_3NbS_4-xSe_x.

Further increase in the temperature results to a graduate drop in the electrical conductivity down to 130 S/m at 598 K. The observed drop in the electrical conductivity is consistent with heavy doped semiconducting behavior[185], where the mobility of thermal excited carriers is severely diminished by electron – electron and acoustic phonon scattering. Regardless of the temperature, the electrical conductivity initially increases with increasing Se content, reaching the highest values for the composition with x = 0.4 (10%). Further increase in the selenium content resulted in a drop in the electrical conductivity (Figure 6-6a). The electrical conductivity of samples with x-values 0.1, 0.2, 0.4, and 0.8 initially increases with rising temperature, reaching the maximum

values at ~400 K. Further increase in temperature resulted in a drop in the electrical conductivity, which is consistent with heavily doped semiconducting behavior. The observed initial increase of the electrical conductivity below 400 K suggests thermal excitation of electron from the valence band to acceptor impurity states within the band gap leading to heavily doped semiconducting behavior at temperature above 400K. This analysis is consistent with the monotonic increase in the thermopower with increasing temperature for all composition of the $Cu_3NbS_{4-x}Se_x$ series (Figure 6-6b). All samples showed positive thermopower in the whole temperature range indicating p-type semiconducting behavior. The thermopower for Cu_3NbS_4 and Cu_3NbSe_4 are respectively, 26 μV/K and 17 μV/K at 309 K and increase with temperature to 60 μV/K and 40 μV/K at 600 K. Interestingly, the intermediate compositions showed larger thermopower values compared to the two end members. The largest thermopower values are observed for the composition with x = 0.4.At 309 K the thermopower for this composition is 40 μV/K and increase linearly with temperature to ~104 μV/K at 700 K.

The observed increase in both thermopower and electrical conductivity for the intermediate compositions resulted in large increase in the power factor when compared to the two end members Cu_3NbSe_4 and Cu_3NbS_4. The power factor for Cu_3NbS_4 increases slightly with temperature from 9.7×10^{-3} μW/mK^2 at 306 K to 4.1×10^{-2} μW/mK^2 at 523 K (Figure 6-6c). Slightly larger values of the power factor were observed for the selenium analog, Cu_3NbSe_4. At 309 K the power factor for this composition is 6×10^{-2} μW/mK^2 and increases almost linearly to 0.25 μW/mK^2 at 600 K. Partial substitution of sulfur by selenium in the $Cu_3NbS_{4-x}Se_x$ series increases the power factor in the whole temperature range, when compared to Cu_3NbS_4. The largest power factor is observed for the composition with x = 0.4, starting with a value of 0.5 μW/m K^2 at 309 K, which rapidly increases with rising temperature to a peak value of 2.2 μW/m

K^2 at 650 K. The observed increase in the electrical conductivity and thermopower of $Cu_3NbS_{4-x}Se_x$ samples upon substitution of S by Se, while maintaining the thermal conductivity close to that of the pristine Cu_3NbS_4 sample resulted in improved thermoelectric figure of merit ZT when compared to the two end members. The largest enhancement in ZT is obtained for the composition with x = 0.4, which displays a ZT value of 10^{-3} at 650 K.

6.4 Conclusion

We have investigated the effect of sulfur to selenium substitution on the structure, optical, electronic and thermal properties of the $Cu_3NbS_{4-x}Se_x$ series. Single-phase polycrystalline powders of selected compositions were synthesized through solid-state reaction of the elements at high temperature. X-ray diffraction on polycrystalline powders revealed that the synthesized materials are isostructural to the end member Cu_3NbS_4. A plot of the refined lattice parameter and measured density as a function of increasing selenium content (x values) show a linearity (r^2 > 0.98) suggesting that the $Cu_3NbS_{4-x}Se_x$ series is a substitutional solid-solution. This is also in agreement with the satisfaction of Cu_3NbS_4 and Cu_3NbSe_4 with the Rume-Hothery rules. Electronic transport data showed p-type heavily doped semiconducting behavior for all samples. Interestingly, the optical direct band gap of various $Cu_3NbS_{4-x}Se_x$ compositions can be tuned within the range from 2.6 eV for the sulfide end member and 2.2 eV for the selenide end member with marginal increase in the lattice parameter. These band gaps represent photon energies that cover the lower bound of blue all the way to the upper bound of yellow. In addition, the lattice parameters ranging from 5.655(6) Å Cu_3NbSe_4 for and 5.501(1) Å for Cu_3NbS_4, are comparable

to that of GaAs (a = 5.653 Å). These features could enable the design of fully tunable green band gap optoelectronic devices, which can be epitaxially grown on GaAs substrate.

Chapter 7 General Conclusion and Future Work

7.1 Summary and Closing Remarks

The general focus of this work was to further the discovery and understanding of material technologies for a future powered by renewable energy ecosystem. The energy from sunlight that falls upon the earth is so plentiful that with more efficient technology, it will be possible to harness a larger fraction of it. It is more predictable than wind and with energy storage technologies, it is possible to provide electric power at night. With respect to elucidating the behavior of as-synthesized lithiated copper sulfide phases from chapter 3, it is important to have enough metal atoms to maintain charge neutrality throughout the compound. This realization additionally sets parameters on materials chemistries involved which need to have atoms capable of changing oxidation states.

In the continuing effort to develop light absorbing materials to improve the efficiency of photovoltaic devices,Cu_4TiSe_4 (CTSe) has been discovered. Through the unique coordination of the metal atoms, the band structure shows very flat bands relative to other direct semiconductor materials. The combination of the flat bands, the large density of states from the atoms and the closeness of the indirect and direct band gaps allow CTSe to have an enormous absorption coefficient, with potential to surpass GaAs. Because spectral losses account for a majority of the efficiency loss, the large absorption coefficient allows CTSe to require 20x reduction in thickness over CdTe and GaAs.. In addition, CTSe was found to be stable from energetic, elastic

and dynamic aspects, which significantly enhances the prospect of realizing scalable, low-cost, high-efficiency, lightweight, and environmentally friendly next generation solar cells.

Further, the Cu_4TiSe_4 can have its band gap altered to be able to absorb even more portions of the solar spectrum. The band gap alteration comes in the form of substituting a small fraction of the selenium atoms, up to 11% at, to change the band gap from 1.34 eV to 1.64 eV. The advantage of this chemical substitution allows for flexibility in band gap, while exhibiting the same structure as the parent compound Cu_4TiSe_4. Because of the similarities with the parent compound, many processing parameters are applicable with the exception of temperatures in excess of half of the melting temperature.

Lastly, the $Cu_3NbS_{4-x}Se_x$ (x = 0, 0.1, 0.2, 0.4, 0.6, 0.8, and 4) solid solution series has very high melting temperatures (> 1073 K) and are straightforward to synthesize. The band gap is adjustable almost linearly with the substitution of sulfur atoms for selenium atoms from 2.60 eV to 2.48 eV. In addition, the lattice parameter of compositions near the sulfide phase have pattice parameters within 0.2% of GaAs, laying groundwork for epitaxial films upon GaAs substrates for optoelectronic device fabrication and research.

7.2 Future Work

7.2.1 Cu_4TiSe_4 and $Cu_4TiSe_{4-x}S_x$

With respect to Cu_4TiSe_4, it satisfies many property requirements which identify a good candidate for photovoltaic applications because of its band gaps in the 1.1 – 1.5 eV range, promising optical absorption and ability to be synthesized in bulk and thin film. Furthering this work would involve building, testing and optimizing a solar cell device using Cu_4TiSe_4. This

material also has the potential to be added as an absorber layer and rely upon higher mobility materials such as GaAs for carrier extraction. There are important measurements, in addition to interference-enhanced spectroscopic ellipsometry, which can be explored using other spectroscopic techniques and electron microscopy to further study carrier movement and validate the optical absorption coefficient.

A very important project would be to fabricate, test and optimize fabrication conditions for a solar cell device utilizing polycyrstalline Cu_4TiSe_4 as the p-type layer. An initial layer structure would be grown upon molybdenum substrates, then the Cu_4TiSe_4 layer, a ZnO (or a suitable n-type layer) and a transparent conducting oxide (such as indium tin oxide). The prototype solar cell can be tested in a number of labs which have a solar simulator, such as Prof. Jamie Phillips (EECS) and at the National Renewable Energy Laboratory.

Another idea is to epitaxially grow single crystal Cu_4TiSe_4 films by PLD on a GaAs substrates to see if it is possible to grow low defect density films. The reason for this is because a lot of the "waste" in converting light energy into electricity comes from recombination of carriers before they are able to reach the current collectors. There are three kinds of recombination mechanisms. If the dominant recombination mechanism happens to be Shockley-Reed-Hall, then this problem can be mitigated by growing defect-free single crystal films. The improvement in crystallinity reduces the density of defects by reducing grain boundaries, which is considered a defect. Additional annealing of the thin film can lower the defect density due to the rapid nature of deposition which pulsed laser deposition imposes.

To study the recombination mechanisms, I recommend that time-resolved terahertz spectroscopy be utilized to determine the dominant recombination mechanism and determine carrier mobility. Dr. Jason Baxter at Drexel University operates and oversees the time-resolved

terahertz spectrometer, which has been used to study carrier properties on thin films for solar cell materials such as CZTS[186] and CdSe coated ZnO nanowires.[187] The measurement optimally requires a free-standing thin film which has been successfully delaminated from the substrate.

While both DFT calculations and interference-enhanced spectroscopic ellipsometry correlate with each other with respect to band gap and absorption coefficient determination, the order of magnitude above GaAs's absorption coefficient should be verified with other techniques. For example, transmission-based spectroscopic techniques on 100 - 200 nm thin film should be utilized. Thus, the first step to conducting this experiment is to deposit a known and verifiable (through atomic force microscopy at The Materials Characterization Center at the University of Michigan) thickness of film and to gather absorbance or transmission data from an optical absorption spectrometer with an NIR-VIS-UV light source.[159] The measurement can be performed at Prof. Bart Bartlett's lab (Chemistry Dept. at University of Michigan) or at Prof. Jennifer Aitken's lab (Chemistry Dept. At Duquesne University).

Further study of the $Cu_4TISe_{4-x}S_x$ composition requires lattice parameter refinement, compositional verification, electronic transport properties, thermal transport property and synthesis procedure refinement. First and foremost, the synthesis procedure refinement is important to produce, in bulk, single phase $Cu_4TISe_{4-x}S_x$ samples for further studies. A combination of synthesis parameter-PXRD-WDXRF-DSC feedback should be able to provide sufficient direction to refining the optical synthesis annealing profiles for the solid-state synthesis method. PXRD will provide bulk information on phase and detect phase impurities. WDXRF will provide compositional verification of the samples. DSC will provide thermal signature information which can be compared with phase diagram databases (ASM Alloy Phase Diagram database, access is available through the University of Michigan library). If there are phase

impurities which can be identified in PXRD patterns, then the phase diagrams involving the binary/elements can be compared against the phase diagram database. The phase diagram database also provides additional references to works that compiled the phase diagram or phases which are identified in the phase diagram. The information which is provided in this database can help adjust annealing profiles for synthesis. For example, if a phase is thermodynamically stable at elevated temperatures and appears in the PXRD or as a signature in the DSC, then it is advisable to lower the annealing temperature by 50 – 100 °C and increase the duration by 48 hours. It is also advisable that the annealing temperature can be reduced to avoid the formation of the impurity phase and performed twice with the same prescribed duration. The ampoules will need to be broken open in the glovebox, reground and resealed like described for the sample in Chapter 3.

With verification of single phase $Cu_4TISe_{4-x}S_x$ through these multiple methods, then further processing into 10 mm or 12.7 mm diameter pellet or7-10 mm x 2.5 mm x 2.5 mm prismatic bars can be done using the hot press and/or wire saw (Chapter 2). The pellets can be used for the laser flash measurement to determine thermal diffusivity and thermal conductivity. The bars can be measured in the ZEM-3 system to determine the Seebeck coefficient and electrical conductivity. The bars can also be used to perform temperature-dependent Hall measurement at Prof. Uher's lab (Physics Dept. at University of Michigan) to determine the carrier concentration as a function of temperature. The determination of these properties are important for elucidating electronically based limitations towards device manufacturer or how the properties change as a function of temperature. If thin films are created from these phases, it is also advisable to correlate thin film measurements with the bulk measurements.

7.3.2 $Cu_3NbS_{4-x}Se_x$ Series

With the $Cu_3NbS_{4-x}Se_x$ series, it should be determined if thin films can be made. If so, then the series can be integrated into tandem solar cells to harvest larger range of the solar spectrum for electricity. Additionally, the band gaps having been measured in the green region of the visible spectrum, as it is possible to produce green LEDs as an alternative to using GaP. This work can be performed through a close collaboration amongst the Poudeu, Heron and Deotare labs. The facilities under Prof. Poudeu's direction would primarily involve synthesis, phase analysis, thermal measurement and bulk electronic transport. Through collaboration with Prof. Heron's and Prof Deotare's laboratories, thin films and further optoelectronic measurements may be performed to ascertain film-specific characteristics to contrast with bulk properties.

Further, the remaining composition scale should be synthesized so that their band gaps can be determined. Other secondary concerns are related to structure and building a phase diagram for this series. This will give additional insight into the trends and features which stem from the addition substitution of selenium with sulfur. For instance, to further elucidate the structural changes which may occur at a 50:50 split between sulfur and selenium.

A feedback look of synthesis-PXRD-WDXRF-DSC like described in the previous section should also be followed to verify the composition and phase of the synthesized members. The procedure and rationale for this is the same, which will also help verify the density and lattice parameter relationship with composition change.

References

1 *U.S. Energy Flow*, 2016).

2 Council, N. R., Studies, D. o. E. a. L., Climate, B. o. A. S. a. & Change, A. s. C. C. P. o. A. t. S. o. C. *Advancing the Science of Climate Change*. (National Academies Press, 2011).

3 Solomon, S., Plattner, G.-K., Knutti, R. & Friedlingstein, P. Irreversible climate change due to carbon dioxide emissions. *Proceedings of the National Academy of Sciences* **106**, 1704-1709, doi:10.1073/pnas.0812721106 (2009).

4 *U.S. Electricity Flow*, 2015).

5 Tester, J. W., Drake, E. M., Driscoll, M. J., Golay, M. W. & Peters, W. A. *Sustainable Energy: Choosing Among Options*. (MIT Press, 2012).

6 Shankleman, J. & Martin, C. *Solar Could Beat Coal to Become the Cheapest Power on Earth*, <https://www.bloomberg.com/news/articles/2017-01-03/for-cheapest-power-on-earth-look-skyward-as-coal-falls-to-solar> (2017).

7 Munsell, M. *Solar PV Prices Will Fall Below $1.00 per Watt by 2020*, <https://www.greentechmedia.com/articles/read/solar-pv-prices-to-fall-below-1.00-per-watt-by-2020> (2016).

8 Markoff, J. *Start-Up Sells Solar Panels at Lower-Than-Usual Cost*, <http://www.nytimes.com/2007/12/18/technology/18solar.html> (2007).

9 Updated Capital Cost Estimates for Utility Scale Electricity Generating Plants. 201 (Department of Energy, Washington, DC, 2013).

10 Katagiri, H. *et al.* Development of CZTS-based thin film solar cells. *Thin Solid Films* **517**, 2455-2460, doi:10.1016/j.tsf.2008.11.002 (2009).

11 Song, X. *et al.* A Review on Development Prospect of CZTS Based Thin Film Solar Cells. *International Journal of Photoenergy* **2014**, 11, doi:10.1155/2014/613173 (2014).

12 Dubrovskii, G. B. Optical Properties of CdTe. *Soviet Phys. Solid State (Russian Edition)* **3** (1961).

13 Jackson, P. *et al.* New world record efficiency for Cu(In,Ga)Se2 thin-film solar cells beyond 20%. *Progress in Photovoltaics: Research and Applications* **19**, 894-897, doi:10.1002/pip.1078 (2011).

14 Minoura, S. *et al.* Dielectric function of Cu(In, Ga)Se_2-based polycrystalline materials. *Journal of Applied Physics* **113**, 063505, doi:doi:http://dx.doi.org/10.1063/1.4790174 (2013).

15 Joshi, R. A., Taur, V. S. & Sharma, R. Effect of annealing on conversion efficiency of nanostructured CdS/CuInSe2 heterojunction thin film solar cell prepared by chemical

ion exchange route at room temperature. *Materials Research Bulletin* **47**, 2206-2211, doi:http://dx.doi.org/10.1016/j.materresbull.2012.06.001 (2012).
16 Merino, J. M., Di Michiel, M. & Leon, M. Structural analysis of $CuInSe_2$ and $CuIn_3Se_5$ at different temperatures with synchrotron radiation. *J Phys Chem Solids* **64**, 1649-1652, doi:10.1016/S0022-3697(03)00114-8 (2003).
17 Akinlami, J. O. & Ashamu, A. O. Optical properties of GaAs. *Journal of Semiconductors* **34**, 032002 (2013).
18 Saga, T. Advances in crystalline silicon solar cell technology for industrial mass production. *NPG Asia Mater* **2**, 96-102 (2010).
19 Tokio, N. & Masayuki, M. 18% Efficiency Cd-Free Cu(In, Ga)Se 2 Thin-Film Solar Cells Fabricated Using Chemical Bath Deposition (CBD)-ZnS Buffer Layers. *Japanese Journal of Applied Physics* **41**, L165 (2002).
20 Ziang, X. *et al.* Refractive index and extinction coefficient of $CH_3NH_3PbI_3$ studied by spectroscopic ellipsometry. *Opt. Mater. Express* **5**, 29-43, doi:10.1364/ome.5.000029 (2015).
21 Madelung, O. *Semiconductors: Data Handbook*. (Springer Berlin Heidelberg, 2012).
22 Pistoia, G. *Lithium-Ion Batteries: Advances and Applications*. (Elsevier Science, 2013).
23 Hu, X., Li, S. E., Jia, Z. & Egardt, B. Enhanced sample entropy-based health management of Li-ion battery for electrified vehicles. *Energy* **64**, 953-960, doi:http://doi.org/10.1016/j.energy.2013.11.061 (2014).
24 Mizushima, K., Jones, P. C., Wiseman, P. J. & Goodenough, J. B. LixCoO2 (0<x<-1): A new cathode material for batteries of high energy density. *Materials Research Bulletin* **15**, 783-789, doi:10.1016/0025-5408(80)90012-4 (1980).
25 Etacheri, V., Marom, R., Elazari, R., Salitra, G. & Aurbach, D. Challenges in the development of advanced Li-ion batteries: a review. *Energy & Environmental Science* **4**, 3243-3262, doi:10.1039/c1ee01598b (2011).
26 Padhi, A. K., Nanjundaswamy, K. S. & Goodenough, J. B. Phospho-olivines as Positive-Electrode Materials for Rechargeable Lithium Batteries. *Journal of The Electrochemical Society* **144**, 1188-1194, doi:10.1149/1.1837571 (1997).
27 Delmas, C. & Croguennec, L. Layered Li(Ni, M)O2 Systems as the Cathode Material in Lithium-Ion Batteries. *MRS Bulletin* **27**, 608-612, doi:DOI: 10.1557/mrs2002.196 (2002).
28 Tsutomu, O. & Yoshinari, M. Layered Lithium Insertion Material of LiNi1/2Mn1/2O2 : A Possible Alternative to LiCoO2 for Advanced Lithium-Ion Batteries. *Chemistry Letters* **30**, 744-745, doi:10.1246/cl.2001.744 (2001).
29 Tsutomu, O. & Yoshinari, M. Layered Lithium Insertion Material of LiCo1/3Ni1/3Mn1/3O2 for Lithium-Ion Batteries. *Chemistry Letters* **30**, 642-643, doi:10.1246/cl.2001.642 (2001).
30 Croguennec, L. & Palacin, M. R. Recent Achievements on Inorganic Electrode Materials for Lithium-Ion Batteries. *Journal of the American Chemical Society* **137**, 3140-3156, doi:10.1021/ja507828x (2015).

31 Brian, M. *How Lithium-ion Batteries Work*, <http://electronics.howstuffworks.com/everyday-tech/lithium-ion-battery1.htm> (2006).
32 Chung, J. S. & Sohn, H. J. Electrochemical behaviors of CuS as a cathode material for lithium secondary batteries. *Journal of Power Sources* **108**, 226-231, doi:http://dx.doi.org/10.1016/S0378-7753(02)00024-1 (2002).
33 Wang, Y., Zhang, X., Chen, P., Liao, H. & Cheng, S. In situ preparation of CuS cathode with unique stability and high rate performance for lithium ion batteries. *Electrochimica Acta* **80**, 264-268, doi:http://dx.doi.org/10.1016/j.electacta.2012.07.004 (2012).
34 Gabano, J. P., Déchenaux, V., Gerbier, G. & Jammet, J. D-Size Lithium Cupric Sulfide Cells. *Journal of The Electrochemical Society* **119**, 459-461, doi:10.1149/1.2404230 (1972).
35 Eichhöfer, A., Sommer, H., Andrushko, V., Indris, S. & Malik, S. Influence of the Morphology of Lithiated Copper(I) Sulfides with the Formal Composition "Li2Cu4S3" on Their Stability in Electrochemical Cycling. *European Journal of Inorganic Chemistry* **2013**, 1531-1540, doi:10.1002/ejic.201201099 (2013).
36 Hongsberg, C. & Bowden, S. *Solar Cell Structure*, <http://www.pveducation.org/pvcdrom/solar-cell-structure> (
37 Jenny, D. A. & Bube, R. H. Semiconducting Cadmium Telluride. *Physical Review* **96**, 1190-1191 (1954).
38 Bube, R. H. Photoconductivity of the Sulfide, Selenide, and Telluride of Zinc or Cadmium. *Proceedings of the IRE* **43**, 1836-1850, doi:10.1109/jrproc.1955.278046 (1955).
39 Cusano, D. A. CdTe solar cells and photovoltaic heterojunctions in II–VI compounds. *Solid-State Electronics* **6**, 217-232, doi:http://dx.doi.org/10.1016/0038-1101(63)90078-9 (1963).
40 Goldstein, B. Properties of Photovoltaic Films of CdTe. *Physical Review* **109**, 601-603 (1958).
41 Sinha, P. Life cycle materials and water management for CdTe photovoltaics. *Solar Energy Materials and Solar Cells* **119**, 271-275, doi:http://doi.org/10.1016/j.solmat.2013.08.022 (2013).
42 Winkler, M. T. *et al.* Optical designs that improve the efficiency of Cu2ZnSn(S,Se)4 solar cells. *Energ Environ Sci* **7**, 1029-1036, doi:10.1039/c3ee42541j (2014).
43 Tinoco, T., Rincón, C., Quintero, M. & Pérez, G. S. Phase Diagram and Optical Energy Gaps for CuInyGa1−ySe2 Alloys. *physica status solidi (a)* **124**, 427-434, doi:10.1002/pssa.2211240206 (1991).
44 Green, M. A. Thin-film solar cells: review of materials, technologies and commercial status. *Journal of Materials Science: Materials in Electronics* **18**, 15-19, doi:10.1007/s10854-007-9177-9 (2007).
45 Stanbery, B. J. Copper Indium Selenides and Related Materials for Photovoltaic Devices. *Critical Reviews in Solid State and Materials Sciences* **27**, 73-117, doi:10.1080/20014091104215 (2002).

46 Repins, I. *et al.* 19·9%-efficient ZnO/CdS/CuInGaSe2 solar cell with 81·2% fill factor. *Progress in Photovoltaics: Research and Applications* **16**, 235-239, doi:10.1002/pip.822 (2008).
47 Hedstrom, J. *et al.* in *Conference Record of the Twenty Third IEEE Photovoltaic Specialists Conference - 1993 (Cat. No.93CH3283-9)*. 364-371.
48 Chen, S., Gong, X. G., Walsh, A. & Wei, S.-H. Defect physics of the kesterite thin-film solar cell absorber Cu_2ZnSnS_4. *Applied Physics Letters* **96**, 021902, doi:10.1063/1.3275796 (2010).
49 Nagoya, A., Asahi, R., Wahl, R. & Kresse, G. Defect formation and phase stability of Cu_2ZnSnS_4 photovoltaic material. *Physical Review B* **81**, 113202 (2010).
50 Chen, S., Yang, J.-H., Gong, X. G., Walsh, A. & Wei, S.-H. Intrinsic point defects and complexes in the quaternary kesterite semiconductor Cu_2ZnSnS_4. *Physical Review B* **81**, 245204 (2010).
51 Chen, S., Walsh, A., Gong, X.-G. & Wei, S.-H. Classification of Lattice Defects in the Kesterite Cu_2ZnSnS_4 and $Cu_2ZnSnSe_4$ Earth-Abundant Solar Cell Absorbers. *Adv Mater* **25**, 1522-1539, doi:10.1002/adma.201203146 (2013).
52 Winter, M. *Abundance in Earth's crust*, <https://www.webelements.com/periodicity/abundance_crust/> (1993).
53 Kehoe, A. B., Scanlon, D. O. & Watson, G. W. The electronic structure of sulvanite structured semiconductors Cu3MCh4 (M = V, Nb, Ta; Ch = S, Se, Te): prospects for optoelectronic applications. *Journal of Materials Chemistry C* **3**, 12236-12244, doi:10.1039/c5tc02760h (2015).
54 Aoife, B. K., David, O. S. & Graeme, W. W. Modelling potential photovoltaic absorbers Cu 3 MCh 4 (M = V, Nb, Ta; Ch = S, Se, Te) using density functional theory. *Journal of Physics: Condensed Matter* **28**, 175801 (2016).
55 Grima-Gallardo, P. *et al.* Cu3TaSe4 and Cu3NbSe4: X-ray diffraction, differential thermal analysis, optical absorption and Raman scattering. *Journal of Alloys and Compounds* **658**, 749-756, doi:http://dx.doi.org/10.1016/j.jallcom.2015.10.283 (2016).
56 LeBlanc, S. Thermoelectric generators: Linking material properties and systems engineering for waste heat recovery applications. *Sustainable Materials and Technologies* **1–2**, 26-35, doi:http://doi.org/10.1016/j.susmat.2014.11.002 (2014).
57 O'Brien, R. C., Ambrosi, R. M., Bannister, N. P., Howe, S. D. & Atkinson, H. V. Safe radioisotope thermoelectric generators and heat sources for space applications. *Journal of Nuclear Materials* **377**, 506-521, doi:http://doi.org/10.1016/j.jnucmat.2008.04.009 (2008).
58 Tritt, T. M. & Subramanian, M. Thermoelectric materials, phenomena, and applications: a bird's eye view. *MRS bulletin* **31**, 188-198 (2006).
59 *Thermoelectric Devices*, <https://sites.suffolk.edu/scioto/2016/03/04/thermoelectric-devices/> (2016).

60 Minnich, A., Dresselhaus, M., Ren, Z. & Chen, G. Bulk nanostructured thermoelectric materials: current research and future prospects. *Energy & Environmental Science* **2**, 466-479 (2009).
61 Snyder, G. J. & Toberer, E. S. Complex thermoelectric materials. *Nature materials* **7**, 105-114 (2008).
62 Chung, D.-Y. *et al.* CsBi4Te6: A high-performance thermoelectric material for low-temperature applications. *Science* **287**, 1024-1027 (2000).
63 Parker, D. & Singh, D. J. High-temperature thermoelectric performance of heavily doped PbSe. *Physical Review B* **82**, 035204 (2010).
64 Pei, Y., Lensch-Falk, J., Toberer, E. S., Medlin, D. L. & Snyder, G. J. High thermoelectric performance in PbTe due to large nanoscale Ag2Te precipitates and La doping. *Advanced Functional Materials* **21**, 241-249 (2011).
65 Wang, H., Pei, Y., LaLonde, A. D. & Snyder, G. J. Heavily Doped p-Type PbSe with High Thermoelectric Performance: An Alternative for PbTe. *Advanced Materials* **23**, 1366-1370 (2011).
66 Dresselhaus, M. S. *et al.* New Directions for Low-Dimensional Thermoelectric Materials. *Advanced Materials* **19**, 1043-1053 (2007).
67 Narducci, D., Selezneva, E., Cerofolini, G., Frabboni, S. & Ottaviani, G. Impact of energy filtering and carrier localization on the thermoelectric properties of granular semiconductors. *Journal of Solid State Chemistry* **193**, 19-25 (2012).
68 Paul, B., Kumar, A. & Banerji, P. Embedded Ag-rich nanodots in PbTe: enhancement of thermoelectric properties through energy filtering of the carriers. *Journal of Applied Physics* **108**, 064322 (2010).
69 Soni, A. *et al.* Interface driven energy filtering of thermoelectric power in spark plasma sintered Bi2Te2. 7Se0. 3 nanoplatelet composites. *Nano letters* **12**, 4305-4310 (2012).
70 Xie, W. *et al.* Recent advances in nanostructured thermoelectric half-Heusler compounds. *Nanomaterials* **2**, 379-412 (2012).
71 Heremans, J. P. *et al.* Enhancement of thermoelectric efficiency in PbTe by distortion of the electronic density of states. *Science* **321**, 554-557 (2008).
72 Lin, S. *et al.* Tellurium as a high-performance elemental thermoelectric. *Nature communications* **7** (2016).
73 Pei, Y., Wang, H. & Snyder, G. Band engineering of thermoelectric materials. *Advanced materials* **24**, 6125-6135 (2012).
74 Zevalkink, A., Toberer, E. S., Bleith, T., Flage-Larsen, E. & Snyder, G. J. Improved carrier concentration control in Zn-doped Ca5Al2Sb6. *Journal of applied physics* **110**, 013721 (2011).
75 Zhang, J. *et al.* Band structure engineering in (Bi1− xSbx) 2Te3 ternary topological insulators. *Nature communications* **2**, 574 (2011).
76 Hochbaum, A. I. *et al.* Enhanced thermoelectric performance of rough silicon nanowires. *Nature* **451**, 163-167 (2008).

77 Kim, W. *et al.* Thermal conductivity reduction and thermoelectric figure of merit increase by embedding nanoparticles in crystalline semiconductors. *Physical Review Letters* **96**, 045901 (2006).
78 Yang, J., Meisner, G. & Chen, L. Strain field fluctuation effects on lattice thermal conductivity of ZrNiSn-based thermoelectric compounds. *Applied physics letters* **85**, 1140 (2004).
79 Poudel, B. *et al.* High-thermoelectric performance of nanostructured bismuth antimony telluride bulk alloys. *Science* **320**, 634-638 (2008).
80 Poudeu, P. F. *et al.* Nanostructures versus Solid Solutions: Low Lattice Thermal Conductivity and Enhanced Thermoelectric Figure of Merit in Pb9. 6Sb0. 2Te10-x Se x Bulk Materials. *Journal of the American Chemical Society* **128**, 14347-14355 (2006).
81 Pei, Y.-L. *et al.* High thermoelectric performance in n-type BiAgSeS due to intrinsically low thermal conductivity. *Energy & Environmental Science* **6**, 1750-1755 (2013).
82 Romano, G., Di Carlo, A. & Grossman, J. C. Mesoscale modeling of phononic thermal conductivity of porous Si: interplay between porosity, morphology and surface roughness. *Journal of Computational Electronics* **11**, 8-13 (2012).
83 Telkes, M. The Efficiency of Thermoelectric Generators. I. *Journal of Applied Physics* **18**, 1116-1127 (1947).
84 Zhang, H. & Talapin, D. V. Thermoelectric tin selenide: The beauty of simplicity. *Angewandte Chemie International Edition* **53**, 9126-9127 (2014).
85 Zhao, L.-D. *et al.* Ultralow thermal conductivity and high thermoelectric figure of merit in SnSe crystals. *Nature* **508**, 373-377 (2014).
86 Pei, Y. *et al.* Convergence of electronic bands for high performance bulk thermoelectrics. *Nature* **473**, 66-69 (2011).
87 Chung, D. Y. *et al.* in *IEEE.*
88 West, A. R. *Solid State Chemistry and its Applications*. (Wiley, 2014).
89 Hagenmuller, P. *Preparative Methods in Solid State Chemistry*. (Elsevier Science, 2012).
90 Schneider, C. W. & Lippert, T. in *Laser Processing of Materials: Fundamentals, Applications and Developments* (ed Peter Schaaf) 89-112 (Springer Berlin Heidelberg, 2010).
91 Eason, R. *Pulsed laser deposition of thin films: applications-led growth of functional materials*. (Wiley-Interscience, 2007).
92 Speakman, S. A. *Basics of X-Ray Powder Diffraction*, 2011).
93 Rodriguez-Carvajal, J. Recent advances in magnetic Structure determination by neutron powder diffraction. *Physica B-Condensed Matter* **192**, 55-69 (1993).
94 Rodriguez-Carvajal, J. Recent Developments of the Program FULLPROF, in Commission on Powder Diffraction (IUCr). *Newsletter* **26**, 12-19 (2001).
95 SHELXTL, DOS Windows/NT v. version 6.12 (Bruker analytical X-ray instruments Inc., Madison, WI, USA, 2000).
96 Sheldrick, G. M. Crystal structure refinement with SHELXL. *Acta Crystallographica Section C: Structural Chemistry* **71**, 3-8 (2015).

97 Stoyko, S. S. *et al.* Three series of quaternary rare-earth transition-metal pnictides with $CaAl_2Si_2$-type structures: $RECuZnAs_2$, $REAgZnP_2$, and $REAgZnAs_2$. *J Solid State Chem* **213**, 275-286, doi:http://doi.org/10.1016/j.jssc.2014.03.009 (2014).
98 Nobbs, J. H. Kubelka—Munk Theory and the Prediction of Reflectance. *Review of Progress in Coloration and Related Topics* **15**, 66-75, doi:10.1111/j.1478-4408.1985.tb03737.x (1985).
99 *Ellipsometry Measurement*, <https://www.jawoollam.com/resources/ellipsometry-tutorial/ellipsometry-measurements> (
100 Hilfiker, J. N., Synowicki, J. A. & Tompkins, H. G. in *51st Annual Technical Conference.* 511-516 (Society of Vacuum Coaters, 2008).
101 Chen, Y., Davoisne, C., Tarascon, J.-M. & Guery, C. Growth of single-crystal copper sulfide thin films viaelectrodeposition in ionic liquid media for lithium ion batteries. *Journal of Materials Chemistry* **22**, 5295-5299, doi:10.1039/c2jm16692e (2012).
102 Han, F., Li, W.-C., Li, D. & Lu, A.-H. In Situ Electrochemical Generation of Mesostructured Cu2S/C Composite for Enhanced Lithium Storage: Mechanism and Material Properties. *ChemElectroChem* **1**, 733-740, doi:10.1002/celc.201300182 (2014).
103 Kim, J.-S. *et al.* The electrochemical properties of copper sulfide as cathode material for rechargeable sodium cell at room temperature. *Journal of Power Sources* **189**, 864-868, doi:http://dx.doi.org/10.1016/j.jpowsour.2008.10.057 (2009).
104 Etienne, A. Electrochemical Method to Measure the Copper Ionic Diffusivity in a Copper Sulfide Scale. *Journal of The Electrochemical Society* **117**, 870-874, doi:10.1149/1.2407659 (1970).
105 Kimihiko, O. & Shichio, K. Electrical Conduction and Phase Transition of Copper Sulfides. *Japanese Journal of Applied Physics* **12**, 1130 (1973).
106 Bredland, A. M., Messing, T. G. & Paulson, J. W. in *29th Power Sources Symposium of the Electrochemical Society.* 82-85.
107 Cuesta, A. J., Bump, D.D. in *The Electrochemical Society.* (ed N. Margalit B. Owens) 95-100.
108 Dampier, F. W. Cathodic Behavior of CuS, MoO//3, and MnO//2 in Lithium Cells. *Journal of The Electrochemical Society* **121**, 656-668 (1974).
109 Eichinger, G. & Besenhard, J. O. High energy density lithium cells. Part II. Cathodes and complete cells. *Journal of Electroanalytical Chemistry* **72**, 1-31 (1976).
110 Eichinger, G. & Fritz, H. P. Copper based electrodes in organic electrolyte solutions-III. The discharge mechanism of copper(II) sulphide in some organic solvents. *Electrochimica Acta* **20**, 753-757 (1975).
111 Fournie, R., Messina, R. & Perichon, J. Mécanisme de la réduction electrochimique en milieu non aqueux de materiaux cathodiques utilisés dans les piles au lithium, III. Réduction électrochimique d'électrodes membranaires de sulfures et oxydes de cuivre dans le mélange carbonate de propylène-1,2-diméthoxyéthane. *Journal of Applied Electrochemistry* **9**, 329-335 (1979).
112 Oliveria, M., McMullan, R. K. & Wuensch, B. J. Single crystal neutron diffraction analysis of the cation distribution in the high-temperature phases α-Cu2−xS, α-Cu2−xSe, and α-

Ag2Se. *Solid State Ionics* **28**, 1332-1337, doi:http://dx.doi.org/10.1016/0167-2738(88)90382-7 (1988).
113 Kubel, F., Bertheville, B. & Bill, H. Crystal structure of dilithiumsulfíde, Li_2S. *Z. Kristallogr. NCS.* **214**, 302 (1999).
114 Okhotin, A. S., Krestovnikov, A. N., Aivazov, A. A. & Pushkarskii, A. S. On the Mechanism of Heat Transfer in Ag_2S and Cu_2S. *physica status solidi (b)* **31**, 489-492, doi:10.1002/pssb.19690310207 (1969).
115 Heredy, L. M. & Lowell, R. United States patent (1973).
116 Lee, M. M., Teuscher, J., Miyasaka, T., Murakami, T. N. & Snaith, H. J. Efficient Hybrid Solar Cells Based on Meso-Superstructured Organometal Halide Perovskites. *Science* **338**, 643-647, doi:10.1126/science.1228604 (2012).
117 Hao, F., Stoumpos, C. C., Cao, D. H., Chang, R. P. H. & Kanatzidis, M. G. Lead-free solid-state organic-inorganic halide perovskite solar cells. *Nature Photonics* **8**, 489-494, doi:10.1038/nphoton.2014.82 (2014).
118 Stranks, S. D. & Snaith, H. J. Metal-halide perovskites for photovoltaic and light-emitting devices. *Nature Nanotechnology* **10**, 391-402, doi:10.1038/Nnano.2015.90 (2015).
119 Battaglia, C., Cuevas, A. & De Wolf, S. High-efficiency crystalline silicon solar cells: status and perspectives. *Energy & Environmental Science* **9**, 1552-1576, doi:10.1039/c5ee03380b (2016).
120 Masuko, K. *et al.* Achievement of More Than 25% Conversion Efficiency With Crystalline Silicon Heterojunction Solar Cell. *Ieee Journal of Photovoltaics* **4**, 1433-1435, doi:10.1109/Jphotov.2014.2352151 (2014).
121 Kayes BM *et al.* in *Proceedings of the 37th IEEE.* (Photovoltaic Specialists Conference).
122 Liu, M. Z., Johnston, M. B. & Snaith, H. J. Efficient planar heterojunction perovskite solar cells by vapour deposition. *Nature* **501**, 395-398, doi:10.1038/nature12509 (2013).
123 Ball, J. M., Lee, M. M., Hey, A. & Snaith, H. J. Low-temperature processed meso-superstructured to thin-film perovskite solar cells. *Energy & Environmental Science* **6**, 1739-1743, doi:10.1039/c3ee40810h (2013).
124 Zhou, H. P. *et al.* Interface engineering of highly efficient perovskite solar cells. *Science* **345**, 542-546, doi:10.1126/science.1254050 (2014).
125 Todorov, T. K., Reuter, K. B. & Mitzi, D. B. High-Efficiency Solar Cell with Earth-Abundant Liquid-Processed Absorber. *Advanced Materials* **22**, E156-+, doi:10.1002/adma.200904155 (2010).
126 Ito, K. & Nakazawa, T. Electrical and Optical-Properties of Stannite-Type Quaternary Semiconductor Thin-Films. *Japanese Journal of Applied Physics Part 1-Regular Papers Short Notes & Review Papers* **27**, 2094-2097, doi:Doi 10.1143/Jjap.27.2094 (1988).
127 Lee, Y. S. *et al.* $Cu_2ZnSnSe_4$ Thin-Film Solar Cells by Thermal Co-evaporation with 11.6% Efficiency and Improved Minority Carrier Diffusion Length. *Advanced Energy Materials* **5**, 1401372, doi:Unsp 1401372
10.1002/Aenm.201401372 (2015).

128 Wang, W. *et al.* Device Characteristics of CZTSSe Thin-Film Solar Cells with 12.6% Efficiency. *Advanced Energy Materials* **4**, 1301465, doi:Artn 1301465 10.1002/Aenm.201301465 (2014).
129 Chen, S. Y., Walsh, A., Gong, X. G. & Wei, S. H. Classification of Lattice Defects in the Kesterite Cu2ZnSnS4 and Cu2ZnSnSe4 Earth-Abundant Solar Cell Absorbers. *Advanced Materials* **25**, 1522-1539, doi:10.1002/adma.201203146 (2013).
130 DIAMOND v.Version 3.0 c (Crystal Impact GbR, Bonn, Germany, 2005).
131 Souilah, M., Lafond, A., Guillot-Deudon, C., Harel, S. & Evain, M. Structural investigation of the Cu_2Se-In_2Se_3-Ga_2Se_3 phase diagram, X-ray photoemission and optical properties of the $Cu_{1-z}(In_{0.5}Ga_{0.5})_{1+z/3}Se_2$ compounds. *J Solid State Chem* **183**, 2274-2280, doi:10.1016/j.jssc.2010.08.014 (2010).
132 Ren, Y., Meetsma, A., Spijkerman, A. & Wiegers, G. A. Crystal stucture determination of the $TiSe_2$-based misfit layer compound $(La\ Se)_{1.2}\ (TiSe_2)_2$. *Zeitschrift fuer Kristallographie* **212**, 586-p592 (1997).
133 Zhang, C. *et al.* An Ultrathin, Smooth, and Low-Loss Al-Doped Ag Film and Its Application as a Transparent Electrode in Organic Photovoltaics. *Adv Mater* **26**, 5696-5701, doi:10.1002/adma.201306091 (2014).
134 Hilfiker, J. N. *et al.* Survey of methods to characterize thin absorbing films with Spectroscopic Ellipsometry. *Thin Solid Films* **516**, 7979-7989, doi:http://dx.doi.org/10.1016/j.tsf.2008.04.060 (2008).
135 Tauc, J., Grigorovici, R. & Vancu, A. Optical Properties and Electronic Structure of Amorphous Germanium. *physica status solidi (b)* **15**, 627-637, doi:10.1002/pssb.19660150224 (1966).
136 Kresse, G. & Furthmuller, J. Efficiency of ab-initio total energy calculations for metals and semiconductors using a plane-wave basis set. *Computational Materials Science* **6**, 15-50, doi:10.1016/0927-0256(96)00008-0 (1996).
137 Kresse, G. & Furthmüller, J. Efficiency of ab-initio total energy calculations for metals and semiconductors using a plane-wave basis set. *Computational Materials Science* **6**, 15-50, doi:http://dx.doi.org/10.1016/0927-0256(96)00008-0 (1996).
138 Blochl, P. E. Projector augmented-wave method *Physical Review B* **50**, 17953-17979, doi:10.1103/PhysRevB.50.17953 (1994).
139 Kresse, G. & Joubert, D. From ultrasoft pseudopotentials to the projector augmented-wave method. *Physical Review B* **59**, 1758-1775, doi:10.1103/PhysRevB.59.1758 (1999).
140 Perdew, J. P., Burke, K. & Ernzerhof, M. Generalized gradient approximation made simple. *Physical Review Letters* **77**, 3865-3868, doi:10.1103/PhysRevLett.77.3865 (1996).
141 Monkhorst, H. J. & Pack, J. D. Special points for Brillouin-zone integrations *Physical Review B* **13**, 5188-5192, doi:10.1103/PhysRevB.13.5188 (1976).
142 Mehl, M. J. Pressure dependence of the elastic moduli in aluminum-rich Al-Li compounds. *Physical Review B* **47**, 2493-2500, doi:10.1103/PhysRevB.47.2493 (1993).
143 Togo, A. & Tanaka, I. First principles phonon calculations in materials science. *Scripta Materialia* **108**, 1-5, doi:10.1016/j.scriptamat.2015.07.021 (2015).

144 Kresse, G. & Hafner, J. *Ab initio* molecular dynamics for liquid metals. *Physical Review B* **47**, 558-561, doi:10.1103/PhysRevB.47.558 (1993).
145 Kresse, G. & Hafner, J. *Ab initio* molecular-dynamics simulation of the liquid-metal-amorphous-semiconductor transition in germanium. *Physical Review B* **49**, 14251-14269, doi:10.1103/PhysRevB.49.14251 (1994).
146 Kresse, G. & Furthmuller, J. Efficient iterative schemes for ab initio total-energy calculations using a plane-wave basis set. *Physical Review B* **54**, 11169-11186, doi:10.1103/PhysRevB.54.11169 (1996).
147 Kresse, G. & Furthmüller, J. Efficient iterative schemes for *ab initio* total-energy calculations using a plane-wave basis set. *Physical Review B* **54**, 11169-11186 (1996).
148 Blöchl, P. E. Projector augmented-wave method. *Physical Review B* **50**, 17953-17979 (1994).
149 Heyd, J., Scuseria, G. E. & Ernzerhof, M. Erratum: "Hybrid functionals based on a screened Coulomb potential" [J. Chem. Phys. 118, 8207 (2003)]. *The Journal of Chemical Physics* **124**, 219906, doi:10.1063/1.2204597 (2006).
150 Krukau, A. V., Vydrov, O. A., Izmaylov, A. F. & Scuseria, G. E. Influence of the exchange screening parameter on the performance of screened hybrid functionals. *The Journal of Chemical Physics* **125**, 224106, doi:10.1063/1.2404663 (2006).
151 Shishkin, M. & Kresse, G. Implementation and performance of the frequency-dependent GW method within the PAW framework. *Physical Review B* **74**, 035101 (2006).
152 Mostofi, A. A. *et al.* wannier90: A tool for obtaining maximally-localised Wannier functions. *Computer Physics Communications* **178**, 685-699, doi:http://dx.doi.org/10.1016/j.cpc.2007.11.016 (2008).
153 Albrecht, S., Reining, L., Del Sole, R. & Onida, G. *Ab Initio* Calculation of Excitonic Effects in the Optical Spectra of Semiconductors. *Physical Review Letters* **80**, 4510-4513 (1998).
154 Rohlfing, M. & Louie, S. G. Electron-Hole Excitations in Semiconductors and Insulators. *Physical Review Letters* **81**, 2312-2315 (1998).
155 Shockley, W. & Queisser, H. J. Detailed Balance Limit of Efficiency of P-N Junction Solar Cells. *J Appl Phys* **32**, 510, doi:Doi 10.1063/1.1736034 (1961).
156 Rühle, S. Tabulated values of the Shockley–Queisser limit for single junction solar cells. *Solar Energy* **130**, 139-147, doi:http://dx.doi.org/10.1016/j.solener.2016.02.015 (2016).
157 Shi, G. & Kioupakis, E. Electronic and Optical Properties of Nanoporous Silicon for Solar-Cell Applications. *ACS Photonics* **2**, 208-215, doi:10.1021/ph5002999 (2015).
158 Pauling, L. & Hultgren, R. The crystal structure of sulvanite, Cu_3VS_4. *Z Kristallogr* **84**, 204-212 (1933).
159 Seol, J.-S., Lee, S.-Y., Lee, J.-C., Nam, H.-D. & Kim, K.-H. Electrical and optical properties of Cu2ZnSnS4 thin films prepared by rf magnetron sputtering process. *Solar Energy Materials and Solar Cells* **75**, 155-162, doi:https://doi.org/10.1016/S0927-0248(02)00127-7 (2003).

160 Morris, J. W. & Krenn, C. R. The internal stability of an elastic solid. *Philosophical Magazine a-Physics of Condensed Matter Structure Defects and Mechanical Properties* **80**, 2827-2840 (2000).
161 Grimvall, G., Magyari-Koepe, B., Ozolins, V. & Persson, K. A. Lattice instabilities in metallic elements. *Reviews of Modern Physics* **84**, 945-986, doi:10.1103/RevModPhys.84.945 (2012).
162 Burch, K. S., Stephens, J., Kawakami, R. K., Awschalom, D. D. & Basov, D. N. Ellipsometric study of the electronic structure of ${\mathrm{Ga}}_{1\ensuremath{-}x}{\mathrm{Mn}}_{x}\mathrm{As}$ and low-temperature GaAs. *Physical Review B* **70**, 205208 (2004).
163 Adachi, S. Excitonic effects in the optical spectrum of GaAs. *Physical Review B* **41**, 1003-1013 (1990).
164 Šik, J., Schubert, M., Leibiger, G., Gottschalch, V. & Wagner, G. Band-gap energies, free carrier effects, and phonon modes in strained GaNAs/GaAs and GaNAs/InAs/GaAs superlattice heterostructures measured by spectroscopic ellipsometry. *J Appl Phys* **89**, 294-305, doi:10.1063/1.1328778 (2001).
165 Newhouse, P. F. *et al.* Thin film preparation and characterization of wide band gap Cu3TaQ4 (Q = S or Se) p-type semiconductors. *Thin Solid Films* **517**, 2473-2476, doi:https://doi.org/10.1016/j.tsf.2008.11.020 (2009).
166 Klepp, K. O. & Gurtner, D. Synthesis and crystal structure of Cu4TiS4: a novel chalcogenide with tetrahedrally coordinated titanium. *Journal of Alloys and Compounds* **243**, 19-22, doi:http://dx.doi.org/10.1016/S0925-8388(96)02363-8 (1996).
167 Ali, M. A., Jahan, N. & Islam, A. K. M. A. Sulvanite Compounds Cu 3 TMS 4 (TM = V, Nb and Ta): Elastic, Electronic, Optical and Thermal Properties using First-principles Method. *2014* **6**, 13, doi:10.3329/jsr.v6i3.19191 (2014).
168 Bougherara, K. *et al.* Structural, elastic, electronic and optical properties of Cu3TMSe4 (TM = V, Nb and Ta) sulvanite compounds via first-principles calculations. *Science of Advanced Materials* **5**, 97-106, doi:10.1166/sam.2013.1435 (2013).
169 Odobel, F., Le Pleux, L., Pellegrin, Y. & Blart, E. New Photovoltaic Devices Based on the Sensitization of p-type Semiconductors: Challenges and Opportunities. *Accounts of Chemical Research* **43**, 1063-1071, doi:10.1021/ar900275b (2010).
170 Walter, M. G. *et al.* Solar Water Splitting Cells. *Chemical Reviews* **110**, 6446-6473, doi:10.1021/cr1002326 (2010).
171 Kawazoe, H. *et al.* P-type electrical conduction in transparent thin films of CuAlO2. *Nature* **389**, 939-942 (1997).
172 Espinosa-García, W. F., Valencia-Balvín, C. & Osorio-Guillén, J. M. Phononic and thermodynamic properties of the sulvanite compounds: A first-principles study. *Computational Materials Science* **113**, 275-279, doi:http://dx.doi.org/10.1016/j.commatsci.2015.10.036 (2016).
173 Golub, A., Allali, N., Guyomard, D. & Danot, M. LITHIUM INTERCALATION DEINTERCALATION REACTIONS USING MATRICES WITH THE SULVANITE STRUCTURE -

DIMENSIONALITY LOWERING OF THE HOST-STRUCTURE. *Mater. Res. Bull.* **30**, 959-966, doi:10.1016/0025-5408(95)00083-6 (1995).
174 Lv, X. S. *et al.* Fundamental optical and electrical properties of nano-Cu3VS4 thin film. *Opt. Mater.* **34**, 1451-1454, doi:10.1016/j.optmat.2012.02.044 (2012).
175 Lu, Y.-J. & Ibers, J. A. Synthesis and Characterization of Cu_3NbSe_4 and KCu_2TaSe_4. *J Solid State Chem* **107**, 58-62, doi:http://dx.doi.org/10.1006/jssc.1993.1323 (1993).
176 Kars, M., Rebbah, A. & Rebbah, H. Cu3NbS4. *Acta Crystallographica Section E* **61**, 180-181, doi:doi:10.1107/S1600536805022397 (2005).
177 Mizutani, U. *Hume-Rothery Rules for Structurally Complex Alloy Phases*. (CRC Press, 2016).
178 Smith, W. F. & Hashemi, J. *Foundations of Materials Science and Engineering*. (McGraw-Hill, 2006).
179 Slater, J. C. Atomic Radii in Crystals. *The Journal of Chemical Physics* **41**, 3199-3204, doi:10.1063/1.1725697 (1964).
180 Kars, M., Rebbah, A. & Rebbah, H. Cu3NbS4. *Acta Crystallographica Section E* **61**, i180-i181, doi:doi:10.1107/S1600536805022397 (2005).
181 Mullay, J. in *Electronegativity* eds Kali Das Sen & C. K. Jørgensen) 1-25 (Springer Berlin Heidelberg, 1987).
182 Rodriguez-Carvajal, J. Recent advances in magnetic structure determination by neutron powder diffraction + FullProf. *Physica B: Condensed Matter* **192**, Pages 55–56 (1993).
183 Okamoto, H. *Desk Handbook: Phase Diagrams for Binary Alloys*. (ASM International, 2000).
184 Parish, G. *Growth and Characterization of Aluminum Gallium Nitride/Gallium Nitride Ultraviolet Detectors* Doctor of Philosophy thesis, University of California, Santa Barbara, (2001).
185 Kittel, C. *Introduction to Solid State Physics*. (Wiley, 2004).
186 Guglietta, G. W., Choudhury, K. R., Caspar, J. V. & Baxter, J. B. Employing time-resolved terahertz spectroscopy to analyze carrier dynamics in thin-film Cu2ZnSn(S,Se)4 absorber layers. *Applied Physics Letters* **104**, 253901, doi:10.1063/1.4884817 (2014).
187 Edley, M. E., Li, S., Guglietta, G. W., Majidi, H. & Baxter, J. B. Ultrafast Charge Carrier Dynamics in Extremely Thin Absorber (ETA) Solar Cells Consisting of CdSe-Coated ZnO Nanowires. *The Journal of Physical Chemistry C* **120**, 19504-19512, doi:10.1021/acs.jpcc.6b03974 (2016).